

Characterization of the Effects of Cerebral Aneurysm Geometry on
Hemodynamics and Endovascular Treatment Outcomes

by

Priya Nair

A Dissertation Presented in Partial Fulfillment
of the Requirements for the Degree
Doctor of Philosophy

Approved April 2016 by the
Graduate Supervisory Committee:

David Frakes, Chair
Brent Vernon
Brian Chong
Vincent Pizziconi
Ronald Adrian

ARIZONA STATE UNIVERSITY

May 2016

ABSTRACT

Cerebral aneurysms are pathological ballooning of blood vessels in the brain, commonly found in the arterial network at the base of the brain. Cerebral aneurysm rupture can lead to a dangerous medical condition, subarachnoid hemorrhage, that is associated with high rates of morbidity and mortality. Effective evaluation and management of cerebral aneurysms is therefore essential to public health. The goal of treating an aneurysm is to isolate the aneurysm from its surrounding circulation, thereby preventing further growth and rupture. Endovascular treatment for cerebral aneurysms has gained popularity over traditional surgical techniques due to its minimally invasive nature and shorter associated recovery time. The hemodynamic modifications that the treatment effects can promote thrombus formation within the aneurysm leading to eventual isolation. However, different treatment devices can effect very different hemodynamic outcomes in aneurysms with different geometries.

Currently, cerebral aneurysm risk evaluation and treatment planning in clinical practice is largely based on geometric features of the aneurysm including the dome size, dome-to-neck ratio, and parent vessel geometry. Hemodynamics, on the other hand, although known to be deeply involved in cerebral aneurysm initiation and progression, are considered to a lesser degree. Previous work in the field of biofluid mechanics has demonstrated that geometry is a driving factor behind aneurysmal hemodynamics.

The goal of this research is to develop a more combined geometric/hemodynamic basis for informing clinical decisions. Geometric main effects were analyzed to quantify contributions made by geometric factors that describe cerebral aneurysms (i.e., dome size, dome-to-neck ratio, and inflow angle) to clinically relevant hemodynamic responses

(i.e., wall shear stress, root mean square velocity magnitude and cross-neck flow). Computational templates of idealized bifurcation and sidewall aneurysms were created to satisfy a two-level full factorial design, and examined using computational fluid dynamics. A subset of the computational bifurcation templates was also translated into physical models for experimental validation using particle image velocimetry. The effects of geometry on treatment were analyzed by virtually treating the aneurysm templates with endovascular devices. The statistical relationships between geometry, treatment, and flow that emerged have the potential to play a valuable role in clinical practice.

DEDICATION

To my family, for always encouraging me to pursue what I believe in (even when you thought I was being unreasonable). Your unyielding love and support has kept me strong through this long and exciting journey, in a place so far away from home.

ACKNOWLEDGMENTS

Graduate school has been an incredible experience. In addition to the academic knowledge I amassed over the past few years, I have also learnt a lot that has contributed to my personal growth. This journey would not have been possible without the guidance, feedback, and support from a large number of people.

First and foremost, I would like to thank my amazing advisor Dr. David Frakes for his guidance, support, and belief in me (even when I didn't believe in myself). He has always motivated me to pursue my interests, constantly providing me with opportunities for the same. His foresight and approach to research is inspiring, and I am grateful for having been given opportunity to work in his lab.

I would also like to thank Dr. Brian Chong for his valuable inputs to my research in spite of his extremely busy schedule. His enthusiasm for my work has, time and again, reassured me of the importance of my work in the clinical community. I am also grateful to my committee members Drs. Ronald Adrian, Vincent Pizziconi, and Brent Vernon for their feedback and recommendations while being a part of my dissertation committee.

It has been my absolute pleasure working with everyone in the Image Processing Applications Laboratory. I am especially grateful to Dr. Haithem Babiker, who has been my mentor through this academic maze, for his excellent guidance and patience. I would like to thank Dr. Justin Ryan for providing the 3D models for my research. He, along with Jonathan Plasencia and Dr. Rafeed Chaudhury, have constantly supported me through this long expedition. I would also like to extend my gratitude to Aprinda

Indahlastari and James Lindsay for helping me out with the experiments, and Matthew Mortensen (and EndoVantage) for helping me out with the virtual device deployments.

To my friends, who kept me sane and made me feel at home – thank you for putting up with me. I would also like to thank my family, for this would not have been possible without their relentless support and encouragement.

Funding sources for this research includes: The American Heart Association Beginning Grant In Aid (#11GIA7970009), the National Science Foundation CAREER Award (#1151232), The Brain Aneurysm Foundation Research Grant, and Women & Philanthropy Society Category B Grant. I would like to extend my appreciation to Arizona State University's Graduate Education for supporting my post-candidacy doctoral work with the Graduate Dissertation Fellowship.

TABLE OF CONTENTS

	Page
LIST OF TABLES	xi
LIST OF FIGURES	xii
PREFACE.....	xxii
CHAPTER	
1 INTRODUCTION	1
2 CEREBRAL ANEURYSMS: EVALUATION AND TREATMENT STRATEGIES	4
2.1 Cerebral Aneurysms.....	4
2.2 Treatment Strategies	4
2.2.1 Surgical Treatment Techniques	5
2.2.2 Endovascular Treatment Techniques.....	6
2.3 Cerebral Aneurysm Evaluation in Clinical Practice	10
2.4 Role of Hemodynamics.....	14
3 INVESTIGATION OF CEREBRAL ANEURYSM HEMODYNAMICS	16
3.1 Current Techniques for Evaluating and Measuring Cerebral Aneurysm Hemodynamics	16
3.1.1 In-Vivo Techniques	16
3.1.2 In-Vitro Techniques.....	20
3.1.3 In-Silico Techniques	22
3.2 Investigation of Cerebral Aneurysm Hemodynamics Using Computational Fluid Dynamics	24
3.2.1 Governing Equations of Fluid Flow	25
3.2.2 Computational Modeling.....	26
3.2.3 Mesh Generation.....	28

CHAPTER	Page
3.2.4 Boundary Conditions	29
3.2.5 Simulations	32
3.2.6 Analysis.....	32
3.3 Investigation of Cerebral Aneurysm Hemodynamics Using Particle Image Velocimetry.....	33
3.3.1 Physical Modeling	34
3.3.2 Flow Loop.....	36
3.3.3 Data Acquisition	37
3.3.4 Camera Calibration	39
3.3.5 PIV Processing.....	40
3.3.6 Analysis.....	43
4 EFFECTS OF GEOMETRIC VARIATIONS ON IDEALIZED BIFURCATION ANEURYSM HEMODYNAMICS	44
4.1 Introduction.....	44
4.2 Methods.....	45
4.2.1 Study Design.....	45
4.2.2 Computational Methods.....	47
4.2.2.1 Computational Model Construction.....	47
4.2.2.2 Computational Fluid Dynamics	49
4.2.3 Experimental Methods.....	50
4.2.3.1 Physical Model Construction	50
4.2.3.2 Particle Image Velocimetry	52
4.2.4 Data Analysis	52
4.2.4.1 Computational Data Analysis	52

CHAPTER	Page
4.2.4.2 Experimental Data Analysis	53
4.3 Results.....	54
4.3.1 Idealized Aneurysm Models (Templates).....	54
4.3.1.1 Computational Results	54
4.3.1.2 Experimental Results	59
4.3.2 Anatomical Aneurysm Models	61
4.3.2.1 Computational Results	61
4.3.2.2 Experimental Results	63
4.4 Discussion	64
4.4.1 Effects of Geometric Main Factors on Hemodynamics.....	64
4.4.2 Comparisons with Experimental Results	66
4.4.3 Comparisons Among Idealized and Anatomical Findings	67
4.4.4 Limitations	68
5 EFFECTS OF GEOMETRIC VARIATIONS ON IDEALIZED SIDEWALL ANEURYSM HEMODYNAMICS	70
5.1 Introduction.....	70
5.2 Methods.....	71
5.2.1 Study Design.....	71
5.2.2 Computational Model Construction.....	73
5.2.3 Computational Fluid Dynamics	74
5.2.4 Computational Data Analysis	75
5.3.1 Idealized Aneurysm Models (Templates).....	76
5.3.2 Comparisons with Idealized Bifurcation Aneurysm Templates.....	81

CHAPTER	Page
5.4 Discussion	84
5.4.1 Effects of Geometric Main Factors on Hemodynamics.....	84
5.4.2 Comparisons Among Idealized Bifurcation and Sidewall Aneurysm Templates.....	86
6 HEMODYNAMIC CHARACTERIZATION OF CEREBRAL ANEURYSM TEMPLATES TREATED WITH EMBOLIC COILS	88
6.1 Introduction.....	88
6.2 Methods.....	89
6.2.1 Study Design.....	89
6.2.2 Computational Methods.....	90
6.2.2.1 Computational Model Construction.....	90
6.2.2.2 Virtual Device Deployment	91
6.2.2.3 Computational Fluid Dynamics	93
6.2.3 Experimental Methods.....	95
6.2.3.1 Physical Model Construction	95
6.2.3.2 Device Deployment	96
6.2.3.3 Particle Image Velocimetry	97
6.2.4 Analysis.....	97
6.2.4.1 Computational Data Analysis	97
6.2.4.2 Experimental Data Analysis	98
6.3 Results.....	98
6.3.1 Idealized Bifurcation Aneurysm Results	98
6.3.2 Idealized Sidewall Aneurysm Results	106
6.4 Discussion	110

CHAPTER	Page
6.4.1 Effects of Geometry and Treatment on Idealized Bifurcation Aneurysm Hemodynamics	110
6.4.2 Effects of Geometry and Treatment on Idealized Sidewall Aneurysm Hemodynamics	111
6.4.3 Clinical Implications.....	112
7 HEMODYNAMIC CHARACTERIZATION OF CEREBRAL ANEURYSM TEMPLATES TREATED WITH PIPELINE EMBOLIZATION DEVICE.....	115
7.1 Introduction.....	115
7.2 Methods.....	116
7.2.1 Study Design.....	116
7.2.2 Computational Modeling and Virtual Device Deployment.....	117
7.2.3 Computational Fluid Dynamics (CFD).....	120
7.2.4 Data Analysis.....	121
7.3 Results.....	122
7.3.1 Idealized Bifurcation Aneurysm Results	122
7.3.2 Idealized Sidewall Aneurysm Results	127
7.3.3 PED versus Embolic Coiling	131
7.4 Discussion	134
7.4.1 Effects of Geometry and Treatment on IBTA and ISA Templates	134
7.4.2 Effects of Aneurysm Geometry on Treatment Outcomes.....	135
8 CONCLUSIONS AND FUTURE WORK.....	138
REFERENCES.....	140
APPENDIX	
A PERMISSIONS	152

LIST OF TABLES

Table		Page
4.1	Percentage Changes in Hemodynamic Responses after Changing One Geometric Factor, Keeping the Other Two Factors Constant, for All Different Flow Rates.	56
5.1	Percentage Changes in Hemodynamic Responses Calculated by Changing One Geometric Factor, Keeping the Other Two Factors Constant, for All Investigated Flow Rates.	78
5.2	Percentage Contributions of the Investigated Geometric Factors, and Their Interactions, on Aneurysmal and Neck-plane Hemodynamic Responses in Idealized Bifurcation and Sidewall Aneurysm Templates. The First, Second and Third Largest Contribution is Highlighted in Orange, Purple and Grey, Respectively.	82
6.1	Coil Sizes Used for Virtual Deployment of Embolic Coils in the IBTA and ISA Aneurysms.	91
6.2	Hemodynamic Responses Calculated from CFD for All Four IBTA Templates and across All Investigated Steady and Pulsatile (in Parenthesis) Flow Rates before and after Treatment with Embolic Coils.	100
6.3	Hemodynamic Responses Calculated from CFD for all Four ISA Templates and across All Investigated Steady Flow Rates before and after Treatment with Embolic Coils.	107

LIST OF FIGURES

Figure	Page
1.1 Computational Model of a Cerebral Aneurysm.....	1
2.1 Surgical Treatment of a Cerebral Aneurysm by Placing a Clip across the Aneurysmal Neck. The Figure Was Reproduced from Brisman Et Al. 2006 [13].....	6
2.2 Endovascular Treatment Using Embolic Coils: (a) During Deployment, and (b) after Deployment. The Figure Was Reproduced from Brisman Et Al. 2006 [13].....	8
2.3 Digital Subtraction Angiography Images of a Giant Cerebral Aneurysm (a) Immediately after Stenting, (b) One Month after Stenting and before Coiling, and (c) One Year after Stent-assisted Coiling [20].....	9
2.4 Computational Model of a Pipeline Embolization Device (PED) Deployed in an Idealized Sidewall Aneurysm Model.	10
2.5 Cerebral Aneurysm Locations (With the Rate of Occurrence) in the Circle of Willis. The Figure Was Reproduced from Brisman Et Al. 2006 [13].....	13
3.1 Digital Subtraction Angiography Images of a Basilar Tip Aneurysm (a) Prior to Treatment, (b) During and (c) after Treatment with Stent-assisted Embolic Coiling. The Images Were Obtained with Permissions from RSNA [®] , and Was Published in Radiology 2009 (Vol: 253, Pp: 199-208) by Tähtinen Et Al. [55]. Permission Letter is Attached in Appendix A.....	18

Figure	Page
3.2 (Left) CTA Image of a Cerebral Aneurysm, and (Right) MRA Image of a Healthy Cerebrovascular System. Figure Was Reproduced from Keedy Et Al. 2006 [49]. Permission Letter is Attached in Appendix A.....	19
3.3 In-vitro Experimental Process. (a) Segmented Aneurysm from CT Image, (b) 3D Computational Model, (c) Lost-core Physical Model of the Cerebral Aneurysm, (d) Experimental Flow Loop, and (e) Aneurysmal Flow Vectors Obtained from Experimental investigation [74].	21
3.4 In-silico Flow Investigation. (a) Computational Cerebral Aneurysm Model, (b) the Meshed Computational Geometry, and (c) CFD Simulation Results Represented As Streamtraces Color-coded by Velocity Magnitude.....	23
3.5 Various Steps Involved in Successfully Setting Up and Performing a CFD Simulation.	25
3.6 (a) In-vivo Angiogram Image of a Basilar Tip Aneurysm [15], (b) Idealized Bifurcation Aneurysm Model, and (c) Idealized Sidewall Aneurysm Model.	27
3.7 Electrical Analog of (a) Resistance, and (b) Windkessel Outflow Boundary Conditions.	30

Figure	Page
3.8 Physical Model Construction Process for an Anatomical Cerebral Aneurysm. (a) Image Acquisition, (b) Segmentation and Reconstruction of the Cerebrovasculature, (c) Creation of the 3D Computational Aneurysm Model, (d) Wax Model Constructed from the Computational Model, (e) and (f) Metal Re-cast of the Wax Model, (G) Metal Model Encapsulated by Clear Urethane, (G) Close Up of the Lost-core Aneurysm Model, and (H) Experimental Flow Loop.	35
3.9 Photograph of the PIV System.....	36
3.10 Standard Configuration of a Stereoscopic PIV System with Two Cameras. Θ_1 and Θ_2 , and F_1 and F_2 are the Camera Angles and the Focal Lengths of Camera 1 and Camera 2, Respectively.	38
3.11 A Particle Image Obtained During PIV Data Acquisition.....	39
3.12 Marked Flat Type-5 Calibration with Software Detected Markers.	40
3.13 Calculation of Particle Displacement by Comparing Images Obtained at Two Subsequent Exposures Using Cross-correlation. Figure Was Reproduced from the LaVision FlowMaster Product-manual.	41
3.14 Velocity Vector Field (Averaged) Color-coded by Velocity Magnitude Obtained after PIV Processing in Davis.	42
4.1 Schematic Representation of the Three investigated Geometric Factors. The Directions of Inflow and Outflows are Marked by Arrows in the Drawing.	45

Figure	Page
4.2 Cube Representing a Two-level Full Factorial Experimental Design Based on Three Geometric Factors: Dome Size, Dome-to-neck Ratio, and Inflow Angle.....	46
4.3 Computational IBTA Templates. The Numbers in Red, Green, and Blue Represent the DS (in mm), DNR (No Units), and IA (in Degrees), Respectively. The Black Arrows Represent the Directions of Inflow and Outflows.....	48
4.4 Cube Representing a Full Factorial Design of DS, DNR and IA. The Orange Bubbles Represent the Five IBTA Templates Chosen for PIV Experimentation Based on a Fractional Factorial Design.	51
4.5 A Physical Urethane Model (IBTA1).....	51
4.6 (a) Effects of Dome Size Change on Aneurysmal V_{RMS} (Keeping Dome-to-neck Ratio and Inflow Angle Constant Within Grouped Bars) and (b) Effects of Dome-to-neck Ratio Change on Aneurysmal Wall Shear Stress (Keeping Dome Size and Inflow Angle Constant Within Grouped Bars). Solid and Patterned Colors Correspond to 3 mL/s Steady and Pulsatile CFD Simulations, Respectively, in the Idealized Model Templates.	57
4.7 Illustrations of Intra-aneurysmal Flow Patterns from CFD with Black Streamtraces and Color-coded Wall Shear Stress Overlays at 3 mL/s Steady Inflow.....	57

Figure	Page
4.8 Contributions Made by Individual Geometric Factors, and Their Interactions, to Effects on Simulated Hemodynamic Responses Under Steady (Solid Boxes) and Pulsatile (Patterned Boxes) Inflow Conditions in the Idealized Templates.....	59
4.9 Comparisons Between Aneurysmal V_{RMS} Values from PIV and CFD when Changing the Dome Size (Black to Red), Dome-to-neck Ratio (Black to Green), and Inflow Angle (Black to Blue). Solid and Patterned Boxes Correspond to 3 mL/s Steady and Pulsatile Inflows, Respectively, in the Idealized Aneurysm Models.	60
4.10 (a) PIV and (b) CFD Flow Fields Color-coded by Velocity Magnitude in IBTA-1 at Mid-systole for a 3 mL/s Pulsatile Inflow.....	61
4.11 Simulated Aneurysmal Wall Shear Stress in Anatomical and Idealized Basilar Tip Aneurysm Templates at 3 mL/s Steady and Pulsatile Inflow.	62
4.12 Illustrations of Intra-aneurysmal Flow Patterns Color-coded by Velocity Magnitude from CFD in (Top) Anatomical and (Bottom) Idealized Cerebral Aneurysm Templates, Both at 3 mL/s Steady Inflow.....	63
5.1 Schematic Representations of the Different Geometric Factors (and Values Used) to Generate Idealized Sidewall Aneurysm Templates for Hemodynamic Investigation. The Inflow-outflow Directions are Marked by Arrows in the Drawing.....	72

Figure	Page
5.2 Cube Representing a Two-level Full Factorial Design Used to Construct the Idealized Sidewall Aneurysm Templates Based on Three Geometric Factors: Dome Size, Dome-to-neck Ratio, and Inflow Angle. The Red, Green and Blue Edges Correspond to an Increase in DS, DNR, and IA, Respectively, with the Other Two Factors Held Constant, Along the Direction of the Colored Arrows.....	72
5.3 Idealized Computational Sidewall Aneurysm Templates. The Numbers in Red, Green, and Blue Correspond to the Dome Size, Dome-to-neck Ratio and Inflow Angle. The Direction of Inflow and Outflow is Marked with the Black Arrow in Template 1.....	73
5.4 Intra-aneurysmal Flow Patterns in the Idealized Sidewall Aneurysm Templates Represented as Streamtraces Color-coded by Velocity Magnitude, for an Inflow Rate of 3 mL/s.....	79
5.5 Effects of Change in (a) Dome Size (Keeping Dome-to-neck Ratio and Inflow Angle Constant Within Grouped Bars), (b) Dome-to-neck Ratio (Keeping Dome Size and Inflow Angle Constant Within Grouped Bars), and (c) Inflow Angle (Keeping Dome Size and Dome-to-neck Ratio Constant Within Grouped Bars) for a 3 mL/s Inflow.	79
5.6 Percentage Contribution of Dome Size, Dome-to-neck Ratio, and Inflow Angle to Effects on Idealized Sidewall Aneurysm Hemodynamics.....	81

Figure	Page
5.7 Comparison of Intra-aneurysmal Flow Patterns in Idealized (Left) Bifurcation and (Right) Sidewall Aneurysm Templates with (Top) Low and (Bottom) High Inflow Angle.	83
6.1 Representation of the Geometric Templates Used for Coiling (a) Chosen from the 2 ³ Factorial Design (Marked with Orange Bubbles), and (b) as a 2 ² Factorial Design.	90
6.2 Deployed Coil Configuration for the Cerebral Aneurysm Templates with (Left) Small DS, and (Right) Large DS.	93
6.3 (Top) IBTA and (Bottom) ISA Templates Virtually Treated with Embolic Coils.	93
6.4 Deployed Embolic Coils in the Physical Urethane Models.	96
6.5 Wall Shear Stress Distribution in the Idealized Basilar Tip Aneurysm Templates Pre- and Post-treatment at a 3 mL/s Steady Inflow Rate.	101
6.6 Effects of Increasing Aneurysmal Dome Size (from Black to Red Boxes) on Cross-neck Flow Keeping Inflow Angle Constant Within Grouped Bars. the Solid and Patterned Boxes Correspond to 3 mL/s Steady and Pulsatile Inflow Conditions, Respectively.	101
6.7 Effects of Steady (Solid Boxes) and Pulsatile (Patterned Boxes) Inflow Conditions on Aneurysmal V_{RMS} for IBTA-3.	102
6.8 Percentage Contributions of Dome Size (DS), Inflow Angle (IA), and Packing Density (PD) on (a) Aneurysmal Wall Shear Stress, (b) Aneurysmal V_{RMS} , (c) Neck-plane V_{RMS} , and (d) Cross-neck Flow.	103

Figure	Page
6.9 Percentage Contributions of Dome Size and Inflow Angle on Untreated (Solid Boxes) and Treated (Patterned Boxes) Hemodynamics Under Steady Flow Conditions.....	104
6.10 CFD to PIV Comparison of Cross-neck Flow in Untreated (Solid Boxes) and Treated (Patterned Boxes) IBTA Models at a 3 mL/s Steady Inflow Rate.	105
6.11 CFD (Left) and PIV (Right) Velocity Vector Distribution, Color-coded by Velocity Magnitude, in IBTA-8 at 3 mL/s Steady Inflow Rate.....	106
6.12 Velocity Streamtraces, Colored-coded by Velocity Magnitude, in (Top) Pre- and (Bottom) Post-treatment ISA Templates.....	108
6.13 Effects of Changing (a) Dome Size on Cross-neck Flow, and (b) Inflow Angle on Aneurysmal V_{RMS} , Keeping the Other Factor Constant Within the Grouped Bars at a Steady Inflow Rate of 3 mL/s.	108
6.14 Percentage Contribution of the Effects of Dome Size, Inflow Angle, and Packing Density on (a) Aneurysmal Wall Shear Stress, (b) Aneurysmal V_{RMS} , (c) Neck-plane V_{RMS} , and (d) Cross-neck Flow in the Idealized Sidewall Aneurysm Templates.	109
6.15 Percentage Contributions of DS and IA on Untreated (Solid Boxes) and Treated (Patterned Boxes) Hemodynamic Responses.....	110
6.16 WSS Changes in Anatomical Bifurcation Aneurysm Model, before and after Treatment with Embolic Coils, at a 3 mL/s Steady Inflow Rate.	114

Figure	Page
7.1 (a) Full Factorial Design of DS, DNR and IA with Orange Bubbles Representing the 3:2 DNR Templates and Pink Bubbles Representing the Two Templates with 2:1 DNR Chosen for Investigation with PEDs, and (b) a 2 ² Factorial Design the Wide-neck Templates.....	117
7.2 Virtual PED Deployment Process In a Sidewall Cerebral Aneurysm Template. (a) and (b) Depict Displacement of the Microcatheter to the Device Landing Zone, and (c) – (f) Depict the Device Unsheathing Process.	118
7.3 IBTA Templates Virtually Treated with Pipeline Embolization Device.....	119
7.4 ISA Templates Virtually Treated with Pipeline Embolization Device.....	119
7.5 Effects of Increasing Aneurysmal Dome Size on Neck-plane V_{RMS} in the Idealized Bifurcation Aneurysm Templates, at a Steady Inflow Rate of 3 mL/s.	123
7.6 Effects of Increasing DNR (from Black to Green Boxes) in Untreated (Solid Boxes) and Treated (Patterned Boxes) IBTA Templates.	124
7.7 Percentage Contribution of DS, IA and Treatment with PED on Modifying Aneurysmal and Neck-plane Hemodynamic Responses.	125
7.8 Effects of the Geometric Factors (I.E., DS and IA) on Pre- and Post-treatment IBTA Hemodynamics.	127
7.9 Effects of Increasing (a) DS on Neck-plane V_{RMS} , and (b) IA on Aneurysmal V_{RMS} for a 3 mL/s Steady Inflow Rate.	128
7.10 Percentage Contribution of Dome Size, Inflow Angle and PED Treatment on ISA Hemodynamics.	129

Figure	Page
7.11 Effects of Dome Size and Inflow Angle on ISA Hemodynamics, before and after Treatment with Pipeline Embolization Device.....	130
7.12 Streamtraces Color-coded by Velocity Magnitude in Idealized Bifurcation and Sidewall Aneurysm Templates (Left) Pre-treatment, (Middle) after Virtual Treatment with PED, and (Right) after Virtual Treatment with Embolic Coils.....	131
7.13 Effects of Treatment with PED and Embolic Coils on Idealized Bifurcation Aneurysm Templates.....	132
7.14 Effects of Treatment with PED and Embolic Coils on Idealized Sidewall Aneurysm Templates.....	133

PREFACE

All the work presented in this dissertation was primarily conducted at the Image Processing Applications Laboratory (IPALab), Arizona State University, under the advisement of Dr. David Frakes. The dissertation document, specifically Chapters 4, 5, 6 and 7, includes material from published manuscripts, or manuscripts in preparation for publication with other researchers. All the publications have the author of this dissertation as the first author. The physical urethane modeling process described in Chapter 4 was developed and carried out by Dr. J. Ryan as a Ph.D. student in the lab, and the flow experiments in Chapters 4, 6, and 7 were conducted by the author of this dissertation with A. Indahlastari (graduate researcher, IPALab) and J. Lindsay (undergraduate researcher, IPALab). The virtual coiling process presented in Chapter 6 was performed by A. Indahlastari for her Master's thesis, and the design and deployment technique was developed by Dr. H. Babiker for his Ph.D. thesis. The virtual deployments of the pipeline embolization device in Chapter 7 were completed using the EndoVantage Interventional Suite (EndoVantage, Scottsdale, Arizona, USA) by M. Mortensen, an undergraduate researcher in IPALab.

The bibliographic details including the manuscript title, authors, citation details and chapters that the material is located in are as follows:

- P. Nair, B. W. Chong, A. Indahlastari, J. Lindsay, D. Dejeu, V. Parthasarathy, J. Ryan, H. Babiker, C. Workman, L. F. Gonzalez, and D. Frakes, “Hemodynamic Characterization of Geometric Cerebral Aneurysm Templates,” *Journal of Biomechanics, In Press*, 2015. (CHAPTER 4)

- Chapters 5, 6 and 7: P. Nair, B. W. Chong, M. Mortensen, H. Babiker, J. Ryan, C. E. Baccin, and D. Frakes, "Effects of Geometry on Hemodynamics and Treatment Outcomes in Sidewall Cerebral Aneurysm Templates," *In Preparation*, 2016. (CHAPTERS 5, 6 and 7)
- Chapter 6: P. Nair, B. W. Chong, A. Indahlastari, J. Ryan, C. Workman, H. Babiker, H. Y Farsani, C. E. Baccin, and D. Frakes, "Hemodynamic Characterization of Geometric Cerebral Aneurysm Templates Treated with Embolic Coils," *Journal of Biomechanical Engineering*, 138(2), 021011 1-8, 2016.

CHAPTER 1
INTRODUCTION

Abnormal hemodynamics can lead to the initiation and progression of cardiovascular diseases, including heart diseases and stroke, which are among the leading causes of death in the United States. Cerebral aneurysms are one such class of cardiovascular diseases that account for about 30,000 deaths in the United States each year [1]. Cerebral aneurysms are out-pouchings of blood vessels in brain that are usually saccular in shape [2], and have a distinct sac (dome of the aneurysm) and a neck (where the aneurysm attaches to the parent vessel), as shown in Figure 1.1.

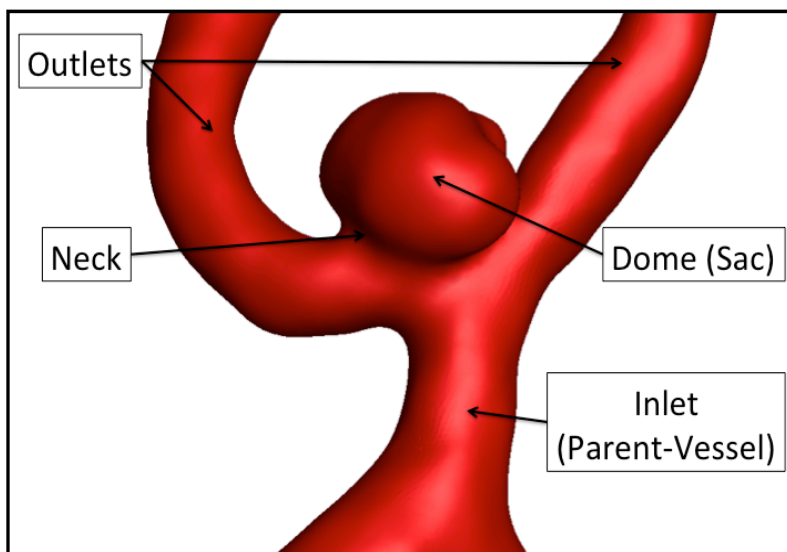


Figure 1.1: Computational model of a cerebral aneurysm.

Cerebral aneurysm rupture can lead to a dangerous medical condition known as subarachnoid hemorrhage (SAH). SAH, if not treated immediately, is associated with a

mortality rate of 40%. Furthermore, about half the survivors have permanent neurological deficits [1]. Although hemodynamics are known to be deeply involved in the onset and progression of cerebral aneurysms, they are still considered only to a limited degree during cerebral aneurysm evaluation and treatment planning in clinical practice. Current clinical evaluation strategies are primarily based on geometric features of the aneurysm (for example, the sac size). Although extensive studies have been performed that affirmed the importance of geometry-based cerebral aneurysm evaluation, the studies did not differentiate between different aneurysm types (i.e., whether the aneurysm is attached to the lateral vessel wall (sidewall aneurysm) or is present at arterial bifurcations (terminal aneurysms)) [3]–[5]. A study by Hassan et al. demonstrated considerably different hemodynamic environments between aneurysms with different parent vessel configurations [6]. The need for a thorough geometric-hemodynamic basis for informing clinical decisions is therefore essential to public health.

In this dissertation, the effects of geometric variations on hemodynamics are quantified in order to attribute specific hemodynamic features to geometric underliers that are routinely quantified in clinical practice. The hypothesis of this research is that geometric variations affect local hemodynamics, and can impact treatment outcomes. In other words, similar aneurysm configurations with some geometric differences can produce drastically different hemodynamic environments.

The main objectives of this dissertation were to (1) characterize the effects of geometry on cerebral aneurysm hemodynamics, and to (2) characterize the effects of geometry on endovascular treatment outcomes. The statistical relationships between geometry and flow that emerged have potential to play a valuable role in current clinical

practices for evaluating cerebral aneurysms and planning their treatments. Toward this end, a design of experiments was applied on idealized bifurcation and sidewall aneurysm templates to create unique combinations of three geometric factors. The templates were then investigated using computational fluid dynamics (CFD) and particle image velocimetry (PIV) to understand the effects of geometric variations on hemodynamics.

This document details the methods and results of the flow studies performed on the cerebral aneurysm templates, and also includes some patient-specific cerebral aneurysm models. An introduction to cerebral aneurysm and treatment, its evaluation in clinical practice, and the role of hemodynamics in cerebral aneurysm progression are presented in Chapter 2. Chapter 3 describes current in-vivo, in-vitro and in-silico techniques for measuring cerebral aneurysm hemodynamics, focusing on CFD and PIV. Chapters 4 and 5 investigate the effects of geometric changes on idealized bifurcation aneurysm and sidewall aneurysm hemodynamics, respectively, while Chapter 6 and 7 details the effects of aneurysm geometry and endovascular treatment on idealized cerebral aneurysm hemodynamics (both, bifurcation and sidewall). Chapters 4 – 7 were prepared as independent manuscripts that have been published, or are currently in preparation, in which the author of this dissertation is the first author. Lastly, conclusions and future work are discussed in Chapter 8.

CHAPTER 2

CEREBRAL ANEURYSMS: EVALUATION AND TREATMENT STRATEGIES

2.1 Cerebral Aneurysms

Cerebral aneurysms are localized dilations in blood vessels of the brain. They are predominantly found in major arteries at the base of the brain, particularly in the circle of Willis. Although aneurysms can be saccular (sac-like) or fusiform (dilation along a part of the vessel wall), over 90% of cerebral aneurysms are saccular [2]. An estimated 5% of the world population harbor unruptured cerebral aneurysms [7]. Cerebral aneurysm rupture can lead to a dangerous medical condition, called subarachnoid hemorrhage (SAH), where blood from within the arteries ooze into the space between the brain and the tissue covering the brain resulting in stroke. SAH is associated with a high rate of mortality, and can also result in permanent neurological deficits [8]. Effective cerebral aneurysm evaluation and treatment strategies (whether before or after rupture) are thus critical for successful clinical outcomes.

2.2 Treatment Strategies

The goal of cerebral aneurysm treatment is to prevent rupture by isolating the aneurysm from circulation. Current treatment techniques can be broadly categorized into two groups: surgical and endovascular. In the surgical technique the aneurysm is accessed

from outside the blood vessel, while the endovascular technique treats the aneurysm from within the affected blood vessels.

2.2.1 Surgical Treatment Techniques

Surgical treatment of cerebral aneurysms was the preferred method of treating unruptured and ruptured cerebral aneurysms until the 1990s. In this technique, the neurosurgeon cuts open a part of the patient's skull to physically access the aneurysm site. Small metallic clip (or clips), made of titanium, are then placed across the neck of the aneurysm thereby preventing the inflow of blood into the aneurysm sac, as demonstrated in Figure 2.1. Although surgical clipping produced excellent results, the invasive nature of this technique, long patient recover time, and the difficulty in treating inaccessible aneurysms or aneurysms near vital brain tissue resulted in the popularity of endovascular technique. The international subarachnoid aneurysm trial (ISAT) published in 2002 compared the effects of surgical clipping to endovascular coiling in 2143 patients with ruptured cerebral aneurysms. The patients were randomly assigned to surgical clipping or endovascular coiling, and were assessed at 2 months and 1 year following treatment. The findings indicated a higher mortality rate for surgical clipping compared to endovascular coiling (30.6% versus 23.7%) [9].

In some cases where clipping is not a viable surgical option, blood flow into the aneurysm is cutoff by occluding (one of) the inflow vessel(s). The occlusion procedure is sometimes combined with a bypass in order to restore blood flow to the downstream

vasculature by using a small graft. This procedure has been applied to giant, inoperable aneurysms [10]–[12].

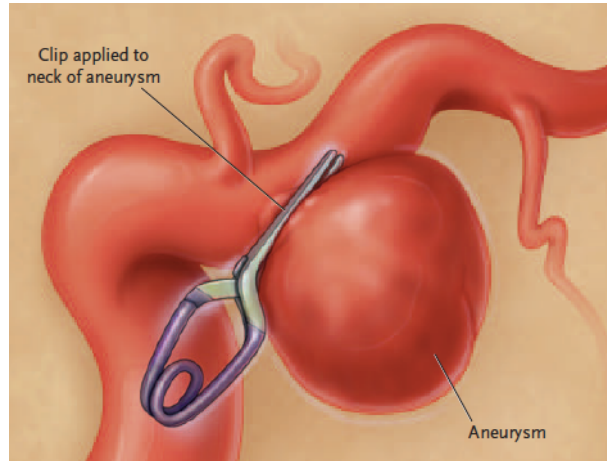


Figure 2.1: Surgical treatment of a cerebral aneurysm by placing a clip across the aneurysmal neck. The figure was reproduced from Brisman et al. 2006 [13].

2.2.2 Endovascular Treatment Techniques

Endovascular treatment of cerebral aneurysms is a minimally invasive technique where a neurointerventional surgeon makes a small incision at the femoral (or carotid) artery and navigates a micro-catheter containing the endovascular device to the aneurysm site, under fluoroscopic guidance. The device is then deployed in or around the aneurysm site to facilitate isolation of the aneurysm from circulation. Due to the minimally invasive nature of this technique, endovascular treatments have reduced hospital costs and mortality rates by 23% and 50%, respectively [14].

Endovascular Coiling

Treatment with embolic coils has been the most popular technique for cerebral aneurysm repair for over a decade [15], [16]. During this procedure, the aneurysm sac is packed with series of flexible coils, as shown in Figure 2.2. Blood flow into the aneurysm is reduced, thereby promoting thrombosis within the aneurysm sac. Over time, vascular remodeling at the neck leads to complete isolation of the aneurysm from circulation. In order to facilitate successful outcome, the packing density¹ (or PD) of the aneurysm is determined before treatment, based on the aneurysm geometry. A study by Sluzewski et al. demonstrated that aneurysms with PDs between 20% and 25% prevented unfavorable post-treatment hemodynamics [17]. PD can be calculated by customizing the coil deployment sequence prior to treatment based on the length, thickness, and loop radius of each coil.

¹ Packing density is defined as the percentage of aneurysmal volume occupied by coils

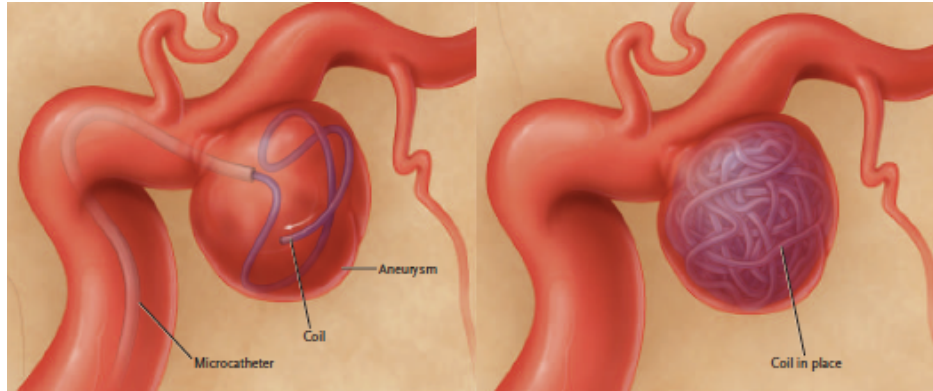


Figure 2.2: Endovascular treatment using embolic coils: (a) during deployment, and (b) after deployment. Figure was reproduced from Brisman et al. 2006 [13].

Endovascular Stenting

Sometimes embolic coiling alone is not a viable option for treatment of aneurysms with neck size greater than 5 mm, or dome-to-neck ratio² less than 1.6 [18], [19]. In such cases, one or more high porosity³ endovascular stents are often deployed across the neck of the aneurysm, following which coils are deployed within the aneurysm sac. The high porosity stent provides structural support, and prevents coil herniation into the parent vessel. Sometimes, coiling is performed immediately after stenting, and in other cases the two stages are performed over several days (or even months). Figure 2.3 represents a large aneurysm at different stages of stent-assisted coiling treatment. The Enterprise stent

² The dome-to-neck ratio is defined as the maximum width of the aneurysm dome to the diameter of the aneurysm neck.

³ Stent porosity is defined as the percentage of metal-free area per the total surface area of the stent

(Cordis Neurovascular Inc, Miami Lakes, Florida, USA) and Neuroform stent (Stryker, Fremont, California, USA) are some examples of high porosity endovascular stents.

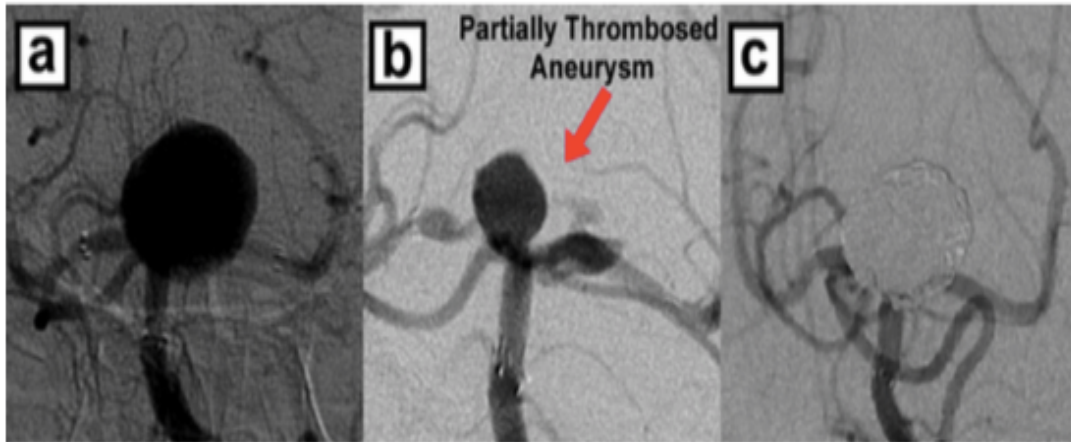


Figure 2.3: Digital subtraction angiography images of a giant cerebral aneurysm (a) immediately after stenting, (b) one month after stenting and before coiling, and (c) one year after stent-assisted coiling [20].

Low porosity endovascular stents (also known as flow diverting stents) are another class of endovascular stents used as a stand-alone treatment for cerebral aneurysms repair. The high-density braided stent struts alters intra-aneurysmal hemodynamics by reducing blood flow into the aneurysm, promoting intra-aneurysmal thrombosis and eventual occlusion. The Pipeline Embolization Device (PED) is one such FDA approved flow diverter often used in clinical practice that is associated with high angiographic occlusion rates at 6 month post-treatment [21]–[23]. A computational model of a PED is shown in Figure 2.4 [24]. PEDs were predominantly used to treat large and giant saccular and fusiform cerebral aneurysms (greater than 10 mm in diameter) [21], [22], [25]. However, since majority of the cerebral aneurysms found in the general

population are under 10 mm, PEDs are being used to treat smaller aneurysms as well [5], [26]. Although PEDs are associated with high occlusion rates, the effects of procedure related mortality and morbidity, and long term treatment impacts (especially in larger aneurysms) are not negligible [27], [28].

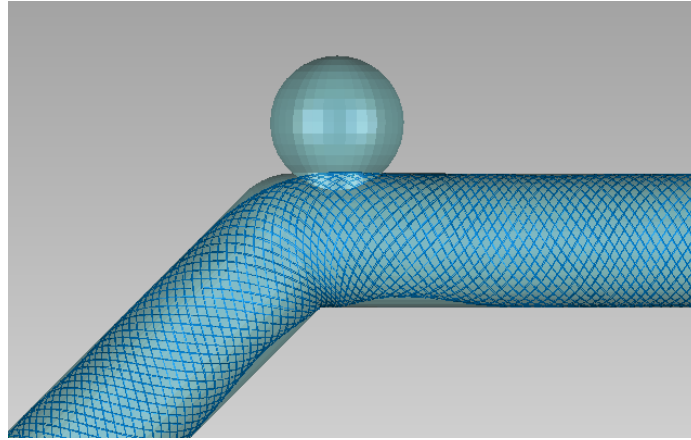


Figure 2.4: Computational model of a pipeline embolization device (PED) deployed in an idealized sidewall aneurysm model.

2.3 Cerebral Aneurysm Evaluation in Clinical Practice

Cerebral aneurysm evaluation and treatment planning in clinical practice is largely based on geometric features of the aneurysm, location of the aneurysm in the circle of Willis, aneurysm morphology, and other patient-specific characteristics.

Geometric Features

Aneurysm size is an important factor considered in clinical practice during cerebral aneurysm risk assessment, and treatment strategies. Extensive studies focusing on the natural history of aneurysms have identified dome size (DS) as an important predictor of growth and rupture. Cerebral aneurysms with DS greater than 10 mm have been found more prone to rupture [3], [5], [13], [29], [30]. However, 80% of the aneurysms found in the general population are less than 10 mm, and a large number of ruptured aneurysms recorded were also less than 10 mm [5], [31]–[34]. These findings indicate that aneurysm size should not be considered as a lone predictor in evaluating cerebral aneurysm risk. Additionally, while many larger aneurysms are treated almost immediately, management of small cerebral aneurysms is still a gray area because the tradeoff between associated treatment and rupture risks (especially when evaluation is based on size alone) is often unclear [31].

Aneurysm dome-to-neck ratio (DNR), and neck size (NS) are important geometric factors used in deciding suitable treatment strategies. DNR is defined as the ratio of the maximum width of the aneurysm to the diameter of the neck. Studies have shown that aneurysms with DNR over 1.6 and NS less than 5 mm, are suitable for treatment with embolic coils without the need for any adjunctive techniques, while treatment with PEDs are preferred for aneurysms with DNR under 1.5 (wide neck aneurysms) [18], [19], [21], [25]. In addition to DS and DNR, the inflow angle (IA) (defined as the angle between the inflow axis and main aneurysmal axis), has also been linked to aneurysmal outcomes [6], [35].

Aneurysm geometry is also known to affect treatment outcomes. Aneurysms with DS greater than 9 mm were observed to have higher recurrence rates after endovascular

coiling than aneurysms between 3 and 9 mm (50% versus 21%) [36]. Cerebral aneurysms with NS greater than 4 mm were also associated with high recurrence rates (52%) after endovascular coiling [36]. PEDs, on the other hand, were successful in treating large and giant aneurysms with rates of occlusion ranging from 81.8% to 94.4% at 6 months post-treatment [21], [22], [37].

Location

The most common locations for cerebral aneurysm formation are in the Circle of Willis, the arterial network at the base of the brain, as shown in Figure 2.5. It is estimated that over 85% of cerebral aneurysms are found in the anterior circulation of the Circle of Willis. However, studies on the natural history of cerebral aneurysms demonstrated that aneurysms in the posterior circulation were more prone to rupture, and were independent predictors of rupture risk with a hazard ratio of 2.9 [29], [38].

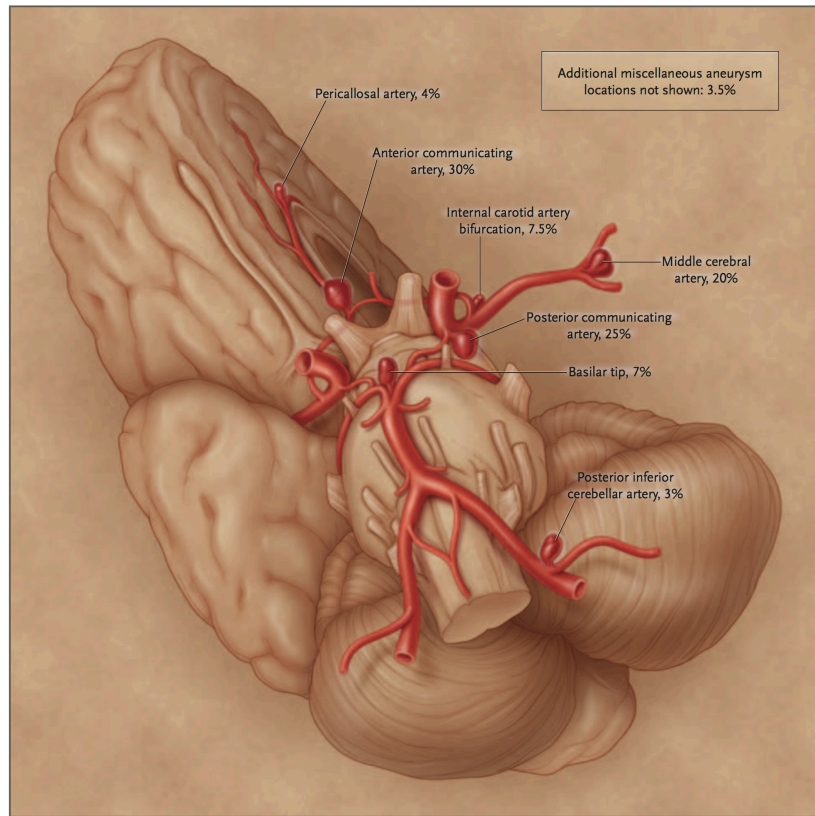


Figure 2.5: Cerebral aneurysm locations (with the rate of occurrence) in the Circle of Willis. The figure was reproduced from Brisman et al. 2006 [13].

Aneurysm Morphology

The morphology of the cerebral aneurysm also ties in with rupture risks. The presence of atypical aneurysm morphologies, such as multiple lobes on the aneurysm or daughter sacs, were found to increase the risk of aneurysm rupture [39], [40].

Patient-Specific Characteristics

Patient-specific characteristics are especially important during cerebral aneurysm evaluation. For example, Nahed et al., noted that age, sex, and cigarette smoking were all important contributors to the rupture of small cerebral aneurysms (< 7 mm) [41]. Furthermore, patients with prior history of SAH were also found to be at higher risks of aneurysm rupture [3], [5].

2.4 Role of Hemodynamics

Hemodynamics are known to be deeply involved in cerebral aneurysm initiation and progression. Although the precise cause is unknown, it is believed to occur due to complex interactions between the components of the blood vessel wall and hemodynamic forces acting on the vessel wall [2]. Wall shear stress (WSS) is an extensively studied hemodynamic response that is known to play an important role in cerebral aneurysm initiation and growth. High WSS is believed to initiate cerebral aneurysm formation by triggering the remodeling of the blood vessel wall [42], [43]. Low WSS, on the other hand, weakens the integrity of the vessel wall, thereby causing aneurysm growth and may eventually trigger aneurysm rupture [42]. Other hemodynamic parameters often investigated by researchers include the cumulative flow crossing the aneurysm neck per second (or cross-neck flow (CNF)), velocities, flow impingement regions, number of vortices and relative resident times within the aneurysm [44]–[46]. As mentioned earlier, the goal of aneurysm treatment is to isolate the aneurysm from circulation by reducing the inflow of blood, and creating a low flow environment within the aneurysm to promote thrombosis. Over time, vascular remodeling at the aneurysm neck will eventually seal the

aneurysm from circulation. It is therefore essential to understand hemodynamic environments before and after endovascular treatment.

In addition to comparing the pre- and post-treatment hemodynamics within the aneurysm, it is also important to understand the impact of aneurysm geometry on hemodynamics. It is well known that geometric factors are key determinants of aneurysmal hemodynamics [47]. However, unlike geometric factors, hemodynamics is considered only to a limited degree in current clinical practices during cerebral aneurysm evaluation and treatment planning. A primary reason for this lack of consideration is that hemodynamic data is often unavailable or difficult to acquire in clinical practice.

CHAPTER 3

INVESTIGATION OF CEREBRAL ANEURYSM HEMODYNAMICS

3.1 Current Techniques for Evaluating and Measuring Cerebral Aneurysm Hemodynamics

Cerebral aneurysm hemodynamics can be evaluated and measured within the body (in-vivo), outside the body (in-vitro), and using computational simulation techniques (in-silico).

3.1.1 In-Vivo Techniques

Various in-vivo techniques are employed for the measurement and evaluation of blood flow in a cerebral aneurysm. Some of the techniques commonly used in clinical scenario are Doppler ultrasound, Digital Subtraction Angiography (DSA), Computed Tomography Angiography (CTA), and Magnetic Resonance Angiography (MRA) [48], [49].

The use of Doppler ultrasound for the measurement of blood flow in cerebral arteries dates back to the early 1980s, where Aaslid et al., used this technique to record blood flow through three basal cerebral arteries [48]. The working of the Doppler ultrasound is based on the principle of the Doppler effect, where the difference in frequencies between the transmitted and received waves provides an estimate of flow velocity. During this procedure, a transmitter probe is placed on the skull (over the temporal lobe) that emits low-frequency ultrasound waves (≤ 2 MHz). These waves

travel through the skull into the blood vessels, and are reflected by the moving red blood cells within the blood vessels. The change in frequency between the transmitted and received waves (or the Doppler shift frequency, f_D) is directly proportional to the blood velocity, and cosine of the angle (θ) between the transmitted beam (f_T) and velocity vector (V).

$$f_D = f_R - f_T \quad (3.1)$$

$$= \frac{V \times \cos(\theta) \times 2f_T}{c}, \quad (3.2)$$

where f_R is the frequency of the received wave, and c is the speed of sound in blood (1541 m/s) [50]. From equation 3.2, the blood flow velocity can be calculated as

$$V = \frac{f_D \times c}{2f_T \times \cos(\theta)}. \quad (3.3)$$

Although this technique is inexpensive and allows dynamic evaluation of cerebral hemodynamics, it is highly operator dependent [51], [52]. Furthermore, about 10-20% of patient-population have inadequate trans-temporal acoustic windows that limits the quality of the received ultrasound waves [52].

The current standard technique for cerebral aneurysm evaluation and examination of treatment effectiveness in clinical practice is DSA. During a traditional angiography procedure the radiologist injects dye into the blood stream, and X-rays are used to visualize the contrast-enhanced blood vessels. However, during this process surrounding soft tissues also show up on the X-ray films, and can compromise the quality of visualization. During DSA imaging, an initial image is taken before contrast is injected into the blood stream. The radiologist then injects contrast at a controlled rate, while X-ray images are captured at a preset rate. Each of the images with contrast is then

subtracted from the initial image to obtain images of the cerebral aneurysm with superior spatial resolution [53]. DSA is used for precise visualization of the cerebral aneurysm and its surrounding vasculature in order to determine suitable treatment strategy, and also after treatment with endovascular devices or neurosurgical clipping to assess treatment success [54], [55]. Figure 3.1 shows DSA images of a cerebral aneurysm pre- and post-treatment with embolic coils. Additionally, this technique can provide hemodynamic information. However, if the aneurysm overlaps with adjacent vasculature, accurate visualization of the aneurysm is challenging. Three-dimensional (3D) rotational DSA imaging can be used in such cases. DSA is an expensive and invasive imaging technique, and is associated with complication rates 2-4%, with permanent neurological deficits in 0.3-0.5% of patients [49], [56]–[58].

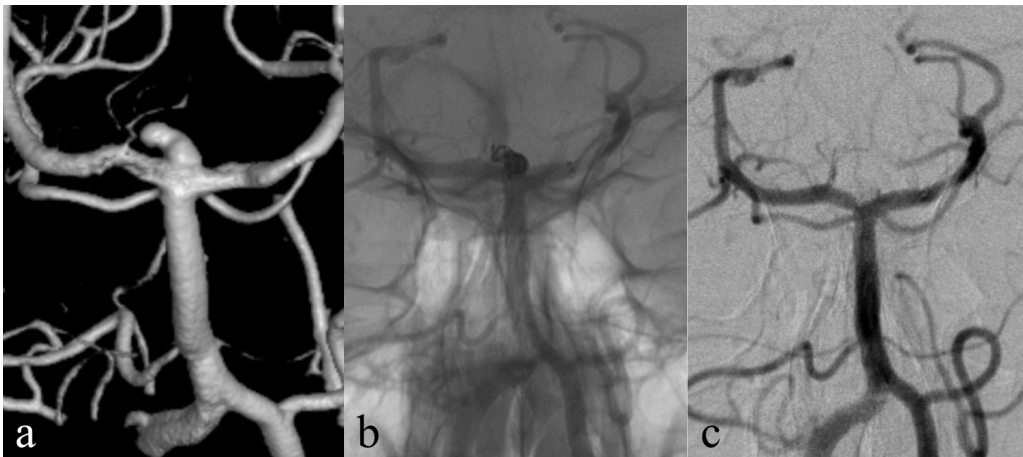


Figure 3.1: Digital subtraction angiography images of a basilar tip aneurysm (a) prior to treatment, (b) during and (c) after treatment with stent-assisted embolic coiling. The images were obtained with permissions from RSNA[®], and was published in Radiology 2009 (Vol: 253, pp: 199-208) by Tähtinen et al. [55]. Permission letter is attached in Appendix A.

While DSA is the preferred technique for cerebral aneurysm evaluation, CTA and MRA are frequently used for 3D visualization of cerebral aneurysm anatomy [49]. During CTA, a contrast dye is injected into the blood vessel and image slices of the region of interest (i.e., the aneurysm) are acquired from different perspectives. These different slices can be used to generate a rotational 3D model of the vasculature. MRA is a similar technique where 3D representation of the vessel anatomy can be reconstructed from image slices of the vasculature. Examples of cerebrovasculature obtained using CTA and MRA are shown in Figure 3.2. An advantage of MRA over CTA is that MRA does not require the use of contrast materials due to the absence of ionizing radiations. Nevertheless, gadolinium contrast agents can be used for better blood vessel and aneurysm visualization. Furthermore, MRA is suitable for acquiring morphological as well as hemodynamic information in cerebral blood vessels [59], [60].

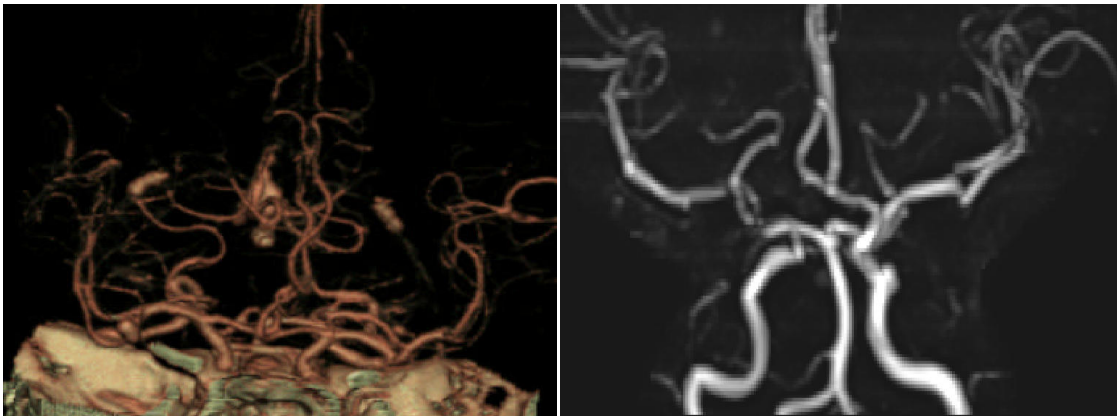


Figure 3.2: (left) CTA image of a cerebral aneurysm, and (right) MRA image of a healthy cerebrovascular system. Figure was reproduced from Keedy et al. 2006 [49]. Permission letter is attached in Appendix A.

The non-invasive nature of CTA and MRA imaging with improved delineation of the vessel wall has led to the popularity of these techniques over DSA. A meta-analysis comparing CTA with DSA in the diagnosis of cerebral aneurysms demonstrated that CTA images could be acquired with lesser patient risk and at reduced costs [61]. However, detection of small aneurysms (< 4 mm), and aneurysms next to bone structures, with CTA remains problematical [62]–[64]. Magnetic Resonance Imaging (MRI) and its variants can also be used to directly measure cerebral aneurysm hemodynamics, and is often used to provide patient-specific boundary conditions for computational fluid dynamic (CFD) simulations [65]–[67].

3.1.2 In-Vitro Techniques

In-vitro techniques, such as Particle Image Velocimetry (PIV) and Laser Doppler Velocimetry (LDV), are frequently used to investigate the effects of hemodynamics on cerebral aneurysm growth, rupture, and treatment [68]–[71]. The general process of in-vitro flow experimentation involves (1) constructing/creating the computational model, (2) translating the computational model into a physical model, (3) connecting the physical model to a flow loop filled with blood analog fluid, and (4) measuring fluid flow through the model using optical imaging or other flow measurement techniques.

PIV is a powerful laser-based, optical flow measurement technique extensively used in cerebral aneurysm research [20], [69], [72], [73]. During this technique, one or more high-resolution cameras capture images of particles (illuminated by a laser) suspended in a flowing fluid in quick succession, and calculate flow velocities by

comparing particle movement between subsequent frames. An overview of the PIV experimentation process is illustrated in Figure 3.3, and a detailed explanation is provided in Section 3.3.

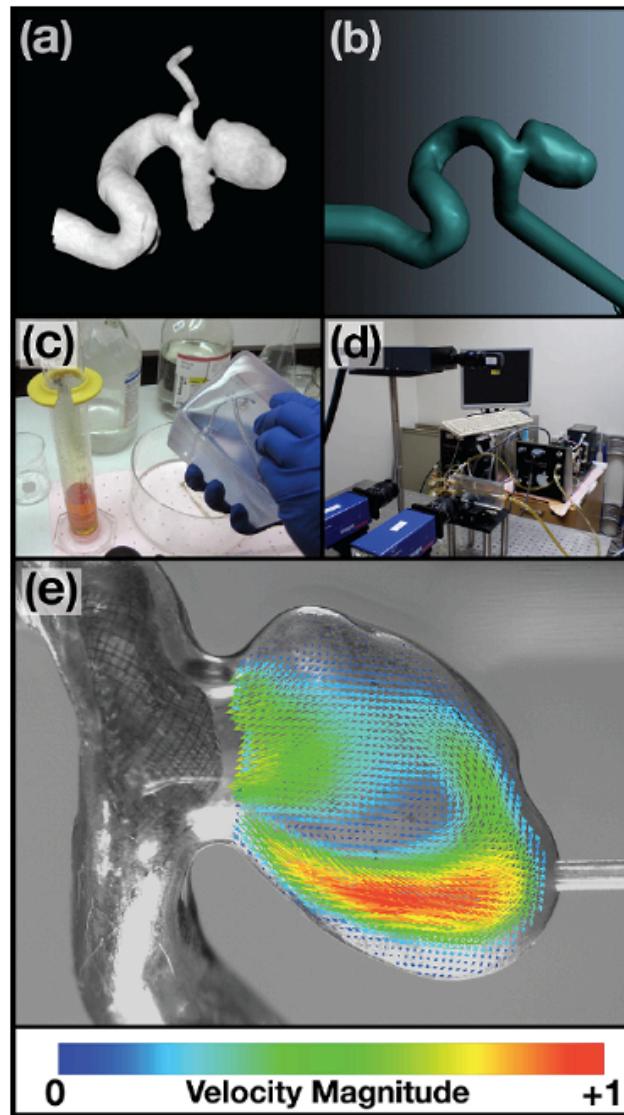


Figure 3.3: In-vitro experimental process. (a) Segmented aneurysm from CT image, (b) 3D computational model, (c) lost-core physical model of the cerebral aneurysm, (d) experimental flow loop, and (e) aneurysmal flow vectors obtained from experimental investigation [74].

3.1.3 In-Silico Techniques

Advances in computational modeling techniques have allowed the use of computational fluid dynamics (CFD) for the investigation of cerebral aneurysm hemodynamics, in-silico, on a patient-specific basis. CFD solves the governing equations of fluid flow (i.e., Navier-Stokes equations) using numerical methods and algorithms. The validity of CFD simulations has been confirmed by various experimental studies, and it is the most popular technique for measuring and analyzing cerebral aneurysm hemodynamics [75]–[78]. CFD offers several advantages over in-vivo and in-vitro examination of cerebral aneurysm hemodynamics. CFD allows hemodynamic examination of large patient population. In-vivo flow measurement can pose significant patient risks [56], [58], while in-vitro evaluation requires the construction of customized flow models for individual aneurysm geometries and can be time-consuming. CFD techniques also allow evaluation of cerebral hemodynamics after virtual treatment with endovascular devices such as embolic coils and stents [79]–[81]. In spite of the flexibility that CFD offers over experimentations, it is not without limitations. One of the major limitations is the computational power required to perform such tedious numerical calculations. As a result, simplifying assumptions are often made to reduce simulation complexity by assuming that the vasculature has rigid walls, and the fluid is modeled as Newtonian and incompressible. Additionally, computational analysis of complex devices also proves to be challenging, primarily due to difficulty in meshing the device geometry.

In general, flow investigation using CFD entails the following steps: (1) construction of the computational model, including the inflow and outflow vessels, (2) discretization of the computational geometry into mesh elements, (3) application of boundary conditions to the inflow(s), outflow(s), and vessel walls, and (4) simulation of blood flow through the model. An example of the CFD process is presented in Figure 3.4 (a)-(c).

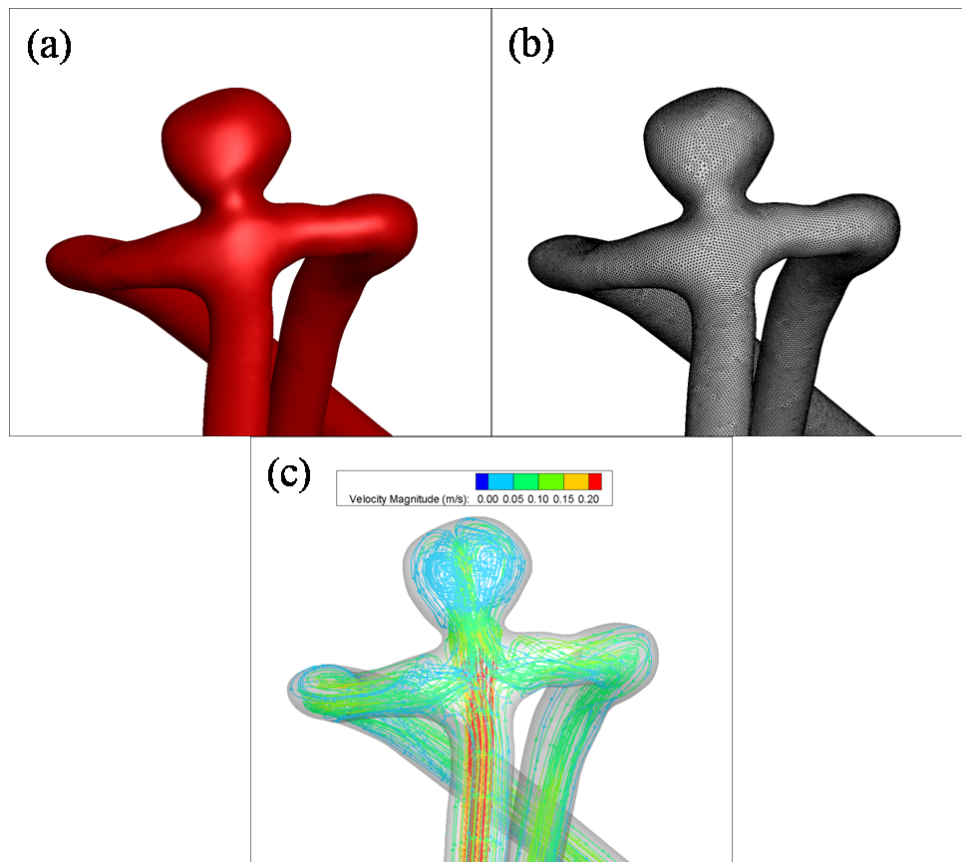


Figure 3.4: In-silico flow investigation. (a) Computational cerebral aneurysm model, (b) the meshed computational geometry, and (c) CFD simulation results represented as streamtraces color coded by velocity magnitude.

3.2 Investigation of Cerebral Aneurysm Hemodynamics Using Computational Fluid Dynamics

CFD is a branch of fluid dynamics that numerically solves the equations describing fluid flow using principles of physics, mathematics, and computer science. Some advantages of CFD over experimental measurement techniques are as follows:

- 3D flow information can be obtained using CFD, whereas most experiments are point/plane based
- Complex flows can be simulated
- Faster turnaround time compared to experiments since CFD does not require the construction of physical vascular models
- Unphysical flow phenomena can also be investigated for better understanding of underlying physics.

This section details the CFD methods used to acquire the hemodynamic parameters presented in Chapters 4, 5, 6 and 7. The importance of meshing and boundary conditions are also highlighted in this section. The workflow process to obtain simulation results is shown in Figure 3.5.

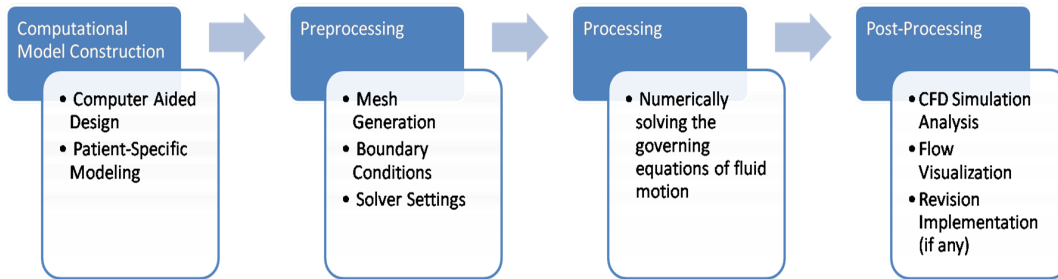


Figure 3.5: Various steps involved in successfully setting up and performing a CFD simulation.

3.2.1 Governing Equations of Fluid Flow

The governing equations of fluid flow are based on the laws of conservation of (1) mass, (2) linear momentum, and (3) energy. In order to simplify the complexity of CFD simulations for modeling blood flow, some assumptions have to be made. One of the main assumptions made is modeling blood as a Newtonian and incompressible fluid. In reality, blood is a non-Newtonian fluid (i.e., the shear stress is not linearly proportional to the shear rate), with some amount of compressibility. However, modeling non-Newtonian flow behavior is a complex process, and therefore the assumption of Newtonian behavior is commonly used in modeling blood flow. Studies comparing non-Newtonian and Newtonian fluid models in cerebral aneurysms have demonstrated that while absolute values of calculated hemodynamic responses vary between the two fluid models, the global characteristics of flow patterns do not vary significantly [64], [82].

The Navier-Stokes equations are the governing equations of fluid flow consisting of continuity and momentum equations. The general form of Navier-Stokes equation is can be written as follows:

$$\vec{v} \cdot \nabla \vec{v} = 0, \quad (3.4)$$

$$\frac{\partial \vec{v}}{\partial t} + \vec{v} \cdot \nabla \vec{v} = -\frac{1}{\rho} \nabla P + \nu \nabla^2 \vec{v} + \vec{g}, \quad (3.5)$$

where \vec{v} is the velocity vector, P is the pressure, ρ is the density of the fluid, ν is the kinematic viscosity of the fluid, and \vec{g} is the gravitational force. The kinematic viscosity is defined as the ratio of the dynamic viscosity and density of the fluid ($\nu = \frac{\mu}{\rho}$). Equations

3.4 and 3.5 are the continuity and momentum equations, respectively.

3.2.2 Computational Modeling

The first step towards setting up a CFD simulation is the construction of the computational geometries. In this dissertation the effects of geometry and treatment on idealized bifurcation and sidewall cerebral aneurysm hemodynamics were investigated. SolidWorks (Dassault Systèmes, Waltham, Massachusetts, USA) was used to construct the idealized aneurysm templates. The computational bifurcation aneurysm template was designed based on angiographic image of a basilar tip aneurysm, as shown in Figure 3.6 (a). The aneurysms were constructed as spheres, and the parent vessels were modeled as 4 mm diameter cylinders. Examples of the final bifurcation and sidewall aneurysm templates are shown in Figure 3.6 (b) and (c). Details on the idealized template designs are presented in Chapters 4 and 5.

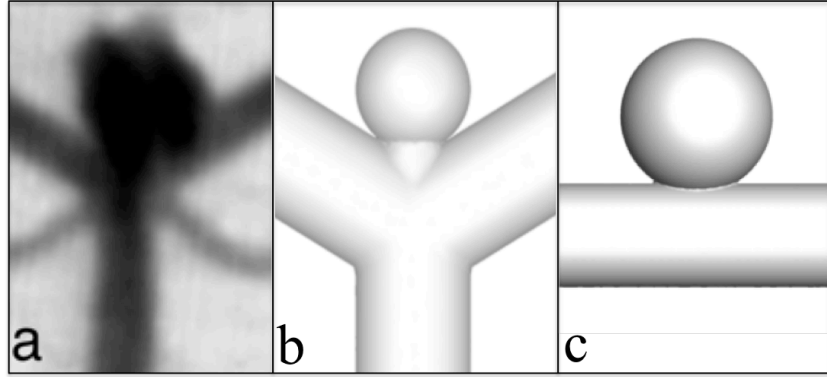


Figure 3.6: (a) In-vivo angiogram image of a basilar tip aneurysm [15], (b) idealized bifurcation aneurysm model, and (c) idealized sidewall aneurysm model.

A few patient-specific cerebral aneurysm models were also investigated in order to translate the findings based on the idealized templates to more realistic scenarios. The anatomical aneurysm geometries were segmented and reconstructed from patient-specific CT datasets using Mimics (Materialize, Leuven, Belgium). The underlying CT data had image matrix sizes of 512 by 512 pixels, pixel dimensions of 0.5 mm square, and slice thicknesses of 0.625 mm. The models were then trimmed using Geomagic (3D Systems, Rock Hill, South Carolina, USA) to represent the region of interest (i.e., aneurysm and parent vessels), and smoothed to remove geometric aberrations (if any). The inlet and outlet(s) of all the computational templates were extruded to ensure fully developed flow conditions at the aneurysm site, and to aid in simulation convergence. The final computational models (idealized and anatomical) were then exported as Virtual Reality Modeling Language (VRML) files for meshing.

3.2.3 Mesh Generation

Mesh generation is an important step in the CFD workflow since the governing equations of fluid flow are discretized and solved within each of the mesh elements. The cerebral aneurysm templates were meshed in ANSYS ICEM 14.1 (Ansys, Inc., Canonsburg, Pennsylvania, USA), where the fluid volume was discretized into unstructured tetrahedral mesh elements using the patch-independent Octree approach. The Octree approach is based on the concept of spatial subdivisions where: (1) a “root” tetrahedron is first generated such that it encloses the entire geometry, (2) the tetrahedron is next subdivided in powers of 2 until all the elements either match or are smaller than the maximum element size specified by the user, (3) the tetrahedral elements close to the surface are projected onto the surface as triangles to create a surface mesh around the geometry, and (4) the volume and surface mesh elements are smoothed by moving nodes and edges until it conforms to the geometry. The Octree approach was chosen for meshing since it is most suited for discretizing complex geometries.

Adequate mesh resolution is required to accurately capture fluid dynamics within the aneurysm, and it affects the accuracy of the hemodynamic responses investigated. In order to ensure that the hemodynamic responses obtained were independent of mesh sizes, mesh refinement studies were performed on one idealized untreated bifurcation and one untreated sidewall cerebral aneurysm template at a steady inflow rate of 3 mL/s. The final mesh sizes were deemed acceptable when changes in the hemodynamic response calculated between different mesh resolutions were less than 5%. The meshes were then

imported into ANSYS Fluent (Ansys, Inc., Canonsburg, Pennsylvania, USA) for CFD simulations.

3.2.4 Boundary Conditions

Boundary conditions play a vital role in dictating the accuracy of hemodynamics obtained from CFD simulations. In order to obtain physiologic flow fields, it is essential to supply accurate and realistic boundary conditions. Velocity-based inflow boundary conditions are most commonly used for incompressible flow simulations, where the velocity vector and scalar of the flow at the inlet are specified. This velocity information can be obtained either on a patient-specific basis, or based on existing literature of flow velocities in the region of interest (in this case, cerebral blood flow).

The outlet boundary conditions describe the downstream vasculature of the cardiovascular system, and are more complex than inlet boundary conditions. The effects of outlet boundary conditions on pressure and flow fields within the domain of interest have been thoroughly investigated by various researchers, and it has been well established that the downstream vasculature plays an important role in producing realistic hemodynamics within the simulated arteries [83]–[86]. The most commonly used outlet boundary condition for flow simulation in arteries is by specifying **zero pressure or zero-traction** at the outlet. This boundary condition assumes that blood flows freely through the system, and the flow regime within the domain of interest is solely dictated by the arterial geometry. But in reality, the downstream vasculature is largely responsible for modifying hemodynamics, and also in dictating the direction of flow though the

system [87]. Proper flow split between different arteries can be captured by **resistance outflow boundary conditions**, depicted by the resistor in Figure 3.7 (a). This model takes the resistance of the downstream vasculature into account while performing CFD simulations, and is the simplest model to implement. In the resistance boundary condition, a direct linear relationship exists between pressure (P) and flow (Q) through the blood vessel, and can be written as:

$$P = R_p Q, \quad (3.6)$$

where, R_p is the peripheral (downstream) resistance of the domain under investigation. Using this formulation, appropriate outlet pressures can be prescribed for the CFD simulations.

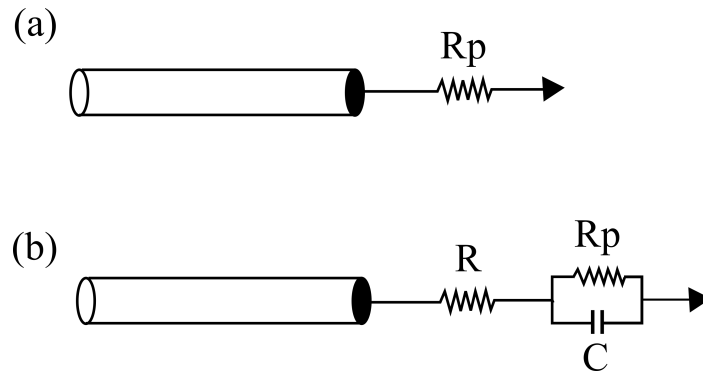


Figure 3.7: Electrical analog of (a) resistance, and (b) Windkessel outflow boundary conditions.

The main drawback of the resistance outflow boundary condition is that it does not take blood vessel compliance into account. In order to integrate the effect of wall compliance, more complex lumped-parameter models can be used as outlet boundary conditions. The simplest of the lumped-parameter models used in cardiovascular

literature is the **Windkessel model** (or **RCR model**) that includes a capacitor (C) to account for vessel compliance. The electrical analog of the Windkessel outflow boundary condition is presented in Figure 3.7 (b). The equations representing the three elements (R, R_p , and C) can be combined into a single ODE [86] to obtain

$$\frac{dp}{dt} + p \frac{1}{R_p C} = R \frac{dQ}{dt} + \frac{1}{R_p C} (R + R_p) Q, \quad (3.7)$$

and solution to the above equation is,

$$p(t) = e^{-\frac{t}{R_p C}} \int_0^t e^{\frac{s}{R_p C}} R \frac{dQ(s)}{ds} + \frac{1}{R_p C} (R + R_p) Q(s) ds + p(0). \quad (3.8)$$

Although the Windkessel outflow boundary condition can accurately model physiological flow regimes, such boundary conditions become more important for deformable wall simulations such as in the cardiovascular regions where, unlike the cerebrovasculature, compliance is highly prevalent [87].

In this dissertation, flow rates of 2, 3, and 4 mL/s were investigated, that corresponded to inflow velocities of 0.159, 0.239, and 0.318 m/s, respectively. The flow rates were chosen to span healthy and diseased flow conditions in a cerebral artery, and the values were taken from literature [88]. Steady and pulsatile flow conditions were investigated. For the steady state simulations, a constant velocity value was prescribed at the inlet. In some simulations (untreated bifurcation aneurysms), a user-defined parabolic flow profile was prescribed at the inlet, while a modified vertebral artery flow waveform was specified at the inlets for the pulsatile simulations [89]. Zero-pressure (and zero-traction) outlet boundary conditions were applied to the idealized bifurcation cerebral

aneurysm templates, while a resistance outlet boundary condition was applied to the idealized sidewall cerebral aneurysm templates. The vessel walls were assumed to be rigid. While compliant walls would be more beneficial, previous studies have shown that the main driving factor for aneurysmal hemodynamics is vessel geometry and that vessel compliance is secondary or even tertiary [44]. Furthermore, the global flow and stress profiles generated from compliant wall simulations were similar to those from the rigid wall simulation cases [90], [91].

3.2.5 Simulations

The meshed aneurysm templates were imported into ANSYS Fluent where CFD simulations were performed. Blood was modeled as incompressible and Newtonian fluid. Initial and boundary conditions, as described in the previous section, were specified. The convergence criteria for the continuity and momentum equations were then specified as 1×10^{-5} , to ensure solution stability and accuracy. A pressure-based segregated solver was used to solve the Navier-Stokes equations. The Semi-Implicit Method for Pressure-Linked Equations (SIMPLE) algorithm was used for pressure-velocity coupling, and a second-order discretization scheme was used for momentum.

3.2.6 Analysis

The CFD results were analyzed using Tecplot 360 (Tecplot, Inc., Bellevue, Washington, USA) to compute hemodynamic responses within the aneurysm and at the aneurysm

neck. Aneurysmal and neck-plane root-mean-squared velocity magnitude (V_{RMS}), aneurysmal wall shear stress (WSS), and amount of flow crossing the aneurysm neck per second (or cross-neck flow, CNF) were computed for all the CFD simulations. The CFD results were also analyzed with JMP Pro (JMP, SAS Institute, Inc., Cary, North Carolina, USA), a statistical analysis software, to quantify the contribution of each geometric factor towards modifying a hemodynamic response.

3.3 Investigation of Cerebral Aneurysm Hemodynamics Using Particle Image Velocimetry

PIV is a powerful experimental laser-based flow measurement technique often used in cardiovascular research. A typical PIV setup includes a flow loop filled with blood analog fluid connected to an optically-clear vascular model, buoyant microsphere (fluorescent microspheres or glass beads) particles suspended in the fluid, a laser to illuminate the particles within the fluid, one or more cameras to capture the illuminated particles, and a PIV processing software. PIV calculates instantaneous flow velocities by measuring the displacement of flowing particles between image frames. This section describes the PIV process used to acquire the data presented in Chapters 4, 6 and 7.

3.3.1 Physical Modeling⁴

A subset of the computational idealized bifurcation aneurysm templates were translated into optically clear urethane models for flow experimentation using PIV using lost-core manufacturing technique. An example of the physical modeling process of an anatomical cerebral aneurysm is illustrated in Figure 3.8. The first step towards translating the computational model to a physical model was the printing of a wax core based on the computational geometry using a Solidscape[®] R66+ 3D printer (Solidscape[®], Inc., Merrimack, New Hampshire, USA), shown in Figure 3.8 (d). The wax model was then encapsulated in a silica-based and subsequently placed in a kiln. The wax within the investment was burned off, leaving a hollow channel in the shape of the computational model. Molten eutectic lead-tin-bismuth alloy was then poured into the silica channel, as shown in Figure 3.8 (d). The result was a metal core in the shape of the computational model. The metal core was extracted from the investment and then sanded and polished, depicted in Figure 3.8 (e). Optically clear urethane (PolyOptic 1411, Polytek Development Corp., Easton, Pennsylvania) was then poured around the metal core, and was cured in a pressure chamber to remove optical impurities caused by trapped gases. The metal core encapsulated by optically clear urethane is shown in Figure 3.8 (g). Following the curing, the metal core was evacuated from the urethane block by placing the model within a kiln at a temperature just above the metal's melting point. Remnant

⁴The physical modeling process was developed and performed by Dr. Justin Ryan as a doctoral student in the School of Biological and Health Systems Engineering at Arizona State University.

metal was removed with an acid bath. The final urethane model was sanded and polished to enhance optical clarity, and connected to a flow loop for PIV experiments. Figure 3.8 (h) and (i) depict the final aneurysm model and flow loop, respectively.

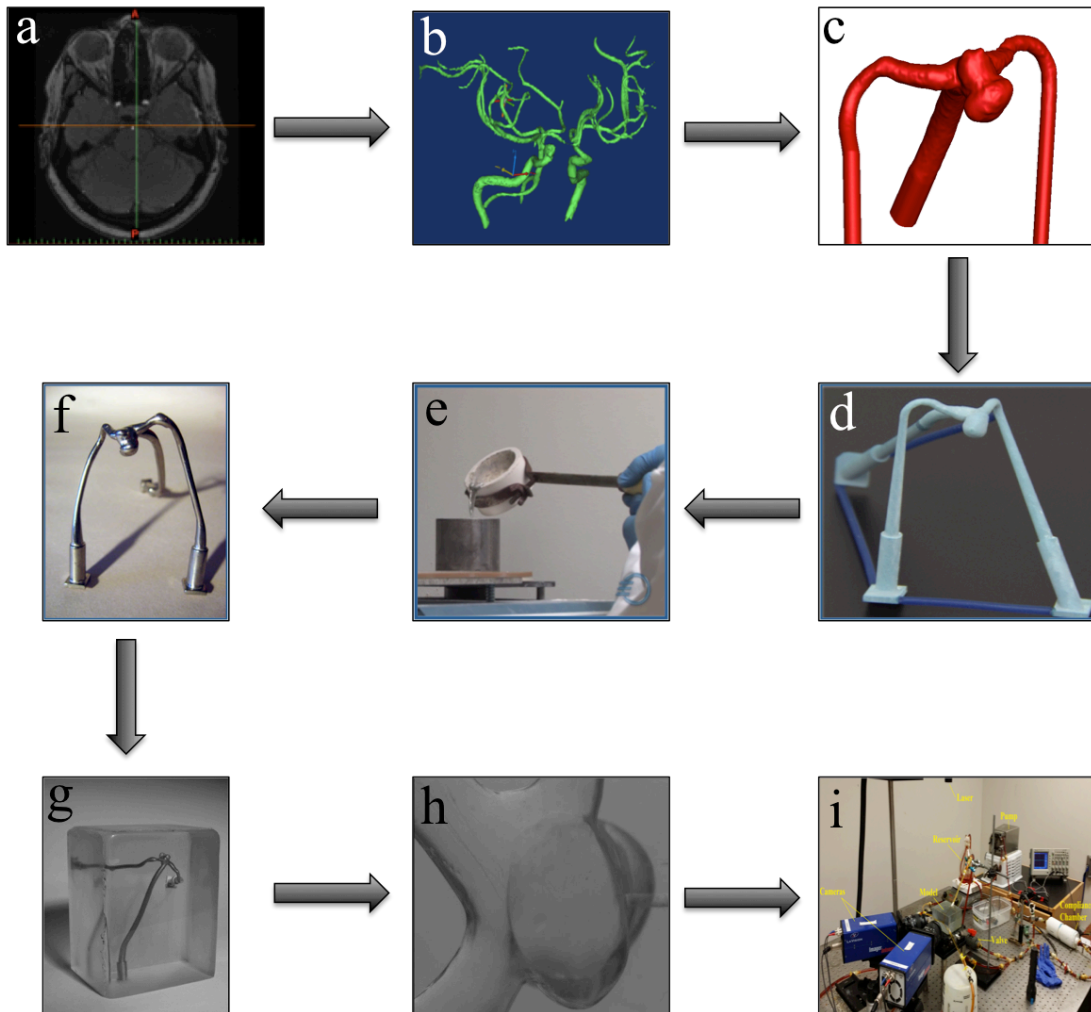


Figure 3.8: Physical model construction process for an anatomical cerebral aneurysm. (a) image acquisition, (b) segmentation and reconstruction of the cerebrovasculature, (c) creation of the 3D computational aneurysm model, (d) wax model constructed from the computational model, (e) and (f) metal re-cast of the wax model, (g) metal model encapsulated by clear urethane, (g) close up of the lost-core aneurysm model, and (h) experimental flow loop.

3.3.2 Flow Loop

The optically clear urethane models were mounted on a micrometer stage and connected to a flow loop, as shown Figure 3.9. A mixture of aqueous sodium iodide (NaI), glycerin and water was chosen as the blood analog. The blood analog had a density and viscosity of 1500 kg/m^3 and 3.86 cP . The blood analog fluid was also seeded with $8\mu\text{m}$ fluorescent microspheres (Thermo Scientific, Waltham, Massachusetts, USA) that experience peak excitation and emission at wavelengths of 542 nm and 618 nm , respectively. The refractive index of the blood analog fluid matched to that of urethane ($n = 1.49$), to prevent laser reflections between the urethane and the fluid.

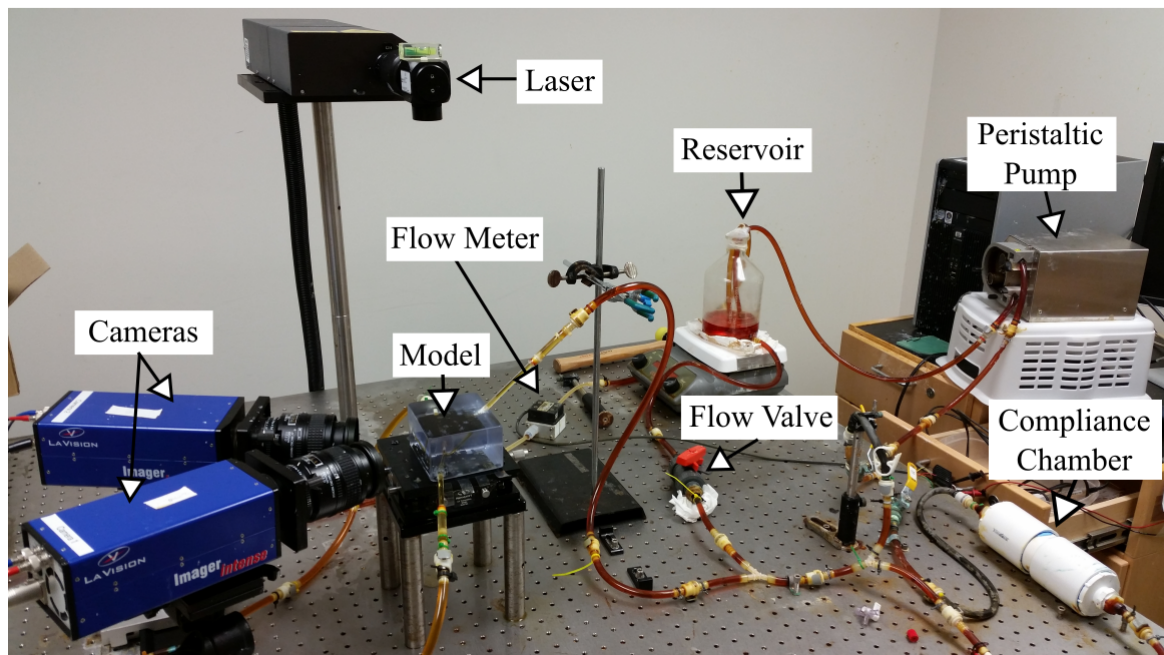


Figure 3.9: Photograph of the PIV system.

A peristaltic pump (Harvard Apparatus, Holliston, Massachusetts, USA) was used to drive the blood analog fluid through the flow loop. Since the pump inherently produced pulsatile flow pattern, an additional flow path including a variable compliance chamber was incorporated to provide a steady inflow. The variations in the dampened steady flow waveform, above or below the steady flow rate, were less than 5% of the steady flow rate. Valves were used to switch between the two inflow paths. Equal vascular resistances were imposed at the outlets. Inflow and outflow rates were controlled and monitored using a resistance valve and an infrared flowmeter (Omega Engineering, Inc., Stamford, Connecticut, USA).

3.3.3 Data Acquisition

Particle movement within the aneurysmal domain was captured by a Flow Master 3D Stereo-PIV system (LaVision, Ypsilanti, Michigan, USA). Light sheet from a dual-pulse, 532 nm Nd:YAG laser was used to illuminate the suspended fluorescent polymer microspheres within the aneurysmal volume. The light sheet, of 0.5 mm thickness, was formed by an optical arrangement of short-focal length cylindrical lens and a long focal length spherical lens housed within the laser unit. Two Imager Intense CCD cameras at a resolution of 1376 x 1040 pixels, with a pixel size of 6.45 μ m square, were used to capture the illuminated fluorescent particles. Each camera captured images corresponding to the laser exposure, i.e., camera 1 captured two particle images and camera 2 captured two particle images corresponding to the exposure 1 and exposure 2 of the dual-pulse

laser. The cameras were fitted with AF Micro-Nikkor 60 mm lens (Nikon, Tokyo, Japan), with lens f-numbers of 8, and were placed in a standard stereoscopic configuration as shown in Figure 3.10. The cameras were also fitted with low-pass optical filter to block unwanted laser reflections due to the model.

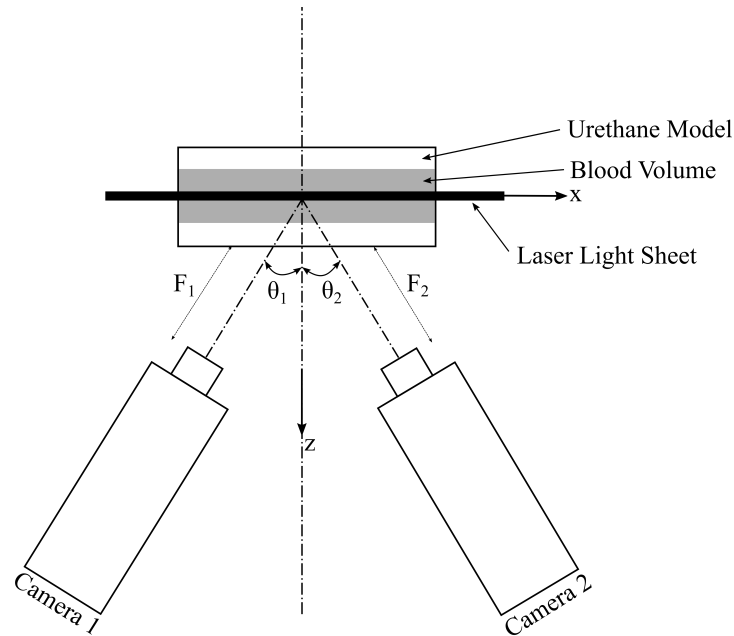


Figure 3.10: Standard configuration of a stereoscopic PIV system with two cameras. θ_1 and θ_2 , and F_1 and F_2 are the camera angles and the focal lengths of Camera 1 and Camera 2, respectively.

Steady and pulsatile inflow rates of 2, 3, and 4 mL/s were investigated, to match the CFD simulations. One hundred image pairs, taken at 5 Hz, were captured at three to five planes within the model to obtain volumetric flow information, at each flow rate. Images were acquired at the center plane (bisection the aneurysm, and inflow and outflow

vessels), and planes that were displaced orthogonally from the center plane by 0.5 mm. An example particle image (obtained at the center plane) is shown in Figure 3.11.



Figure 3.11: A particle image obtained during PIV data acquisition.

3.3.4 Camera Calibration

The particle images acquired from the CCD cameras have to be calibrated before further processing in order to relate the camera dimensions (pixels) to a spatial measurement (mm), and correct for any registration errors. A flat type-5 calibration plate, was attached to a urethane block, and placed at the location of the light sheet on the micrometer stage. The thickness of the urethane block was similar to the thickness between the outer edges of the aneurysm model to the center of the lumen. An image was acquired at the location of the light sheet, following which another image was acquired with the calibration plate

displaced from the light sheet by 0.5 mm. The markers on the calibration plate were then detected by DaVis Software (LaVision, Ypsilanti, Michigan, USA), as shown in Figure 3.12. Based on the detected marker positions, a mapping function was calculated based on the camera pin-hole model. A self-calibration process was also performed to minimize the root-mean-square (RMS) error, and to create a disparity map. Finally, the disparity correction was applied to correct for any unintentional alignment of the calibration plate and for changes in light sheet caused by laser reflections.

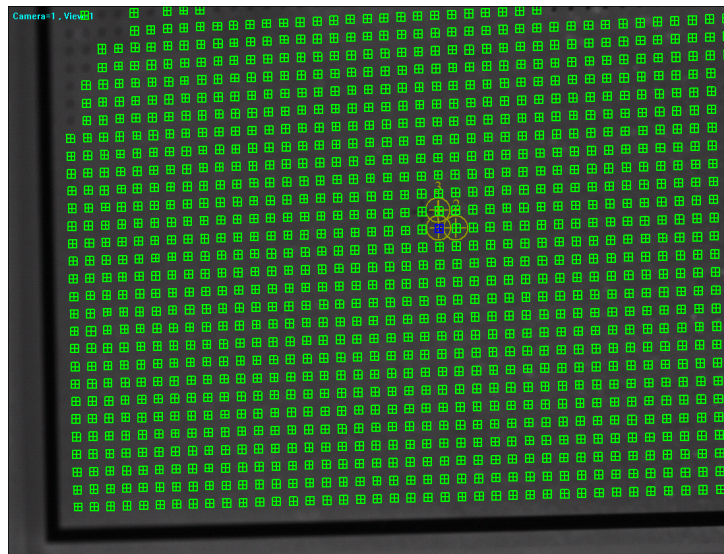


Figure 3.12: Marked flat type-5 calibration with software detected markers.

3.3.5 PIV Processing

PIV calculated the instantaneous velocity vector field by measuring the particle displacement between images, obtained during the first and second laser exposure, using

cross-correlation. Each particle image was subdivided into smaller regions, called interrogation spots or “windows”. A space-time cross-correlation of the particles lying within each window was then performed, as shown in Figure 3.13. Displacement peaks were calculated when the particle patterns matched, and the location of the highest peak determined the particle displacement [92].

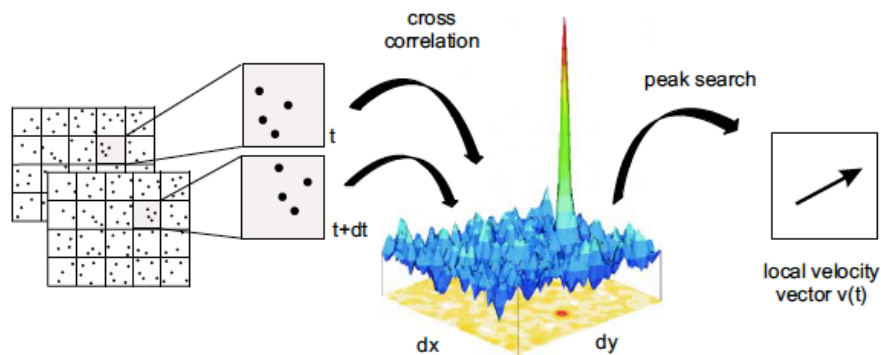


Figure 3.13: Calculation of particle displacement by comparing images obtained at two subsequent exposures using cross-correlation. Figure was reproduced from the LaVision FlowMaster Product-Manual.

The PIV algorithm within DaVis consists of three stages of processing: (1) image pre-processing, (2) vector calculation, and (3) vector post-processing. In the image pre-processing stage, the average of all 100 images is subtracted each particle image facilitating image background removal. The vector calculation stage involves setting up the PIV cross-correlation function. Multi-pass recursive cross-correlation algorithm was chosen to process the PIV images. Initial and final window sizes of 32×32 pixels and 16×16 pixels, respectively, with a window overlap of 50% were applied to the cross-correlation algorithm. Finally, spurious vectors were removed during vector post-

processing by (1) specifying an allowable vector range, (2) specifying a minimum peak-to-noise ratio⁵ (Q), (3) applying a median filter, and (4) specifying minimum number of vectors in a group. The peak-to-noise ratio is defined as the ratio of the highest correlation peak (P₁) to the second highest correlation peak (P₂), and is calculated as

$$Q = \frac{P_1 - \min}{P_2 - \min}, \quad (3.9)$$

where “min” is the lowest value of correlation. The median filter calculated the median of 9 neighboring vectors in the interrogation window and compared that value to the center vector. The center vectors were removed if the calculated median was greater than a specified value (for example, 2 times the R.M.S of the neighboring vectors). An example of the final vector field obtained from DaVis is shown in Figure 3.14.

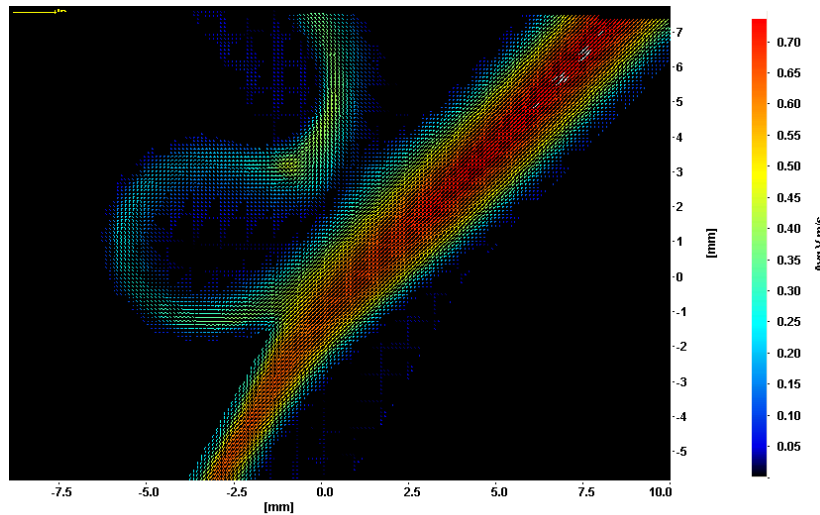


Figure 3.14: Velocity vector field (averaged) color-coded by velocity magnitude obtained after PIV processing in DaVis.

⁵ The value of Q should be as high as possible to accurately measure particle displacements

3.3.6 Analysis

The final averaged velocity vector fields were exported as Tecplot data files, and analyzed using an in-house Matlab (MathWorks, Naticks, Massachusetts, USA) to quantify hemodynamic responses such as V_{RMS} and CNF. The CNF was calculated as:

$$CNF = W \cdot L \left(\sum_{i=1}^n V_i \right), \quad (3.10)$$

where W is the window size, L is the laser sheet thickness, and V_i is the velocity at the neck-plane at the i^{th} point, and the V_{RMS} was calculated as:

$$V_{RMS} = \sqrt{\frac{1}{n} \sum_{i=1}^n |V_i|}. \quad (3.11)$$

The hemodynamic responses calculated from PIV were then compared directly to the corresponding responses obtained using CFD for validation.

CHAPTER 4

EFFECTS OF GEOMETRIC VARIATIONS ON IDEALIZED BIFURCATION

ANEURYSM HEMODYNAMICS

4.1 Introduction

Branching points of major arteries in the Circle of Willis are common sites for the formation of cerebral aneurysms [93]. Complex hemodynamics at the branching points promote in vascular remodeling, leading to the cerebral aneurysm initiation [94]. The influence of aneurysm geometry on cerebral aneurysm evaluation and treatment planning has been described in detail in Chapter 2. Additionally, cerebral aneurysm geometry has been established as the primary driver of hemodynamics, and can influence growth and/or rupture, and effectiveness of treatment outcomes [45], [95].

In this chapter, the effects of geometric variations on idealized basilar tip aneurysm (IBTA) hemodynamics have been quantified in order to attribute specific hemodynamic features to geometric underliers that are routinely quantified in clinical practice. Basilar tip aneurysms (BTAs) were chosen in part because aneurysms at the basilar artery bifurcation have been associated with greater risk of rupture [4], [13], [93], [96]. Furthermore, the location of the aneurysm in the circle of Willis is a dangerous and difficult region to access with surgical clipping. Toward this end, a design of experiments is employed based on parallel computational and bench-top data. The statistical relationships between geometry and flow that emerge have the potential to play a valuable role in current clinical practices for evaluating cerebral aneurysms and planning

their treatments. Methods and results specific to the IBTA templates are discussed in this chapter.

4.2 Methods

4.2.1 Study Design

Changes in aneurysm geometry were parameterized in terms of three geometric factors (i.e., DS, DNR, and IA), and hemodynamic effects were parameterized in terms of four responses (i.e., aneurysmal WSS, aneurysmal and neck-plane V_{RMS} , and CNF). Schematic representations of each geometric factor (and values used) are presented in Figure 4.1, to facilitate the creation of a two-level full factorial design.





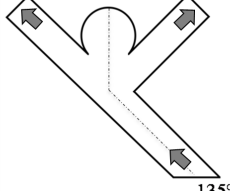
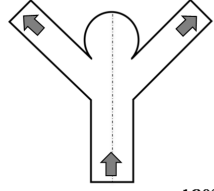
	Low	High
Dome Size	 4 mm	 6 mm
Dome-to-Neck Ratio	 3:2	 2:1
Inflow Angle (Bifurcation Aneurysm)	 135°	 180°

Figure 4.1: Schematic representation of the three investigated geometric factors. The directions of inflow and outflows are marked by arrows in the drawing.

Eight unique combinations of the three investigated geometric factors were generated using a 2^3 full factorial design, as shown in Figure 4.2. The corners of the cube represent the different models, or geometric templates, each corresponding to low or high levels of the three factors. For example, the label **1(4,3:2,135)** refers to the first IBTA model (**IBTA-1**) with 4 mm DS, **3:2** DNR, and **135°** IA. The edges of the cube are color-coded to represent a change in one geometric factor, with the other two factors held constant, and the arrows indicate an increase in factor value. Red edges correspond to a change in DS (increasing from 4 mm to 6 mm with the red arrow), green edges correspond to a change in DNR (increasing from 3:2 to 2:1 with the green arrow), and blue edges correspond to a change in IA (increasing from 135° to 180° with the blue arrow).

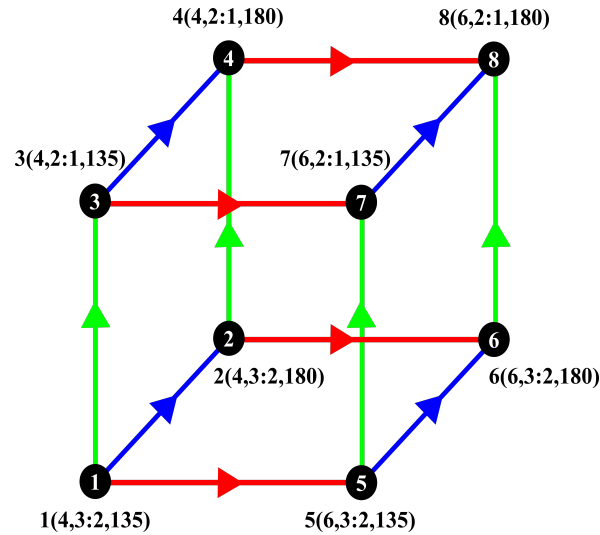


Figure 4.2: Cube representing a two-level full factorial experimental design based on three geometric factors: dome size, dome-to-neck ratio, and inflow angle.

To determine if the hemodynamic responses observed for the idealized templates could potentially be translated to more realistic patient-specific geometries, two anatomical BTA (or ABTA) models that were similar to two of the IBTA templates were also examined. The first ABTA model, ABTA-1, had a DS of 9.59 mm and DNR of 2.8, and the second ABTA model, ABTA-2, had a DS of 14.24 mm and DNR of 1.4. The IAs for both anatomical models were approximately 180° . ABTA-1 and 2 matched closely to the geometric configurations of IBTA-4 (DS = 4 mm, DNR = 2:1, and IA = 180°) and IBTA-6 (DS = 6 mm, DNR = 3:2, and IA = 180°). Although the anatomical models had larger domes as compared to the corresponding idealized templates, the proportional increase in DS between ABTA-1 and ABTA-2 were comparable to the increase in DS between IBTA-4 and IBTA-6 (i.e., roughly 1.5 times). Furthermore, according to standard clinical convention, the DNRs of the anatomical aneurysms correspond to narrow-neck and wide-neck aneurysms, as do IBTA-4 and IBTA-6.

4.2.2 Computational Methods

4.2.2.1 Computational Model Construction

The eight idealized computational cerebral aneurysm templates were designed in SolidWorks (Dassault Systemès, Waltham, Massachusetts, USA). The aneurysm templates were modeled after a DSA image of a basilar tip aneurysm as shown in Figure 3.1 (a). The aneurysms were constructed as spheres, and the inlet and outlet vessels were modeled as 4 mm diameter cylinders. DS, DNR and IA values were imparted to the

models as reported in Figure 4.2, and shown in Figure 4.3. The directions of inflow and outflows are also represented in Figure 4.3 within the first template (IBTA-1). To create the two anatomical aneurysm models, patient-specific CT image datasets were segmented and reconstructed using Mimics (Materialise, Leuven, Belgium). The underlying CT data had image matrix sizes of 512 by 512 pixels, pixel dimensions of 0.5 mm square, and slice thicknesses of 0.625 mm.

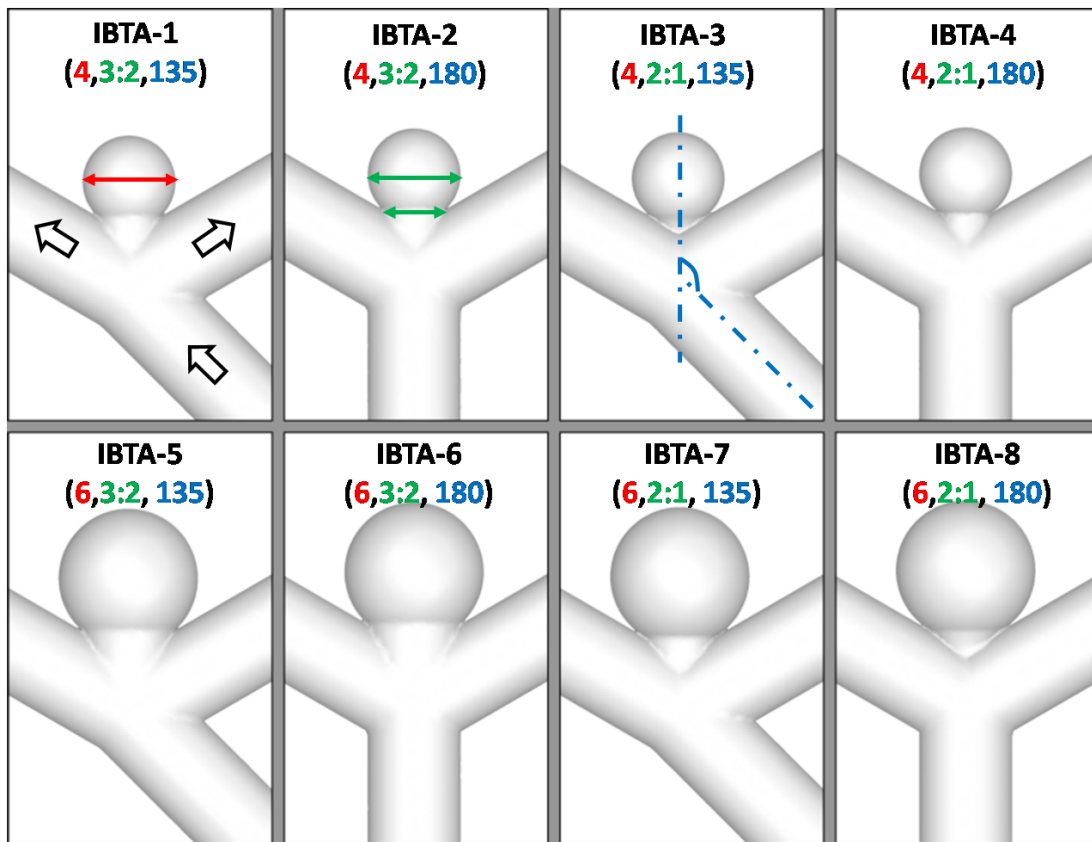


Figure 4.3: Computational IBTA templates. The numbers in red, green, and blue represent the DS (in mm), DNR (no units), and IA (in degrees), respectively. The black arrows represent the directions of inflow and outflows.

4.2.2.2 Computational Fluid Dynamics

The computational templates were prepared for CFD simulations in ANSYS ICEM 14.1 (ANSYS, Inc., Canonsburg, Pennsylvania, USA), where the blood volume was discretized into unstructured tetrahedral mesh elements using the Octree approach. To ensure that the hemodynamic parameters investigated were independent of mesh size, a mesh refinement study was performed on the base model (IBTA-1) by decreasing the maximum element size from 0.5 to 0.2 mm. Steady flow simulations at 3 mL/s were performed for all mesh sizes. The final mesh size was deemed acceptable when the change in V_{RMS} between subsequent mesh sizes were less than 1%, and change in WSS was less than 5%. The final meshes (for all simulations) ranged between 6.1 to 7.1 million elements.

The meshed geometries were then imported into ANSYS Fluent to perform steady and pulsatile flow simulations with inflow rates of 2, 3 and 4 mL/s, corresponding to Reynolds numbers of 247.39, 371.09, and 494.78, respectively. These flow rates span the range of normal, exercise and diseased flow rates reported in literature [88]. The models were assumed to be rigid, and a no-slip boundary condition was applied at the vessel wall. Blood was assumed to be incompressible and Newtonian, with a density of 1500 kg/m³ and viscosity of 3.86 cP. The density and viscosity were chosen to match the blood analog solution used for PIV experiments (described later). User-defined parabolic flow profiles were prescribed at the inlet for the steady simulations, and Ford vertebral artery flow waveforms (Ford et al., 2005) were used for the pulsatile simulations. Three cardiac

cycles were simulated for the pulsatile simulations, and minimum and maximum time-step sizes of 1 ms and 3 ms were specified for the third cardiac cycle using the adaptive time-stepping technique in Fluent. Zero-pressure boundary conditions were imposed at the outlets. Pressure-velocity coupling was specified according to the SIMPLE algorithm, and a second order upwind scheme was used for momentum discretization.

4.2.3 Experimental Methods

4.2.3.1 Physical Model Construction

A subset of the IBTA templates was chosen for validation with PIV. A fractional factorial design was employed to select five of the eight IBTA models, depicted by the orange bubbles in Figure 4.4. This allowed for experimental examination of model pairs with changes in each individual geometric factor, as well as a model pair with changes in all geometric factors concurrently. Experiments were also conducted on ABTA-1 and ABTA-2. Inflow rates of 2, 3 and 4 mL/s were explored under steady and pulsatile flow conditions (for all experimental models) in order to match the CFD simulations. The physical models were then constructed using a lost-core manufacturing technique, as explained in Section 3.3.1. An example of a physical urethane IBTA model is shown in Figure 4.5.

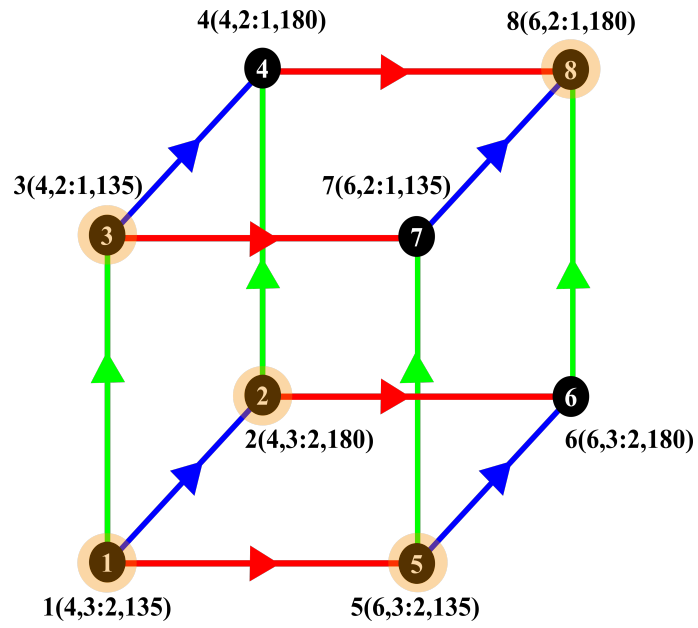


Figure 4.4: Cube representing a full factorial design of DS, DNR and IA. The orange bubbles represent the five IBTA templates chosen for PIV experimentation based on a fractional factorial design.



Figure 4.5: A physical urethane model (IBTA-1).

4.2.3.2 Particle Image Velocimetry

The optically clear urethane models were mounted on a micrometer stage and connected to the flow loop, as described in Section 3.3.2 and as illustrated in Figure 3.9. Volumetric flow data within the aneurysm models were acquired with a FlowMaster 3D stereo-PIV system (LaVision, Inc., Ypsilanti, Michigan, USA). A 532 nm Nd:YAG laser was used to illuminate the fluorescent particles flowing through the model and two CCD cameras, fitted with low pass filters to block laser reflections, were used to capture the particle images. One hundred images, taken at 5 Hz, were captured at different planes within the aneurysmal volume. Images were captured at the center plane (bisecting the aneurysm dome, inlet and outlet vessels), and planes displaced orthogonally from the center plane at 0.5 mm intervals in each direction. A total of three and five planes were captured for the small (4 mm) and large (6 mm) aneurysm models, respectively. PIV processing applied a recursive cross-correlation algorithm using the DaVis software (LaVision, Inc., Ypsilanti, Michigan, USA), where initial and final window sizes of 32 by 32 pixels and 16 by 16 pixels were applied. PIV processing technique, using DaVis, has been described in Section 3.3.5.

4.2.4 Data Analysis

4.2.4.1 Computational Data Analysis

Geometric factors were specified for the idealized models (or measured in the anatomical cases) and hemodynamic responses for each model were calculated by analyzing CFD results with Tecplot 360 (Tecplot, Inc., Bellevue, Washington, USA). WSS was averaged over the distal part of the aneurysm dome (excluding the neck), and CNF was calculated as the cumulative volume of fluid crossing the neck-plane of the aneurysm per unit time. For pulsatile cases, the hemodynamic responses were averaged over 10 or more different time points spaced equidistant from one another throughout the third cardiac cycle. Geometric factor main effects analysis was then performed on data from the idealized templates (using JMP Pro (JMP, SAS Institute Inc., Cary, North Carolina, USA)) in order to quantify the percent contributions that individual geometric factors (and their interactions) made to effects on hemodynamic responses. Specifically, regression analysis using standard least squares estimation was used to generate the sum of squares (SS) for each of the factors and their interactions. Contributions of the geometric factors (and their interactions) toward modifying hemodynamic responses were then calculated by dividing individual SS values by the total SS. More detail on related statistical analyses can be found in [97]. Hemodynamic responses were also compared directly between the ABTA models and their matching IBTA counterparts using Pearson correlation [98]. Please note that in the remainder of this chapter ordered pairs of values are used to denote results corresponding to steady and pulsatile flow conditions in the following order: (steady flow result, pulsatile flow result).

4.2.4.2 Experimental Data Analysis

Experimental flow data were analyzed using an in-house code written in MATLAB (MathWorks, Natick, Massachusetts, USA) to calculate V_{RMS} within the aneurysm and at the neck-plane. For pulsatile cases, these responses were averaged over three different time points of the cardiac cycle: mid systole (at 280 ms), peak systole (at 570 ms), and mid diastole (at 840 ms). The experimental hemodynamic responses were then compared directly to the corresponding responses from CFD (for both the IBTA and ABTA models) to facilitate validation.

4.3 Results

4.3.1 Idealized Aneurysm Models (Templates)

4.3.1.1 Computational Results

The changes in hemodynamic responses after changing one geometric factor across a pair of models (and holding the other two factors constant) are presented in Table 4.1. Increasing DS from 4 mm to 6 mm increased all hemodynamic responses (except for WSS in one model). On average over the three flow rates, increasing DS increased aneurysmal V_{RMS} by (74.10%, 54.22%), neck-plane V_{RMS} by (53.76%, 34.93%), aneurysmal WSS by (149.73%, 90.29%), and CNF by (196.69%, 189.30%). In contrast, increasing DNR from 3:2 to 2:1 decreased all hemodynamic responses across all models, changing aneurysmal V_{RMS} by (56.04%, 56.55%), neck-plane V_{RMS} by (46.53%,

43.16%), aneurysmal WSS by (63.88%, 68.38%), and CNF by (59.69%, 56.99%). Figure 4.6 illustrates the effects of changing DS (from black to red) and DNR (from black to green) on aneurysmal V_{RMS} and WSS, respectively, at 3 mL/s steady and pulsatile inflow rates. In general, increasing IA from 135° to 180° increased only the neck-plane hemodynamic responses, neck-plane V_{RMS} by (36.98%, 37.75%) and CNF by (28.71%, 30.07%). On the other hand, the 135° templates generated overall greater WSS magnitudes as compared to their 180° counterparts, by (40.12%, 41.87%), as illustrated by the color maps in Figure 4.7.

Table 4.1: Percentage changes in hemodynamic responses after changing one geometric factor, keeping the other two factors constant, for all different flow rates.

Changed factors	Constant factors (factor 1; factor 2)	Flow rate (mL/s)	Aneurysmal WSS (%)		Aneurysmal V_{RMS} (%)		Neck-plane V_{RMS} (%)		Cross-neck flow (%)	
			Steady	Pulsatile	Steady	Pulsatile	Steady	Pulsatile	Steady	Pulsatile
Dome size (4 to 6 mm)	(3:2;135°)	2	137.70	125.95	94.93	92.69	88.07	70.51	241.55	220.29
		3	83.74	87.94	66.31	69.89	68.52	57.59	204.64	265.18
		4	64.22	65.93	54.22	54.88	60.43	47.70	189.34	376.88
	(3:2;180°)	2	-30.91	-37.18	38.36	51.52	69.32	30.45	74.59	174.38
		3	-53.49	-40.98	9.36	17.95	78.37	36.21	267.69	149.57
		4	-41.79	-15.18	10.20	-35.72	35.33	31.46	196.34	160.19
	(2:1;135°)	2	473.34	144.00	168.72	124.36	86.08	40.00	293.87	216.26
		3	296.48	259.37	122.71	104.00	68.92	34.62	250.00	204.97
		4	224.45	190.60	102.44	85.25	62.05	29.83	233.24	177.80
	(2:1;180°)	2	289.18	164.90	98.28	33.48	16.02	23.90	154.22	149.31
		3	210.01	51.21	68.60	25.40	6.98	1.50	130.27	92.86
		4	143.85	86.94	55.12	26.93	4.97	15.43	124.50	83.89
Dome-to-neck ratio (3:2 to 2:1 mm)	(4 mm;135°)	2	-88.18	-72.54	-68.23	-61.05	-45.54	-33.54	-60.45	-54.86
		3	-83.44	-80.76	-63.03	-57.52	-41.84	-31.17	-57.40	-49.43
		4	-80.02	-76.78	-60.03	-54.80	-40.45	-30.73	-56.38	-10.74
	(4 mm;180°)	2	-91.19	-88.94	-69.21	-49.88	-44.73	-49.96	-65.86	-69.37
		3	-85.11	-76.79	-61.97	-57.57	-40.11	-38.86	-62.33	-61.59
		4	-77.87	-80.61	-57.87	-78.98	-39.05	-47.28	-61.26	-61.47
	(6 mm;135°)	2	-71.50	-70.35	-56.21	-54.65	-46.12	-45.43	-54.39	-55.43
		3	-64.27	-63.21	-50.49	-48.99	-41.70	-41.20	-51.06	-57.77
		4	-60.54	-59.34	-47.53	-45.93	-39.85	-39.10	-49.76	-48.00
	(6 mm;180°)	2	-50.37	-53.38	-55.88	-55.85	-62.13	-52.47	-50.30	-72.17
		3	-0.77	-40.55	-41.37	-54.89	-64.08	-54.44	-76.41	-70.31
		4	-7.30	-57.26	-40.70	-58.50	-52.73	-53.71	-70.65	-72.77
Inflow Angle (135° to 180° mm)	(4 mm;3:2)	2	-30.02	-39.28	8.79	-6.97	50.42	65.33	50.62	45.68
		3	-14.61	-9.75	18.76	34.49	52.39	68.77	53.04	69.60
		4	-9.91	2.53	22.84	168.94	53.01	64.97	54.07	172.95
	(4 mm;2:1)	2	-47.82	-75.55	5.44	19.69	52.65	24.49	30.00	-1.13
		3	-23.23	8.86	22.14	34.33	56.90	49.92	35.32	28.82
		4	-0.20	-14.36	29.47	25.03	56.61	25.55	36.83	17.84
	(6 mm;3:2)	2	-79.66	-83.12	-22.78	-26.85	35.42	26.49	-23.01	24.80
		3	-78.39	-71.66	-21.91	-6.62	61.29	45.88	84.71	15.90
		4	-68.07	-47.59	-12.22	11.62	29.08	46.83	57.80	48.92
	(6 mm;2:1)	2	-64.58	-73.46	-22.20	-28.79	-4.82	10.18	-16.09	-22.06
		3	-39.97	-54.20	-7.54	-17.43	-0.63	13.03	-10.97	-18.53
		4	-24.99	-44.91	-0.80	-14.33	1.44	11.62	-7.82	-22.00

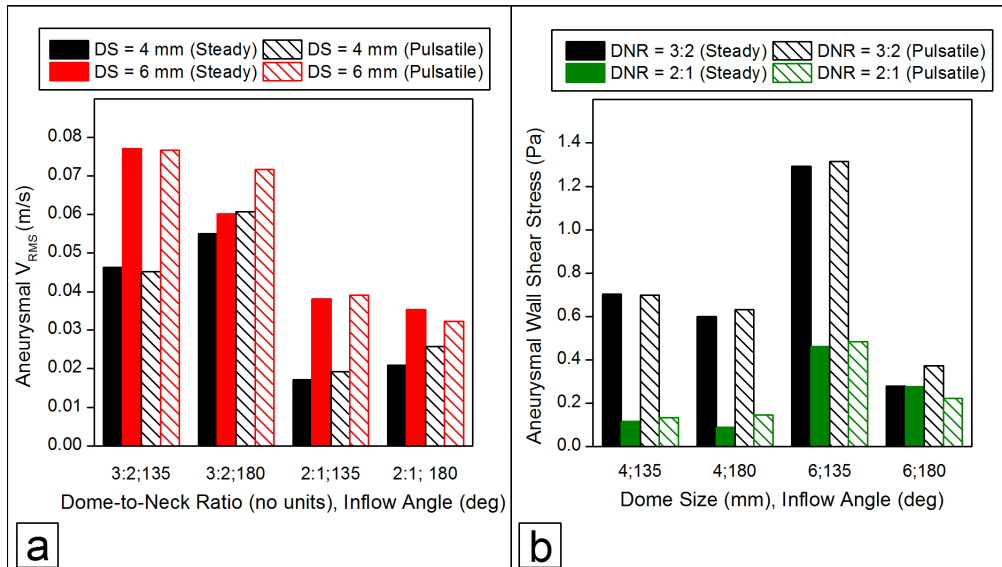


Figure 4.6: (a) Effects of dome size change on aneurysmal V_{RMS} (keeping dome-to-neck ratio and inflow angle constant within grouped bars) and (b) effects of dome-to-neck ratio change on aneurysmal wall shear stress (keeping dome size and inflow angle constant within grouped bars). Solid and patterned colors correspond to 3mL/s steady and pulsatile CFD simulations, respectively, in the idealized model templates.

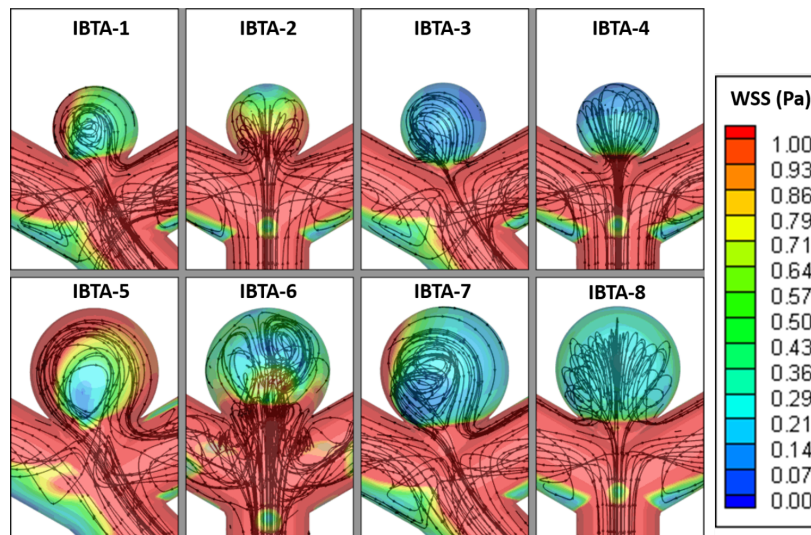


Figure 4.7: Illustrations of intra-aneurysmal flow patterns from CFD with black streamtraces and color-coded wall shear stress overlays at 3 mL/s steady inflow.

Aneurysmal DNR made the greatest contributions to effects on hemodynamic responses (as much as 75.05% to pulsatile aneurysmal V_{RMS} and over 35% to every response). DS made the next greatest contributions (as much as 43.94% to pulsatile CNF and over 20% to all responses except WSS). Figure 4.8 illustrates the contributions that individual geometric factors and their interactions made to the effects on hemodynamic responses under steady and pulsatile inflow conditions. Although the contributions made by IA in the figure were less prominent than those made by DS and DNR, IA did contribute over 10% of the effects on aneurysmal WSS and neck-plane V_{RMS} . Several contributions of factor interactions in the figure, IA with DS or DNR for example, also exceeded 10%.

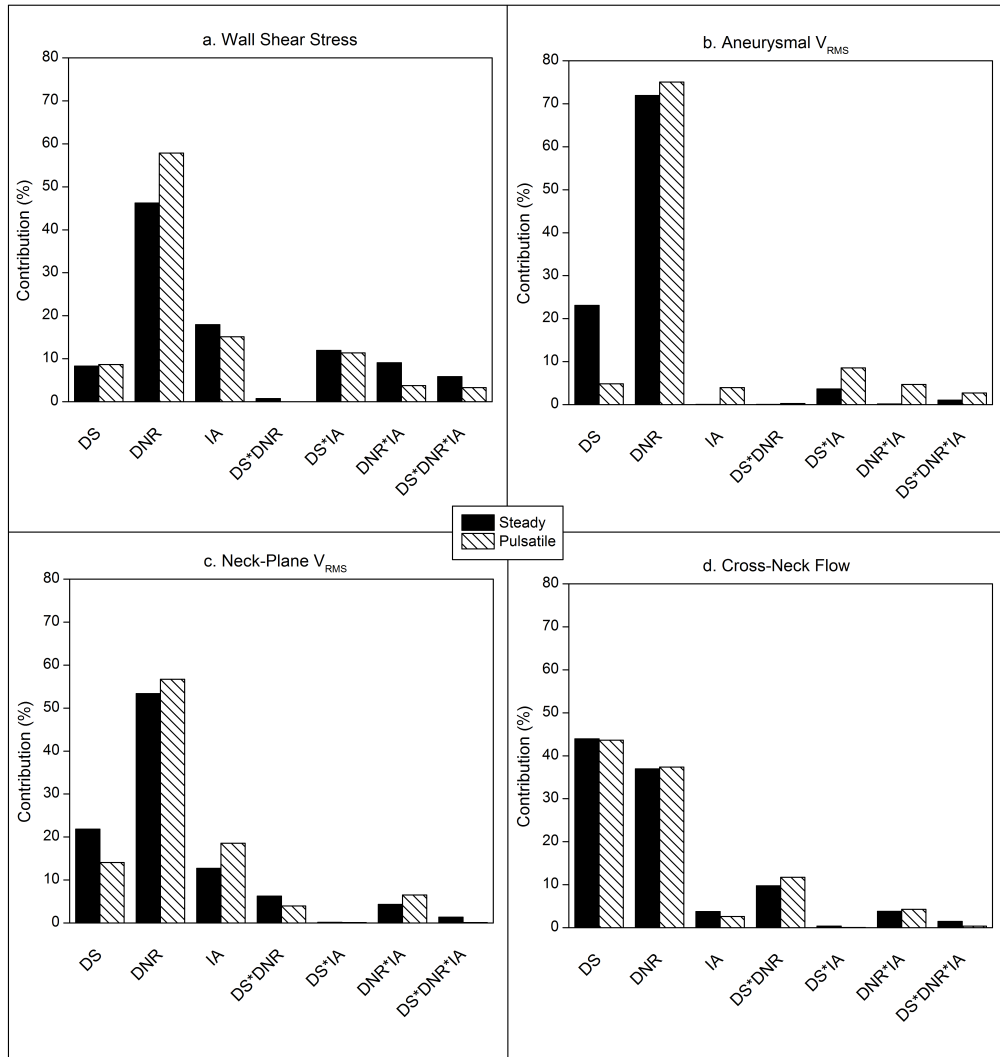


Figure 4.8: Contributions made by individual geometric factors, and their interactions, to effects on simulated hemodynamic responses under steady (solid boxes) and pulsatile (patterned boxes) inflow conditions in the idealized templates.

4.3.1.2 Experimental Results

Aneurysmal and neck-plane V_{RMS} values were also calculated based on PIV results to

validate the corresponding values calculated based on CFD results. Aneurysmal V_{RMS} values from both PIV and CFD are shown in Figure 4.9 for 3 mL/s steady and pulsatile inflows in the idealized models. Although aneurysmal V_{RMS} values (averaged across all flow rates) were (33.49%, 33.53%) greater for PIV, the general trends associated with changes in DS, DNR, and IA were similar across the idealized PIV and CFD datasets. Specifically, for the six different sets of flow conditions (three flow rates and two flow types), correlations between series of simulated and experimental V_{RMS} values (from the four different geometric templates corresponding to single factor changes) ranged from 0.61 to 0.98 with an average correlation of 0.74. For example, the correlation between the steady flow PIV and CFD results presented in Figure 4.9 was 0.70. A qualitative comparison of the center-plane PIV and CFD flow fields from model IBTA-1 at mid-systole for a 3 mL/s pulsatile inflow rate is presented in Figure 4.10.

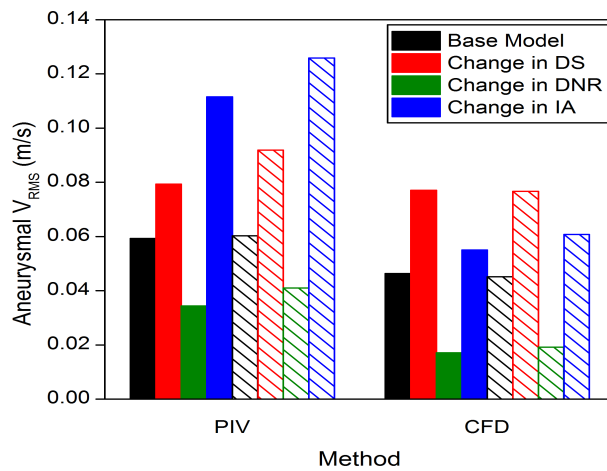


Figure 4.9: Comparisons between aneurysmal V_{RMS} values from PIV and CFD when changing the dome size (black to red), dome-to-neck ratio (black to green), and inflow angle (black to blue). Solid and patterned boxes correspond to 3 mL/s steady and pulsatile inflows, respectively, in the idealized aneurysm models.

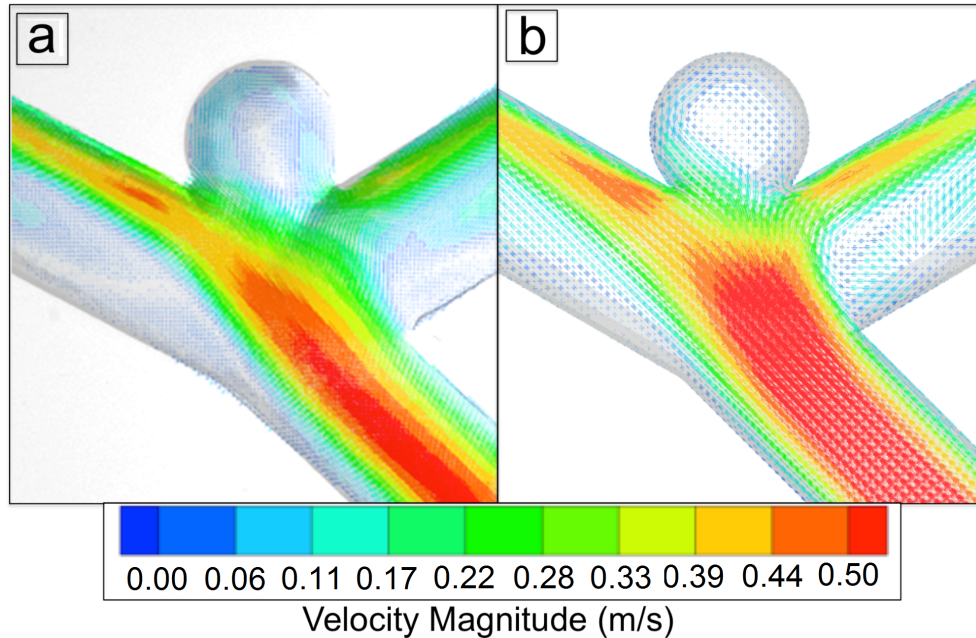


Figure 4.10: (a) PIV and (b) CFD flow fields color-coded by velocity magnitude in IBTA-1 at mid-systole for a 3 mL/s pulsatile inflow.

4.3.2 Anatomical Aneurysm Models

4.3.2.1 Computational Results

Aneurysmal V_{RMS} and WSS values were calculated for the anatomical models (ABTA-1 and ABTA-2) based on CFD. Hemodynamic trends between ABTA-1 and ABTA-2 were similar to those between their idealized counterparts IBTA-4 and IBTA-6. Specifically, the aneurysm models with lower DS and higher DNR (i.e., ABTA-1 and IBTA-4) demonstrated lower V_{RMS} and WSS as compared to the corresponding aneurysm models with higher DS and lower DNR (i.e., ABTA-2 and IBTA-6). The trending among anatomical and idealized counterparts is highlighted in Figure 4.11 where simulated WSS

values are shown for 3 mL/s steady and pulsatile inflows. The two data series there correlate with a value of 0.91; however, the average aneurysmal V_{RMS} and WSS values from the anatomical models were 2.62 and 6.54 times greater, respectively, than the corresponding values from the idealized models. Figure 4.12 displays streamtraces from CFD (color-coded by velocity magnitude) throughout the anatomical aneurysm geometries and their corresponding idealized templates, both at 3 mL/s steady inflow. Features of the simulated intra-aneurysmal flow patterns were qualitatively similar between the anatomical geometries and their idealized counterparts.

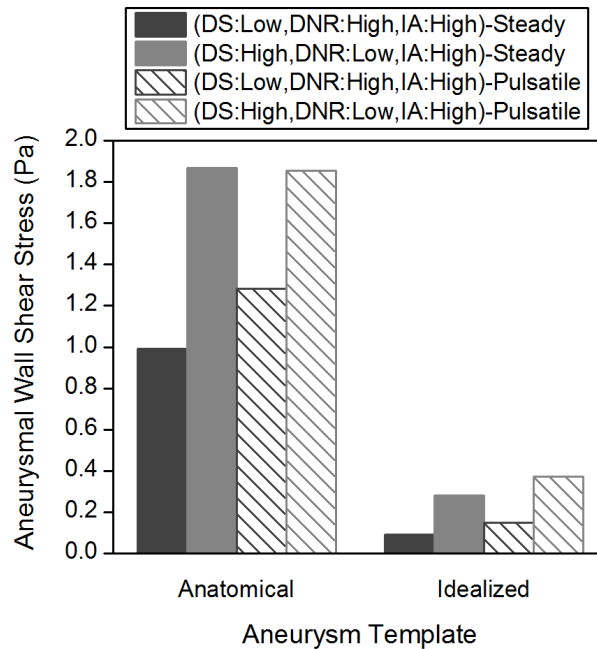


Figure 4.11: Simulated aneurysmal wall shear stress in anatomical and idealized basilar tip aneurysm templates at 3 mL/s steady and pulsatile inflow.

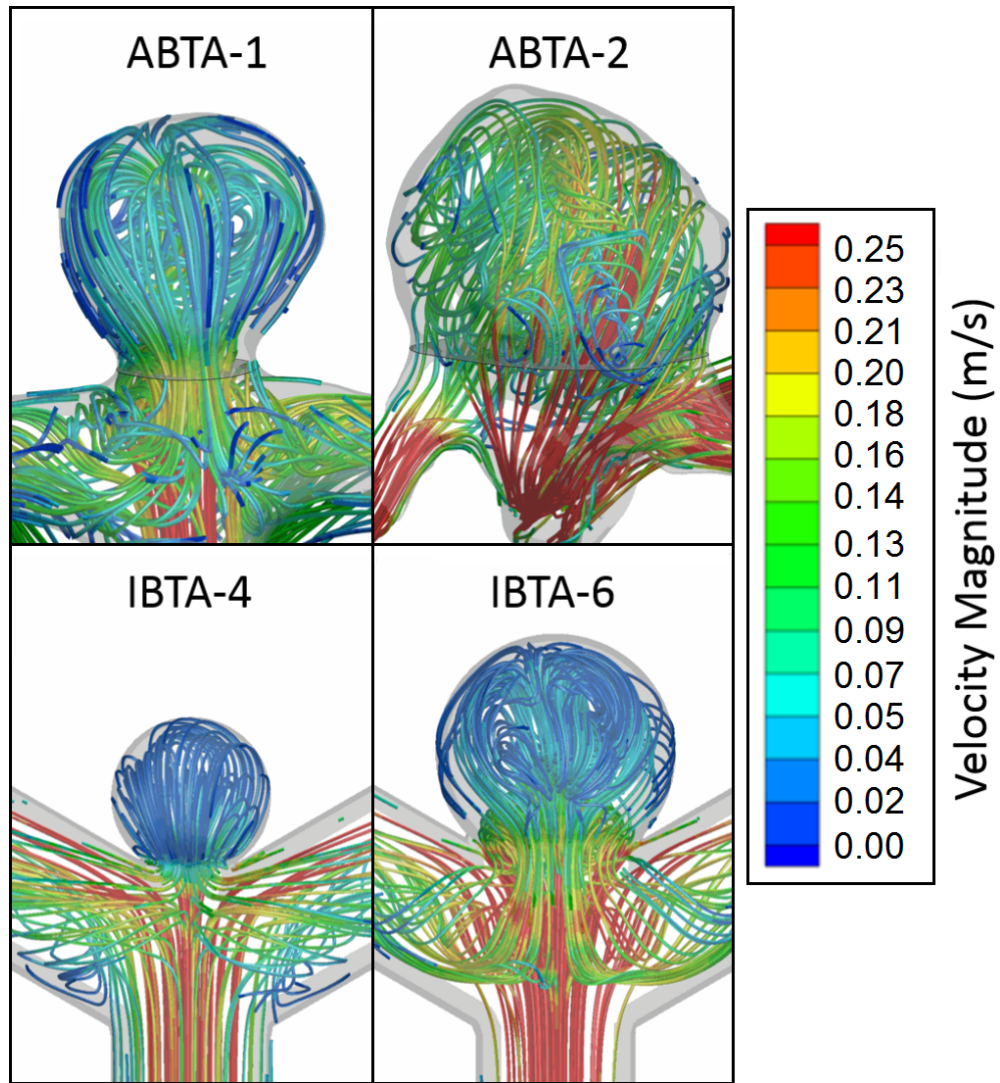


Figure 4.12: Illustrations of intra-aneurysmal flow patterns color-coded by velocity magnitude from CFD in (top) anatomical and (bottom) idealized cerebral aneurysm templates, both at 3 mL/s steady inflow.

4.3.2.2 Experimental Results

Aneurysmal V_{RMS} values were also calculated for the anatomical models based on PIV in order to validate the anatomical CFD data. V_{RMS} values were (17.86%, 26.41%) greater

(averaged over models and flow rates) for the experimental data as compared to the simulated data. However, V_{RMS} increased similarly from ABTA-1 to ABTA-2 in experiments and simulations, by (32.42%, 32.95%) and (36.44%, 46.29%), respectively, on average across flow rates.

4.4 Discussion

Geometry is known to play an important role in cerebral aneurysm hemodynamics and thus aneurysmal growth and/or rupture. This study investigated the contributions made by three geometric factors (DS, DNR, and IA) to effects on BTA hemodynamics. Flows within idealized geometric templates and anatomical geometries were simulated using CFD and measured using PIV. Aneurysmal WSS, V_{RMS} within the aneurysm and at the neck, and CNF were evaluated as hemodynamic responses. To the author's knowledge, this study represents the first time that a factorial design has been applied to characterize the relationships between aneurysmal geometry and hemodynamics. We believe that bridging the gap between the two bases in a quantitative yet practical way has potential to play a valuable role in clinical decision-making.

4.4.1 Effects of Geometric Main Factors on Hemodynamics

Individually, all three investigated geometric factors affected hemodynamics. Foremost among them was DNR, which is routinely evaluated in clinical practice. We observed

that aneurysm templates with low DNR (3:2) generated greater hemodynamic responses (e.g., low DNR increased CNF, aneurysmal V_{RMS} , and WSS by (59.69%, 56.99%), (56.04%, 56.55%), and (63.38%, 68.38%), respectively, on average across flow rates). This is important because greater CNF, aneurysmal V_{RMS} , and WSS may contribute to cerebral aneurysm growth and/or rupture according to [35], [99].

Aneurysmal DS has been clinically established as a strong independent predictor of rupture [5] and, like DNR, is routinely evaluated. Main effects analysis of geometric factors showed that DS made the greatest contributions to effects on CNF, and made the second greatest contributions to effects on other hemodynamic responses. More specifically, templates with larger DS had higher values of computed hemodynamic responses (e.g., high DS increased aneurysmal V_{RMS} by (74.10%, 54.22%)). From a clinical perspective, larger aneurysms are at greater rupture risk than smaller aneurysms [5], which correlates with our finding that higher velocities were present in larger-domed aneurysms. Not surprisingly, the combination of high DS and low DNR (i.e., large, wide-neck terminus aneurysms) produced the most extreme hemodynamic environments in this study based on all of the hemodynamic responses.

Multiple studies have reported the impact of IA on hemodynamics in cerebral aneurysms [35], [46], [94]. Greater inflow angles have been associated with elevated levels of hemodynamic responses that may promote aneurysmal growth and/or re-growth [46]. As expected, CNF and V_{RMS} at the neck were greater for the 180° aneurysm templates by (28.71%, 30.07%) and (36.98%, 37.75%), respectively. A IA of 135°, however, elevated aneurysmal WSS by (40.12%, 41.87%), which may be due to intra-aneurysmal flow patterns like those illustrated in Figure 4.7. The 135° templates led to

regions of flow impingement along the left (from the reader's perspective) aneurysmal wall whereas more dispersed flow patterns were observed in the 180° templates. Figure 4.7 also shows that the combination low DS and high IA produced high WSS within the aneurysm. Whether high or low WSS is detrimental remains a topic of debate [28]. For example, Shojima et al. reported that higher WSS plays an important role in aneurysm formation but lower WSS contributes to growth [42].

Several combinations of geometric factors also made considerable contributions to effects on cerebral aneurysm hemodynamics, the most prominent of which were the combinations of IA with DS or DNR. The interactions of these factors made contributions of greater than 10% to effects on multiple hemodynamic responses, which shows that although individual geometric factors alone affect flow, combinations of factors may also play a role in determining hemodynamics and should thus be considered in cerebral aneurysm treatment planning accordingly. Characterizing pre-treatment aneurysmal geometries in terms of both individual and interacting factors may provide a more complete understanding of an aneurysm's hemodynamic underpinnings for physicians to use in developing well-informed hemodynamic modification plans.

4.4.2 Comparisons with Experimental Results

PIV was performed on five of the eight IBTA models (and the two ABTA models) for the purpose of validation. Discrepancies were observed between V_{RMS} values measured with PIV and those computed with CFD for the idealized models (the PIV values were

(33.49%, 33.53%) greater on average across flow rates). However, the trends in responses remained similar across investigated flow rates and types (the average correlation was 0.74) as illustrated in Figure 4.9. Differences between computational and experimental results may be due to differences in aneurysmal neck sizes between the computational and physical models that resulted from inexact casting of the urethane models. Based on examining a subset of the physical models, their necks were approximately 17% larger in diameter than the necks originally designed in corresponding computational models. Using the same inflow conditions for CFD and PIV would thus lead to higher intra-aneurysmal velocities in the wider-neck physical models. Furthermore, PIV data were obtained from planes in the middle, higher flow region of the aneurysmal dome. CFD data, on the other hand, were computed over the entire aneurysmal domain that included lower flow regions toward the outskirts of the aneurysmal dome. The CFD results were reported for the entire aneurysmal domain in order to provide the most complete representation of aneurysmal hemodynamics. However, upon comparing the CFD and PIV data corresponding to the same fluid domains (as dictated by the span of the PIV data), the average discrepancies in aneurysmal V_{RMS} were (22.87%, 25.18%). We expect that these smaller magnitude discrepancies, which are also on the order of those observed for the anatomical cases, i.e., (17.86%, 26.41%), resulted from the aforementioned differences between the physical and computational geometries.

4.4.3 Comparisons Among Idealized and Anatomical Findings

To understand how the findings from idealized templates could potentially be translated to a more clinically relevant scenario, the two ABTA models were investigated. The simulated intra-aneurysmal flow patterns, represented in Figure 4.12, were qualitatively similar between the anatomical geometries and their idealized counterparts. There were magnitude differences between the anatomical and idealized hemodynamic responses (aneurysmal V_{RMS} and WSS values were 2.62 and 6.54 times greater on average in the anatomical cases), but such differences were expected given the dome size differences between the anatomical and idealized model sets. Further, as quantified earlier and illustrated in Figure 4.11 hemodynamic changes observed between the ABTA models and between their idealized counterparts were consistent. Specifically, simulated aneurysmal V_{RMS} and WSS values varied in the same directions between ABTA-1 and ABTA-2 and between IBTA-4 and IBTA-6, without exception, regardless of flow rate or type. This similarity in findings from the idealized and the anatomical aneurysm models indicates that characterizing the hemodynamic effects of aneurysmal geometry using templates has potential for utility in cerebral aneurysm evaluation. Comparable approaches have demonstrated success in applying template-based methods to characterize hemodynamics in even more complex cardiovascular geometries such as the Fontan connection [100].

4.4.4 Limitations

This study is subject to several limitations. First, a rigid wall assumption was used in the simulations and experiments. While using compliant models could be beneficial, previous studies have shown that the main factor driving aneurysmal hemodynamics is vessel

geometry and that vessel compliance is secondary (or even tertiary) [44], [90]. Second, the fluid mesh did not include near-wall refinement. Although near-wall mesh refinement would improve simulated WSS accuracy, given the very large WSS changes among different cases as reported in Table 1 (i.e., up to 473% and (91.42%, 72.67%) in magnitude on average), it is very unlikely that including near-wall refinement would affect any of the conclusions of this study. Further, WSS was considered in the mesh refinement study. Other assumptions of the study included Newtonian blood flow and equal zero-pressure boundary conditions at the outlets. Although the outlet boundary conditions used in simulations were not physiologic in an absolute sense, assuming equal pressures at the outlets is reasonable given the typically similar distal resistances in the cerebrovascular circulation [101]. To ensure that simplifying the absolute pressure values did not affect flow splits at the outlets considerably, an additional BTA simulation was run at more physiologic outlet pressure values, and the resulting flow splits varied from the simplified case by less than 1%. It is well known that more advanced outlet boundary conditions such as a three-element Windkessel (RCR) model can improve simulation accuracy, and do become more important when only small portions of the cerebrovascular system are included in the simulated fluid domain (as in this study). However, such boundary conditions are most important for deformable wall simulations and in cardiovascular regions where, unlike the cerebrovasculature, compliance is highly prevalent [87].

CHAPTER 5

EFFECTS OF GEOMETRIC VARIATIONS ON IDEALIZED SIDEWALL

ANEURYSM HEMODYNAMICS

5.1 Introduction

Aneurysmal geometry has already been established as an important predictor of aneurysm rupture [3]–[5], [102], and is considered in current clinical practice during cerebral aneurysm evaluation. However, a clear demarcation between different aneurysm types (e.g., bifurcation or sidewall aneurysm) was not considered in those studies. The impact of aneurysm type on hemodynamics was investigated in a CFD study by Hassan et al., where flow patterns in saccular aneurysms with different parent vessel configurations were compared [6]. The results demonstrated the importance of parent and outlet vessel geometries towards modifying aneurysmal hemodynamics. For example, the impact of the parent vessel on hemodynamics was more prominent in a sidewall aneurysm than in a bifurcation aneurysm [6]. Further studies on sidewall aneurysm hemodynamics have verified the importance of aneurysmal inflow angle (IA), and its possible implications towards cerebral aneurysm growth and rupture [35], [46].

In this chapter, the effects of geometric variations on idealized sidewall aneurysm (ISA) hemodynamics are quantified in order to attribute specific hemodynamic features to geometric parameters that are routinely quantified in clinical practice. The ISA templates were modeled after a saccular middle cerebral artery (MCA) sidewall aneurysm. A 2-level full factorial design of three geometric factors (i.e., dome size (DS),

dome-to-neck ratio (DNR), and IA) was used to create the sidewall aneurysm templates, and the hemodynamic responses were quantified using computational fluid dynamics (CFD) in terms of aneurysmal and neck-plane root-mean-square velocity magnitude (V_{RMS}), distal aneurysmal wall shear stress (WSS), and cross-neck flow (CNF). Methods and results specific to the ISA templates, including a comparison to the IBTA templates are discussed in this chapter.

5.2 Methods

5.2.1 Study Design

The effects of three geometric factors on ISA hemodynamics were investigated. Toward that end, low and high levels of DS, DNR and IA were chosen to generate a 2^3 full factorial design. Schematic representations of the geometric factors, including values used, are illustrated Figure 5.1. The corners of the cube in Figure 5.2 represent unique combinations of the three geometric factors (model numbers). For example, **5(6,3:2,90)** corresponds to the fifth ISA template (**ISA-5**) constructed with a **6** mm DS, **3:2** DNR and **90°** IA. The edges of the cube are color-coded to represent changes in a single geometric factor (with the other two factors held constant), and the direction of the colored arrows represent an increase in factor value. The red edges correspond to an increase in DS from 4 to 6 mm along the direction of the red arrow. Similarly, the green and blue edges correspond to an increase in DNR (from 3:2 to 2:1) and IA (from 90° to 135°), respectively, along the direction of the arrows.

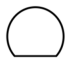



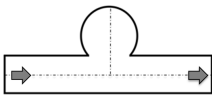
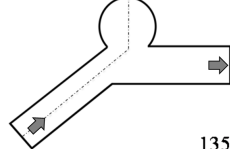
	Low	High
Dome Size	 4 mm	 6 mm
Dome-to-Neck Ratio	 3:2	 2:1
Inflow Angle (Sidewall Aneurysm)	 90°	 135°

Figure 5.1: Schematic representations of the different geometric factors (and values used) to generate idealized sidewall aneurysm templates for hemodynamic investigation. The inflow-outflow directions are marked by arrows in the drawing.

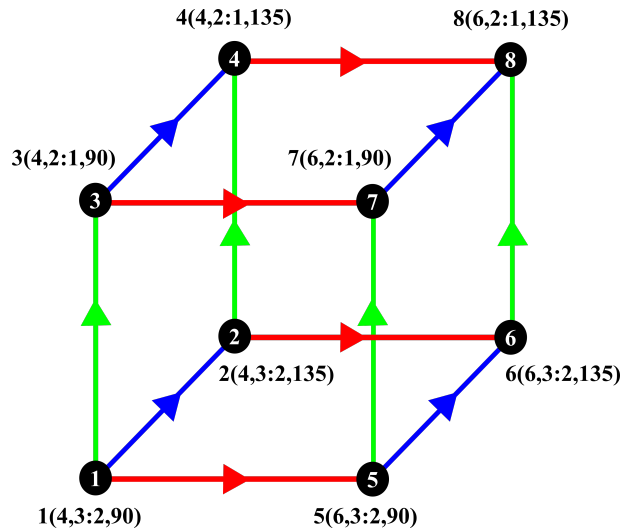


Figure 5.2: Cube representing a two-level full factorial design used to construct the idealized sidewall aneurysm templates based on three geometric factors: dome size, dome-to-neck ratio, and inflow angle. The red, green and blue edges correspond to an increase in DS, DNR, and IA, respectively, with the other two factors held constant, along the direction of the colored arrows.

5.2.2 Computational Model Construction

All eight ISA templates were constructed using SolidWorks, where the inlet and outlet was modeled as cylinders of diameter 4 mm, and the aneurysms were constructed as spheres. The DS, DNR, and IA values were imparted as per Figure 5.2. The final idealized computational templates are shown in Figure 5.3. The inlets and outlets were extruded to ensure fully developed boundary conditions at the aneurysm site, and to aid in CFD simulation convergence.

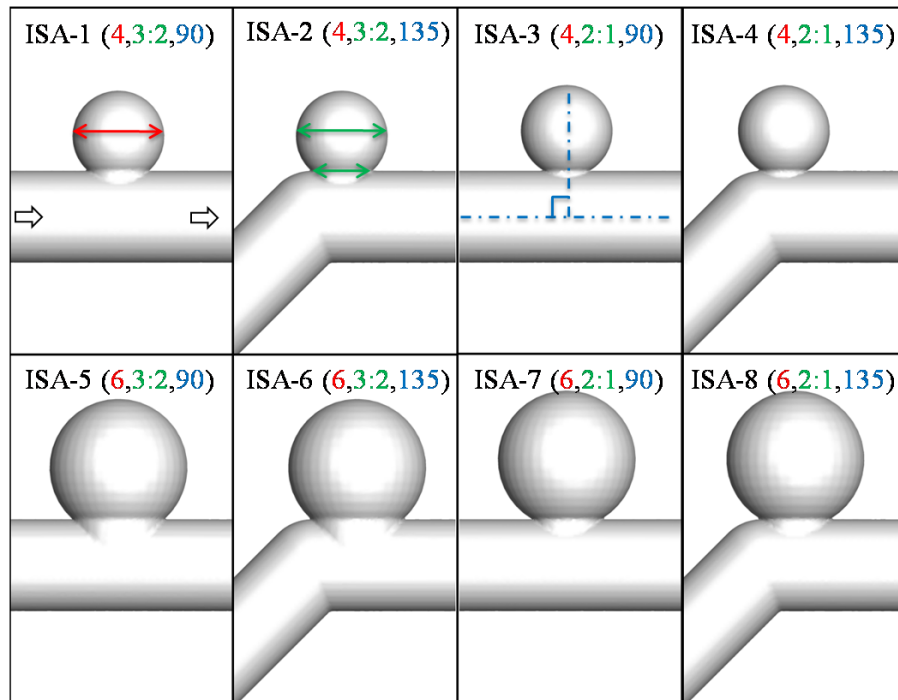


Figure 5.3: Idealized computational sidewall aneurysm templates. The numbers in red, green, and blue correspond to the dome size, dome-to-neck ratio and inflow angle. The direction of inflow and outflow is marked with the black arrow in template 1.

5.2.3 Computational Fluid Dynamics

The templates were prepared for CFD simulations in ANSYS ICEM 15. The blood volume was discretized into unstructured tetrahedral mesh elements using the Octree algorithm in ICEM. The Octree method of mesh generation has been described in Section 3.2.3. To ensure that the calculated hemodynamic responses did not vary with mesh sizes, a mesh independence study was performed on ISA-1 at a steady inflow rate of 3 mL/s by varying the specified maximum element size from 0.3 to 0.15 mm. The final mesh size (maximum element size = 0.17 mm) was deemed acceptable when the calculated responses (i.e., V_{RMS} , WSS, and CNF) varied by less than 4% between subsequent trials. The final meshes (for all eight templates) ranged between 7.48 and 7.75 million elements.

The meshed templates were next imported into ANSYS Fluent for CFD simulations. The fluid was assumed to be incompressible and Newtonian, with a density of 1060 kg/m^3 and viscosity of 3.71 cP. The models were assumed to be rigid with a no-slip condition imposed at the vessel wall. Steady inflow rates of 2, 3, and 4 mL/s were investigated, corresponding to Reynold's numbers of 247.39, 371.09, and 794.98, respectively. The flow rates were chosen from literature, and they span the ranges normal and diseased flow conditions in cerebral arteries [88]. Furthermore, they were the same flow rates as investigated in the idealized bifurcation aneurysm studies so as to facilitate direct comparisons of the effects of aneurysmal geometry on hemodynamics between the two aneurysm variants. To efficiently incorporate the effects of downstream vasculature

on ISA hemodynamics, resistance-based boundary condition was specified at the outflow according to the following equation:

$$P_{outlet} = R_p \times Q_{outflow}, \quad (5.1)$$

where P_{outlet} is the outlet pressure, R_p is the value for peripheral resistance due to the downstream vasculature, and $Q_{outflow}$ is the flow rate through the outlet. R_p was chosen from literature as $5.97 \times 10^9 \text{ Pa s m}^{-3}$ based on the downstream resistance value for a MCA [103]. The flow rate through the outlet was calculated using the *Murray's law* that is based on the principle of minimal work. The law describes a relationship between daughter vessel radii to that of the parent vessel according to the following equation:

$$r_p^3 = r_1^3 + r_2^3 + \dots + r_n^3, \quad (5.2)$$

where r_p is the parent vessel radius, and r_1 through r_n represents the daughter vessel radii. Based on the law, a functional relationship is believed to exist between the vessel radius and volumetric flow rate, flow velocity, velocity profile and wall shear stress [104]. For a single inflow-single outflow vessel, the rate of inflow equals to the rate of outflow (based on the law of conservation of mass). Therefore, the outlet pressures specified for the simulations calculated according to equation 5.1 for inflow rates of 2, 3, and 4 mL/s were 11940, 17910, and 23880 Pa, respectively. A second-order discretization scheme was used for momentum discretization, and the pressure-velocity coupling was specified according to the SIMPLE algorithm.

5.2.4 Computational Data Analysis

The CFD results were analyzed using Tecplot 360 to calculate hemodynamic responses within the aneurysm and at the neck-plane. Specifically, V_{RMS} and WSS were calculated within the aneurysmal domain, and V_{RMS} and CNF were calculated at the neck-plane. The effects of individual geometric factor changes on hemodynamics were investigated by comparing hemodynamic responses obtained by changing a single geometric factor (keeping the other two factors constant). The CFD results were also analyzed using a statistical analysis software, JMP Pro, to determine the percentage contribution of individual geometric factors, and factor interactions, on aneurysmal and neck plane hemodynamics. Sum of squares (SS) for each geometric factor factors, and interactions, were calculated and the percentage contribution was calculated as

$$\%Contribution = \frac{SS_{individual}}{SS_{total}}, \quad (5.3)$$

This approach was similar to the methodology utilized by [97] to identify and rank the primary contributors to the integrated drag of the NASA crew exploration vehicle ascent trajectory. Finally, the effects of geometric variations on the ISA templates were compared to the effects of geometric variations on the IBTA templates discussed in Chapter 5.

5.3 Results

5.3.1 Idealized Aneurysm Models (Templates)

The effects of geometry on ISA hemodynamics were investigated by calculating the changes in hemodynamic responses while changing one geometric factor and keeping the other two factors constant. The results are presented in Table 5.1. Increasing DS from 4 mm to 6 mm, and IA from 90° to 135° increased all calculated hemodynamic responses. On average (across all flow rates), increasing DS increased WSS by 77.59%, aneurysmal V_{RMS} by 62.15%, neck-plane V_{RMS} by 57.67%, and CNF by 233%. Increasing IA increased WSS by 856.99%, aneurysmal V_{RMS} by 291.83%, neck-plane V_{RMS} by 154.67%, and CNF by 364.40%. On the other hand, increasing DNR from 3:2 to 2:1 decreased all calculated responses, changing WSS by 66.21%, aneurysmal V_{RMS} by 62.15%, neck-plane V_{RMS} by 21.89%, and CNF by 55.23%. As observed from the table, increasing IA had the most prominent effect on changing aneurysmal and neck-plane hemodynamics. The effects of IA on intra-aneurysmal flow is also shown in Figure 5.4. Examples of the effects of the individual geometric factors on aneurysmal V_{RMS} are illustrated in Figure 5.5 (a)-(c).

Table 5.1: Percentage changes in hemodynamic responses calculated by changing one geometric factor, keeping the other two factors constant, for all investigated flow rates.

Changed factors	Constant factors (factor 1;factor 2)	Flow rate (mL/s)	Aneurysmal WSS (%)	Aneurysmal V_{RMS} (%)	Neck-plane V_{RMS} (%)	Cross-neck flow (%)
Dome size (4 to 6 mm)	(3:2;90°)	2	10.19	26.68	12.43	260.40
		3	12.05	20.79	7.40	223.50
		4	-4.58	13.15	3.64	201.57
	(3:2;135°)	2	214.47	134.02	110.28	404.03
		3	189.34	113.58	106.35	299.41
		4	141.84	93.12	99.33	244.86
	(2:1;90°)	2	8.16	35.78	21.47	221.50
		3	8.48	28.74	15.35	199.23
		4	9.37	24.19	11.25	186.55
	(2:1;135°)	2	118.24	108.93	113.09	239.95
		3	127.48	82.26	102.32	170.35
		4	96.00	64.54	89.11	144.70
Dome-to-neck ratio (3:2 to 2:1 mm)	(4 mm;90°)	2	-57.26	-38.13	-10.79	-53.89
		3	-57.17	-37.26	-8.14	-52.97
		4	-56.99	-36.53	-6.38	-52.29
	(4 mm;135°)	2	-74.86	-58.07	-41.34	-53.35
		3	-74.37	-53.31	-38.41	-45.83
		4	-69.19	-49.11	-34.83	-42.99
	(6 mm;90°)	2	-58.04	-33.69	-3.62	-58.87
		3	-58.53	-33.14	-1.35	-56.50
		4	-50.71	-30.34	0.50	-54.67
	(6 mm;135°)	2	-82.55	-62.56	-40.55	-68.53
		3	-79.85	-60.15	-39.62	-63.33
		4	-75.03	-56.65	-38.17	-59.55
Inflow Angle (90° to 135° mm)	(4 mm;3:2)	2	154.04	120.38	69.12	220.21
		3	617.73	331.96	206.80	412.46
		4	1091.79	354.91	145.34	407.49
	(4 mm;2:1)	2	49.41	49.38	11.22	223.99
		3	269.69	147.08	38.67	375.12
		4	753.74	264.74	70.77	506.38
	(6 mm;3:2)	2	625.03	307.14	216.32	347.83
		3	1495.27	486.96	297.39	409.29
		4	2920.45	676.47	371.84	480.34
	(6 mm;2:1)	2	201.48	129.86	95.10	242.59
		3	675.21	249.80	143.23	329.27
		4	1429.99	383.26	190.28	417.82

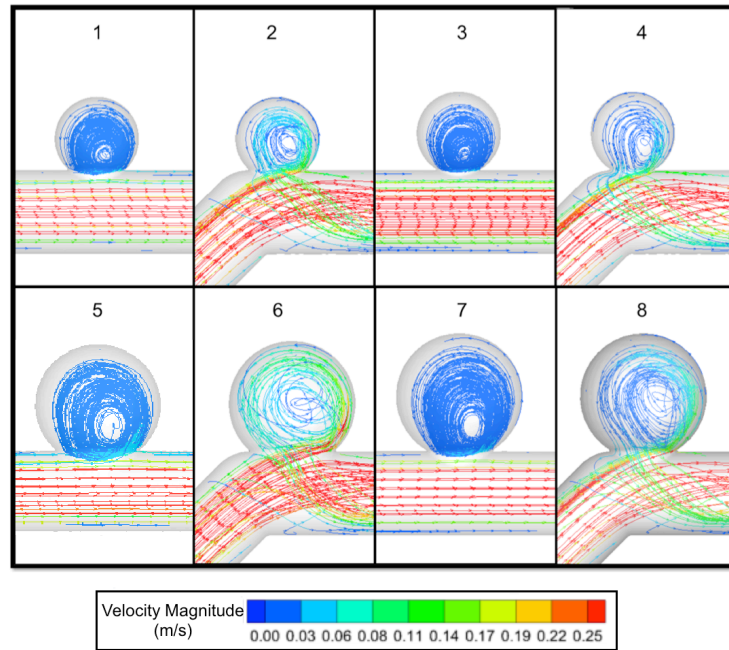


Figure 5.4: Intra-aneurysmal flow patterns in the idealized sidewall aneurysm templates represented as streamtraces color-coded by velocity magnitude, for an inflow rate of 3 mL/s.

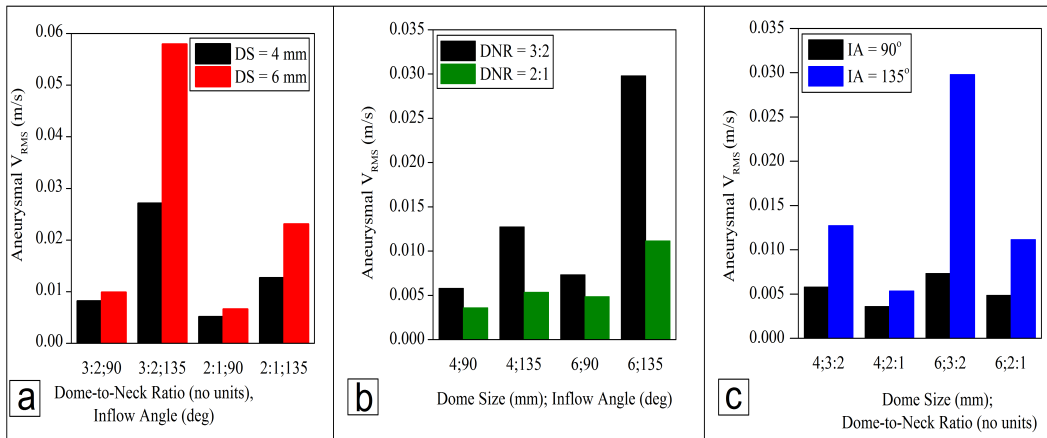


Figure 5.5: Effects of change in (a) dome size (keeping dome-to-neck ratio and inflow angle constant within grouped bars), (b) dome-to-neck ratio (keeping dome size and inflow angle constant within grouped bars), and (c) inflow angle (keeping dome size and dome-to-neck ratio constant within grouped bars) for a 3 mL/s inflow.

Statistical analysis of the geometric main factors revealed that all three geometric factors played prominent roles in modifying aneurysmal and neck-plane hemodynamics, as illustrated by Figure 5.6. IA made the greatest contribution towards modifying all calculated hemodynamic responses (i.e., WSS, aneurysmal and neck-plane V_{RMS} , and CNF). DS and DNR made the second greatest contributions towards modifying neck-plane and aneurysmal hemodynamics, respectively. It is noteworthy that factor interactions, particularly IA with DS or DNR, also contributed to modifying all calculated ISA hemodynamics.

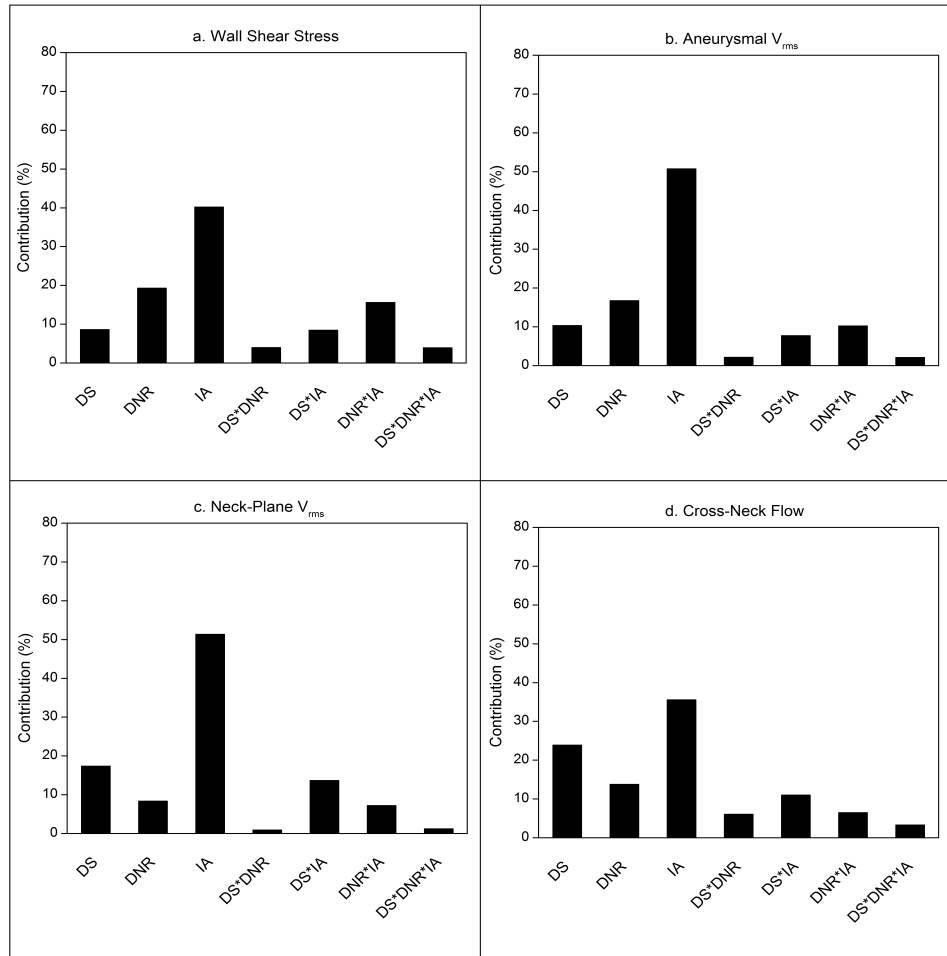


Figure 5.6: Percentage contribution of dome size, dome-to-neck ratio, and inflow angle to effects on idealized sidewall aneurysm hemodynamics.

5.3.2 Comparisons with Idealized Bifurcation Aneurysm Templates

The effects of geometric factors on ISA hemodynamics were also compared with the IBTA results presented in Chapter 4 to understand the impact of geometric variations based on aneurysm type. Comparison of Figures 4.8 and 5.6 clearly depict differences in the impact of DS, DNR, and IA on IBTA and ISA hemodynamics. The percentage

contributions of individual geometric factors and their interactions in IBTA and ISA hemodynamics under steady inflow conditions are presented in Table 5.2.

Table 5.2: Percentage contributions of the investigated geometric factors, and their interactions, on aneurysmal and neck-plane hemodynamic responses in idealized bifurcation and sidewall aneurysm templates. The first, second and third largest contribution is highlighted in orange, purple and grey, respectively.

Hemodynamic	Factors	IBTA Templates: %	ISA Templates: %
Aneurysmal WSS	DS	8.28	8.62
	DNR	46.21	19.30
	IA	17.91	40.16
	DS*DNR	3.94	3.94
	DS*IA	11.93	8.44
	DNR*IA	9.07	9.07
	DS*DNR*IA	3.93	3.93
Aneurysmal V_{RMS}	DS	23.07	10.34
	DNR	71.94	16.72
	IA	0.05	50.72
	DS*DNR	0.06	2.14
	DS*IA	3.66	7.73
	DNR*IA	0.16	10.23
	DS*DNR*IA	1.05	2.11
Neck-plane V_{RMS}	DS	21.84	17.36
	DNR	53.37	8.36
	IA	12.72	51.34
	DS*DNR	6.23	0.88
	DS*IA	0.13	16.67
	DNR*IA	4.34	7.20
	DS*DNR*IA	2.70	1.18
Cross-neck flow	DS	43.94	23.86
	DNR	36.93	13.77
	IA	3.74	35.54
	DS*DNR	9.73	6.02
	DS*IA	0.39	11.01
	DNR*IA	3.81	6.49
	DS*DNR*IA	1.47	3.31

Aneurysmal DS and DNR had similar effects on IBTA and ISA hemodynamics, i.e., increase in DS increased calculated hemodynamic responses, and increase in DNR decreased calculated responses. In contrast, the parent vessel IA had drastically different effects on IBTA and ISA hemodynamics. While increasing IA in the IBTA templates increased only the neck-plane responses, all the ISA templates exhibited higher values of calculated hemodynamics for the higher IA. This may be due to the stark differences in inflow patterns between the two variants, as represented in Figure 5.7.

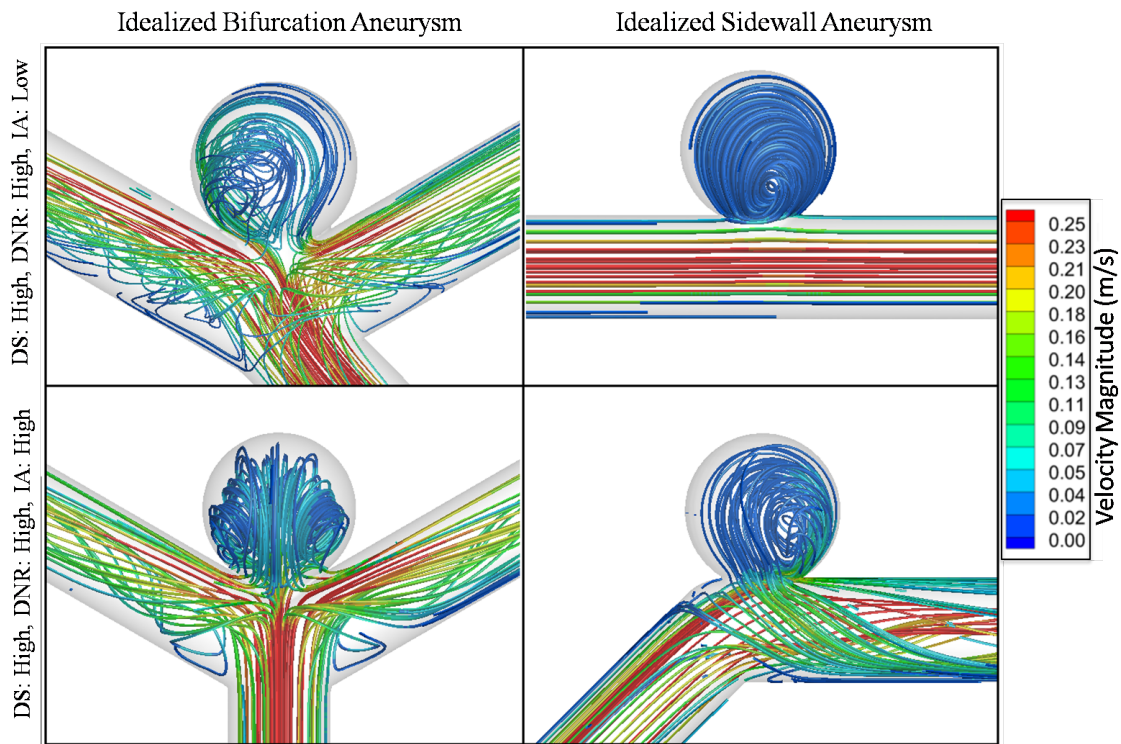


Figure 5.7: Comparison of intra-aneurysmal flow patterns in idealized (left) bifurcation and (right) sidewall aneurysm templates with (top) low and (bottom) high inflow angle.

5.4 Discussion

5.4.1 Effects of Geometric Main Factors on Hemodynamics

The importance of geometry in cerebral aneurysm progression and/or rupture and its role in modifying hemodynamics is well established [28], [46], [102], [105]. Extensive studies on the natural history of aneurysms have identified rupture risks based on important geometric and morphologic features, and aneurysm locations. However, those studies have failed to factor in the aneurysm type based on parent and daughter vessel configurations [3]–[5], [31]. This chapter investigated the effects of three clinically recognized geometric factors (i.e., DS, DNR, and IA) to effects on ISA hemodynamics using CFD simulations. Aneurysmal WSS, aneurysmal and neck-plane V_{RMS} , and CNF were the four hemodynamic responses evaluated. The effects of geometry on two different aneurysm types were also studied by comparing the hemodynamic responses calculated from ISA templates to the hemodynamic responses calculated from IBTA templates. Bridging the gap between aneurysm geometry and hemodynamics has the potential to play a valuable role in clinical decision-making during cerebral aneurysm evaluation.

Individually, all three geometric factors had an effect on aneurysmal and neck-plane hemodynamics. ISA templates with higher IA (i.e., the 135° templates) had elevated levels of aneurysmal compared to their 90° counterparts. On average, increase in IA increased WSS, aneurysmal V_{RMS} , neck-plane V_{RMS} and CNF by 856.99%, 291.83%, 154.67%, and 364.40%, respectively, across all flow rates. The elevated levels may be

due to distinct differences in flow patterns, as illustrated in Figure 5.4. These results agreed with previous findings where greater inflow angles were associated with elevated levels of hemodynamic responses that may promote aneurysmal growth and/or rupture [35], [46]. The impact of IA was confirmed by statistical examination of the contribution that the factor effected on modifying hemodynamics, where IA consistently had the highest contribution.

The other important geometric factor investigated was aneurysmal DS. Clinically, DS has been established as an independent predictor of aneurysm rupture where larger aneurysm size is associated with higher rupture risks [3]. The larger domed ISA templates had higher levels of WSS, CNF and V_{RMS} that can contribute to aneurysmal growth and/or rupture [35], [99]. Main factor analysis revealed that DS made the second highest contribution (over 17%) to effects on neck-plane hemodynamics. Aneurysmal DNR is an important geometric factor investigated particularly in the context of cerebral aneurysm treatment. Aneurysms with lower DNR (i.e., DNR of 3:2) were associated with higher levels of calculated hemodynamic responses which can lead to further aneurysm growth and eventual rupture, as discussed earlier. DNR made over 15% contributions towards modifying aneurysmal hemodynamic responses.

Second and third level factor interactions also made contributions to effects on cerebral aneurysm hemodynamics, the most prominent of which were the interaction of IA with DS or DNR. The presence of factor interactions show that although individual geometric factors may play an important role in modifying flow, multiple geometric factors can together impact hemodynamics should therefore be considered during pre-treatment cerebral aneurysm evaluation.

5.4.2 Comparisons Among Idealized Bifurcation and Sidewall Aneurysm Templates

Comparisons with idealized bifurcation aneurysm templates revealed how that the same geometric factors could have very different effects on flow depending on the aneurysm type. For example, while IA only had a major effect on aneurysmal WSS in the IBTA templates, the impact of IA on ISA hemodynamics was much more pronounced (over 35% contribution in the ISA templates versus a maximum of 17.91% in the IBTA templates). The results obtained from this study further demonstrated the necessity of a hemodynamic basis for cerebral aneurysm evaluation, in addition to the already popular geometry-based evaluation criteria.

5.4.3 Limitations

This section highlights some limitations of the study. One of the main limitations of this study was the rigid wall assumption. While the use of compliant models would be more beneficial, aneurysm geometry has been established as the primary driver of hemodynamics [90], [91]. In general, cerebral arteries are much stiffer compared to extracranial arteries [106], [107]. Löw et al. estimated the maximum wall distensibility of a saccular aneurysm to be 6% [108]. Another limitation of this study was the investigation of hemodynamics under steady flow conditions. However, previous studies (including the data presented in Chapters 4 and 6) have shown that steady flow simulations provide a strong indication of fundamental trends that occur under pulsatile

flow conditions [20], [109], [110]. This study is also limited in that blood flow was assumed to be Newtonian, while blood is actually a non-Newtonian fluid. Nevertheless, previous studies comparing the effects of non-Newtonian versus Newtonian fluid models in cerebral arteries have demonstrated that the global flow characteristics do not vary drastically between the two models [64], [82].

CHAPTER 6

HEMODYNAMIC CHARACTERIZATION OF CEREBRAL ANEURYSM

TEMPLATES TREATED WITH EMBOLIC COILS

6.1 Introduction

Endovascular treatment for cerebral aneurysm repair have gained popularity over traditional surgery due to their minimally invasive nature, shorter recovery time, and reduced hospital costs [111]. Embolic coiling is one of the most effective treatments for cerebral aneurysms, largely due to the hemodynamic modifications that the treatment effects in the aneurysm environment. During this process, a series of flexible coils is deployed into the aneurysm dome to promote thrombosis. Over time, vascular remodeling at the neck then leads to complete isolation of the aneurysm from circulation. Although cerebral aneurysms treated with embolic coils have been associated with lower mortality rates than those treated with surgical clipping [111], not all aneurysms can be treated with coiling. Geometric features of the aneurysm, such as DNR and neck size (NS), are key determinants in selecting patients for treatment with embolic coils. Studies have shown that aneurysms with DNR above 1.6 and NS below 5 mm are suitable for treatment with embolic coils without the need for any adjunctive techniques [18], [19]. Although geometric patient selecting criteria for coiling has been clearly established, post-treatment hemodynamics may also be taken into consideration because unfavorable hemodynamic changes can promote aneurysmal recanalization.

Hemodynamics are known to influence cerebral aneurysm growth and rupture, and are related to aneurysmal geometry [35], [43], [47]. Geometry is also known to affect post-treatment outcomes. For example, aneurysms with DS greater than 9 mm were observed to have higher recurrence rates (50% versus 21%) than aneurysms between 3 and 9 mm [36]. Another factor that influences treatment outcome is coil packing density (PD), a treatment factor defined as the percentage of the aneurysmal volume occupied by coils. PDs between 20 and 25% were observed to prevent unfavorable post-treatment outcomes [17]. It is therefore critical to consider the effects of geometric and treatment factors in working towards optimal treatments in the context of aneurysmal hemodynamics.

This chapter relates two geometric factors that characterize cerebral aneurysms and one factor that describes treatment to three clinically relevant hemodynamic responses. Narrow-neck idealized BTAs and SAs, with 2:1 DNR were chosen from the full factorial designs explained in Chapters 4 and 5.

6.2 Methods

6.2.1 Study Design

IBTA and ISA templates, marked with orange bubbles in Figure 6.1 (a), were chosen from the 2^3 level full factorial designs for this study. Only the templates with 2:1 DNR were chosen since treatment with embolic coils is the preferred method of treating narrow-neck aneurysms. This facilitated the creation of a 2^2 factorial design, as shown in

Figure 6.1 (b). The colored edges of the square represent increase in a single geometric factor, with the other factor held constant, indicated by the direction of the colored arrows. Flows within the IBTA and ISA templates were computed in-silico using CFD. Flows within two of the four IBTA templates were also measured in-vitro using PIV. As in the case of the pre-treated IBTA and ISA templates, flow rates of 2, 3 and 4 mL/s were explored.

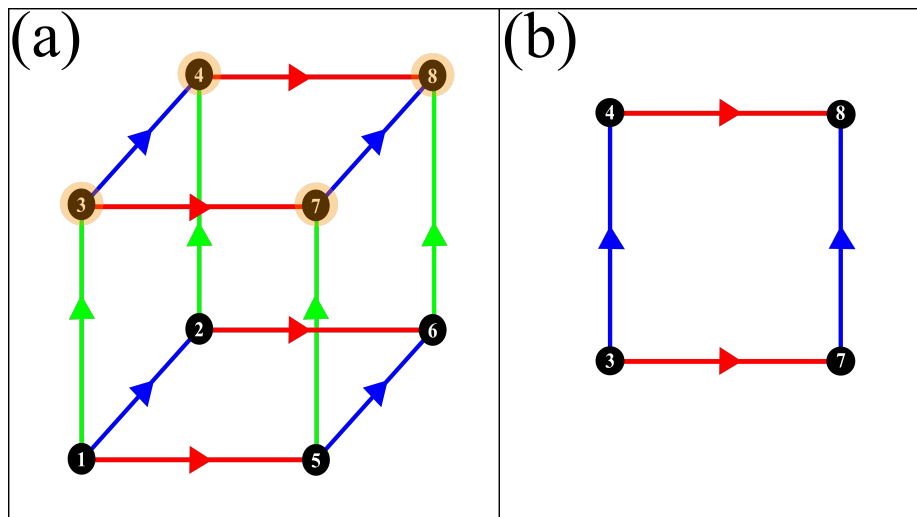


Figure 6.1: Representation of the geometric templates used for coiling (a) chosen from the 2^3 factorial design (marked with orange bubbles), and (b) as a 2^2 factorial design.

6.2.2 Computational Methods

6.2.2.1 Computational Model Construction

The process of constructing the computational IBTA and ISA templates are detailed in Sections 4.2.2.1 and 5.2.2, respectively. IBTA- and ISA-3, 4, 7 and 8 were chosen for investigation with embolic coils. The inlets and outlets of all computational templates were extruded to ensure fully developed flow conditions at the aneurysm, and to aid in simulation convergence.

6.2.2.2 Virtual Device Deployment

FE modeling techniques were employed to virtually treat all four aneurysm templates with embolic coils using Abaqus (Simulia, Providence, RI). The coils were modeled based on Orbit Galaxy Fill detachable coils (Johnson & Johnson, New Brunswick, NJ). Coil loop diameters of 4mm and 2mm were chosen for the framing and filler coils, respectively. The coil sizes used for virtual deployment for the small and large DS are listed in Table 6.1.

Table 6.1: Coil sizes used for virtual deployment of embolic coils in the IBTA and ISA aneurysms.

Dome Size (mm)	Deployment 1 Loop diameter (mm) x length (cm)	Deployment 2 Loop diameter (mm) x length (cm)	Deployment 3 Loop diameter (mm) x length (cm)	Deployment 4 Loop diameter (mm) x length (cm)
4	4x6.5	2x2.5	2x2.5	2x2.5
6	4x15	4x15	2x10	2x5

Each coil was modeled as serially linked 3D Timoshenko beam elements. The larger and smaller coils had Young’s moduli of 6.5 GPa and 5.5 GPa, and material densities of 21.45 g/cm³ and 19 g/cm³, respectively. A Poisson ratio of 0.39 was also specified, approximating the coils as solid beams composed primarily of platinum. The coil deployment process in ABAQUS/Explicit consisted of (a) virtually placing the coil within a microcatheter and positioning the microcatheter within the aneurysm dome, (b) advancing the coil into the dome using displacement boundary conditions at the proximal node of the coil (to mimic the movement of a clinical coil pusher wire), and (c) releasing the coil to complete each deployment. Coil-to-coil, coil-to-microcatheter, coil-to-aneurysm, and intra-coil interactions were specified using the “general contact” algorithm in ABAQUS/Explicit. Further details on the coil modeling and deployment processes have been previously reported by Babiker et al. [79]. The 4 mm and 6 mm models underwent four deployment processes to achieve PD configurations of 26% and 27%, respectively. The final coil configurations for the small and large DS are shown in Figure 6.2, and the computational IBTA and ISA templates after virtual treatment with embolic coils are shown in Figure 6.3. PD was calculated as

$$PD = \frac{Volume_{coils}}{Volume_{aneurysm}} \times 100\%. \quad (6.1)$$

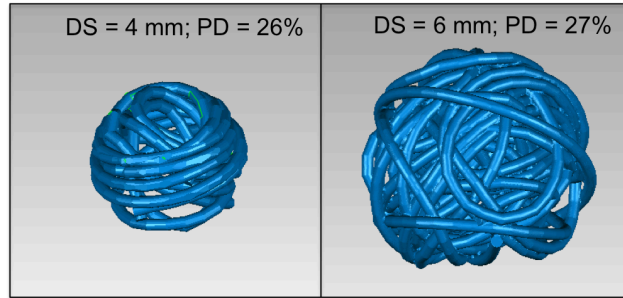


Figure 6.2: Deployed coil configuration for the cerebral aneurysm templates with (left) small DS, and (right) large DS.

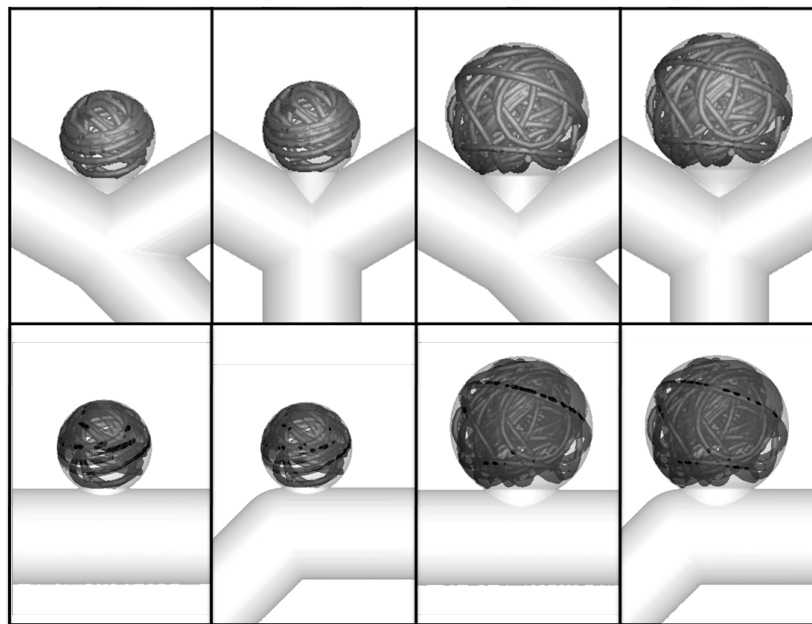


Figure 6.3: (top) IBTA and (bottom) ISA templates virtually treated with embolic coils.

6.2.2.3 Computational Fluid Dynamics

ANSYS ICEM 12.1 (Ansys, Inc., Canonsburg, PA) was used to prepare the computational templates for CFD simulations where the fluid and coil domains were

discretized into mesh elements using the Octree approach. A mesh density function was specified around the aneurysm and coil volumes (in the treated templates) to accurately capture fluid dynamic variations around the device. The maximum element sizes for the untreated and treated IBTA templates were 0.25 mm and 0.2 mm, respectively, and the final untreated and treated IBTA meshes ranged between 6.1 and 7.1×10^6 and 18.5 and 24.3×10^6 elements, respectively. The maximum element sizes for the untreated and treated ISA templates were 0.17 mm, and the final untreated and treated ISA meshes ranged between 7.5 and 7.8×10^6 and 11.4 and 16×10^6 million elements, respectively. The maximum element size for the FE embolic coils were specified as 0.04 mm for all treated templates.

The meshed geometries were then imported into ANSYS FLUENT (Ansys, Inc., Canonsburg, PA) for CFD simulations. Blood was modeled as an incompressible and Newtonian fluid. The coil surface and vessel walls were assumed to be rigid, and a no-slip boundary condition was imposed at the walls. The SIMPLE algorithm was used for pressure–velocity coupling, and a second-order discretization scheme was used for momentum.

IBTA Simulations

Blood was modeled with a density of 1500 kg/m^3 and viscosity of 3.86 cP to match the blood analog solution used for PIV experiments. Steady and pulsatile inflow rates of 2, 3 and 4 mL/s were explored, and zero-pressure boundary conditions were specified at the outlets. Modified vertebral artery flow waveforms were prescribed at the inlet for the

pulsatile flow simulations [89].

ISA Simulations

In the case of the ISA simulations, blood was modeled with density and viscosity of 1060 kg/m³ and 3.71 cP, respectively, to match the properties of blood. Flow rates of 2, 3, and 4 mL/s were explored under steady inflow conditions, and a resistance boundary condition was specified at the outlet according to equation 5.1. The outlet pressure values calculated from equation 5.1 for inflow rates of 2, 3 and 4 mL/s were 11940, 17910 and 23880 Pa, respectively.

6.2.3 Experimental Methods

6.2.3.1 Physical Model Construction

Flows within two of the four computational IBTA templates (IBTA-3 and IBTA-8) were translated into lost-core urethane models for experimental flow measurement using PIV. The two models allowed for examination of all different factors considered. The process for constructing the urethane has been explained in detail in Section 3.3.1. The overall manufacturing process involved (1) translating the computational models to wax models, (2) re-casting the wax models into metal models, (3) encapsulating the metal core within optically clear urethane, (4) heating the urethane block to melt the metal core, and (5) remove metal remnants using acid wash and polishing the urethane blocks to enhance

optical clarity.

6.2.3.2 Device Deployment

The physical aneurysm models were embolized with TruFill DCS Orbit detachable coils (Codman Neurovascular, Johnson & Johnson, Brunswick, NJ). A pusher wire was used to advance the coils into the aneurysm after which a clinical coil detachment syringe (TruFill DCS Syringe, Codman, Johnson & Johnson, New Brunswick, NJ) was used to detach the coils from the delivery system. Series of coils were deployed within both aneurysms, with larger coils framing the aneurysmal sac and smaller coils filling up the space within to achieve PDs that matched the in-silico deployments approximately. The final deployed coil configuration in IBTA-3 and IBTA-8 are shown in Figure 6.4.

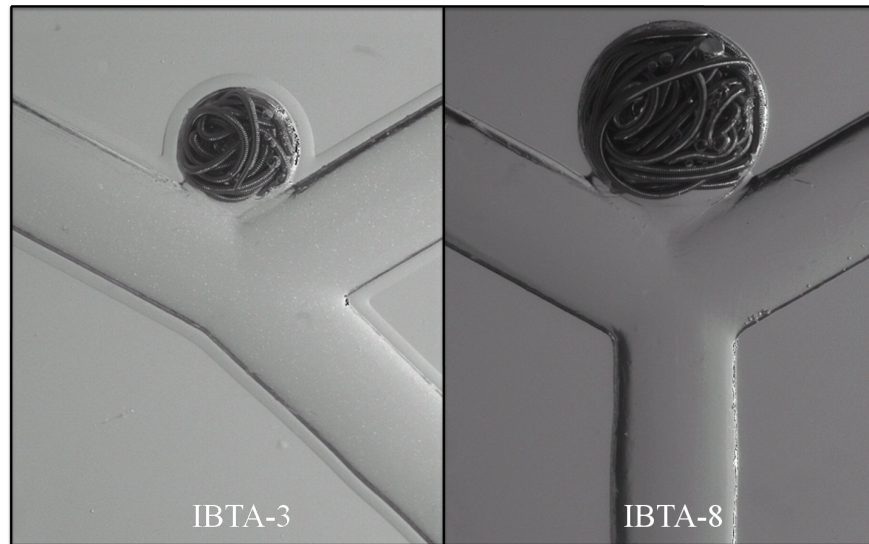


Figure 6.4: Deployed embolic coils in the physical urethane models.

6.2.3.3 Particle Image Velocimetry

The urethane models, before and after treatment with embolic coils, were connected to a flow loop to measure hemodynamic responses at the aneurysm neck. The flow loop and PIV process has been described in Sections 3.3.2 - 3.3.5. Volumetric flow data were acquired over five planes within the fluid volume, each plane separated by 0.5 mm.

6.2.4 Analysis

6.2.4.1 Computational Data Analysis

Tecplot 360 was used to calculate WSS (in the distal half of aneurysmal dome), V_{RMS} (over the entire aneurysmal dome, and the neck-plane), and cross-neck flow in IBTA and ISA templates, before and after treatment with embolic coils. Hemodynamic responses obtained under steady and pulsatile conditions in the IBTA templates were also compared using Pearson correlation. The calculated steady responses were then statistically analyzed using JMP Pro (JMP, SAS Institute, Inc., Cary, NC) to determine the contributions of DS, IA, and PD toward modifying IBTA and ISA hemodynamics as a 2x2x2 factorial design. The two levels of PDs corresponded to the pretreated (PD of 0%) and treated (PDs of 26% and 27% for DS of 4mm and 6 mm, respectively) conditions. Sum of squares (SS) values for each factor (and factor interactions) were calculated using regression analysis, and the percentage contribution of each factor was then calculated as

$$\%Contribution = \frac{SS_{factor}}{SS_{total}} \times 100\%. \quad (6.2)$$

This method is similar to the analysis technique presented by Rhew and Parker [97]. Following the 2x2x2 factorial analysis, two 2-factor two-level analyses were conducted to consider the effects of geometry on untreated and treated aneurysm hemodynamics separately. SS values were calculated as previously described to determine the percentage contributions of each of the geometric factors, and their interactions, toward effects on hemodynamics.

6.2.4.2 Experimental Data Analysis

An in-house MATLAB code (MathWorks, Inc., Natick, MA) was used to analyze the velocity data measured using PIV. CNF at the neck-plane was calculated and compared to the CNF values obtained from corresponding computational IBTA templates using Pearson correlation. Only the neck-plane vectors could be analyzed in experimental cases, because the aneurysmal sac was occluded with coils in the treated physical models.

6.3 Results

6.3.1 Idealized Bifurcation Aneurysm Results

The CFD-based hemodynamic responses for all four IBTA templates, before and after treatment with embolic coils, and across all investigated steady flow rates, are reported in

Table 6.2. As expected, packing the aneurysm with embolic coils (increasing the PD from 0% to over 25%) decreased all calculated responses, except neck-plane V_{RMS} in IBTA-8 . Figure 6.5 illustrates the effects of increasing PD on aneurysmal WSS in the IBTA templates at a 3 ml/s steady inflow rate. Increasing DS from 4mm to 6mm (keeping IA constant) increased WSS, V_{RMS} , and CNF in the untreated and treated templates. For example, the effects of increasing DS on CNF are illustrated in Figure 6.6 (black to red boxes). IA, on the other hand, had lesser effects on hemodynamics.

Table 6.2: Hemodynamic responses calculated from CFD for all four IBTA templates and across all investigated steady and pulsatile (in parenthesis) flow rates before and after treatment with embolic coils.

Model	Flow Rate (mL/s)	Untreated 0% PD				Treated PD 26% (DS: 4mm) PD 27% (DS: 6 mm)			
		Aneurysm		Neck-plane		Aneurysm		Neck-plane	
		WSS Pa	V_{RMS} m/s	V_{RMS} m/s	CNF mL/s	WSS Pa	V_{RMS} m/s	V_{RMS} m/s	CNF mL/s
IBTA – 3 (4 mm, 135°)	2	0.031 (0.077)	0.008 (0.010)	0.023 (0.028)	0.085 (0.101)	0.001 (0.001)	0.003 (0.003)	0.020 (0.018)	0.033 (0.032)
	3	0.116 (0.135)	0.017 (0.019)	0.040 (0.047)	0.153 (0.136)	0.003 (0.003)	0.008 (0.009)	0.037 (0.038)	0.070 (0.073)
	4	0.265 (0.304)	0.027 (0.030)	0.057 (0.067)	0.219 (0.232)	0.007 (0.029)	0.015 (0.015)	0.054 (0.053)	0.108 (0.107)
IBTA – 4 (4 mm, 180°)	2	0.016 (0.019)	0.008 (0.012)	0.034 (0.035)	0.111 (0.100)	0.001 (0.001)	0.006 (0.006)	0.033 (0.030)	0.078 (0.030)
	3	0.089 (0.147)	0.021 (0.026)	0.063 (0.070)	0.207 (0.176)	0.004 (0.002)	0.012 (0.011)	0.058 (0.054)	0.145 (0.054)
	4	0.264 (0.260)	0.036 (0.038)	0.090 (0.084)	0.300 (0.274)	0.006 (0.006)	0.018 (0.016)	0.083 (0.074)	0.206 (0.074)
IBTA – 7 (6 mm, 135°)	2	0.175 (0.187)	0.021 (0.022)	0.042 (0.039)	0.337 (0.321)	0.005 (0.009)	0.006 (0.007)	0.032 (0.035)	0.128 (0.035)
	3	0.462 (0.484)	0.038 (0.039)	0.067 (0.063)	0.535 (0.416)	0.017 (0.018)	0.013 (0.014)	0.059 (0.067)	0.255 (0.067)
	4	0.858 (0.883)	0.056 (0.056)	0.093 (0.087)	0.730 (0.646)	0.036 (0.035)	0.020 (0.023)	0.086 (0.102)	0.385 (0.012)
IBTA – 8 (6 mm, 180°)	2	0.062 (0.050)	0.017 (0.016)	0.040 (0.043)	0.283 (0.250)	0.004 (0.006)	0.006 (0.005)	0.036 (0.035)	0.132 (0.035)
	3	0.277 (0.222)	0.035 (0.032)	0.067 (0.071)	0.477 (0.339)	0.013 (0.011)	0.014 (0.012)	0.071 (0.066)	0.292 (0.066)
	4	0.644 (0.486)	0.055 (0.048)	0.094 (0.097)	0.673 (0.504)	0.029 (0.025)	0.023 (0.020)	0.109 (0.133)	0.466 (0.133)

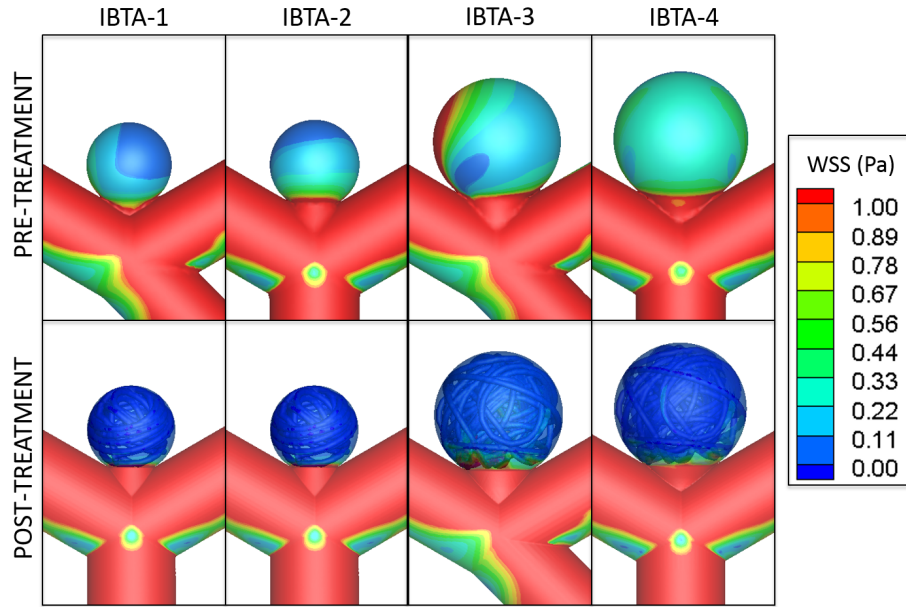


Figure 6.5: Wall shear stress distribution in the idealized basilar tip aneurysm templates pre- and post-treatment at a 3 mL/s steady inflow rate.

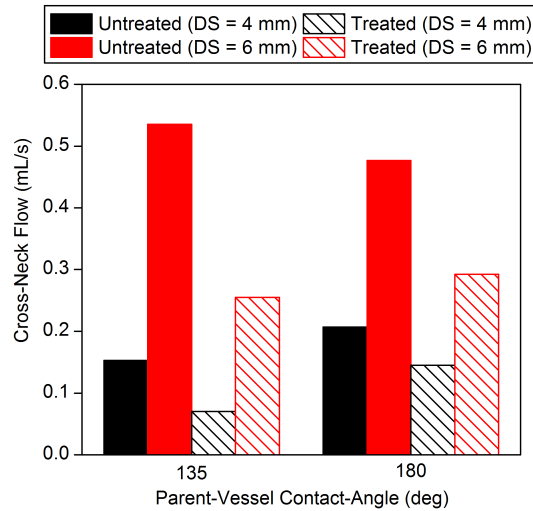


Figure 6.6: Effects of increasing aneurysmal dome size (from black to red boxes) on cross-neck flow keeping inflow angle constant within grouped bars. The solid and patterned boxes correspond to 3 mL/s steady and pulsatile inflow conditions, respectively.

Hemodynamic responses obtained under pulsatile flow conditions agreed with the steady flow responses with a strong positive correlation of 0.98 on average [98]. A comparison of aneurysmal V_{RMS} values calculated in IBTA-3 for steady and pulsatile flow conditions is provided in Figure. 6.7.

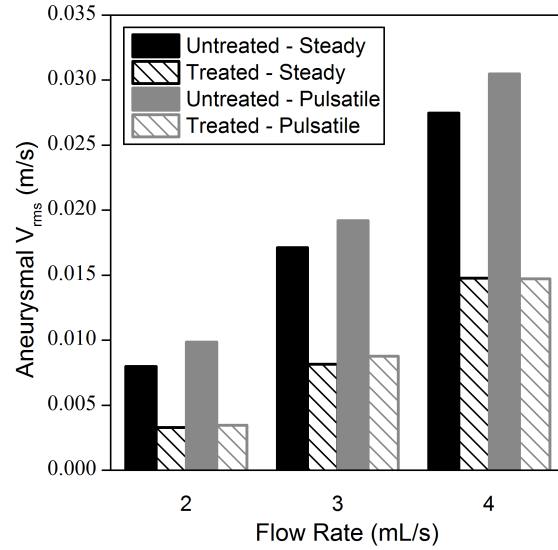


Figure 6.7: Effects of steady (solid boxes) and pulsatile (patterned boxes) inflow conditions on aneurysmal V_{RMS} for IBTA-3.

Although both factors, DS and PD, affected hemodynamics considerably, statistical examination of factor contributions revealed that PD had the greatest impact on responses in and around the aneurysmal volume (i.e., V_{RMS} and WSS), while DS has the greatest impact on the neck-plane response (i.e., CNF). These results are presented graphically in Figure. 6.8 where the contributions of each of the factors (and their interactions) to the effects on the four calculated hemodynamic responses are visualized. Analyzing the effects of geometry on hemodynamics before and after treatment (as two

2x2 factorial designs) revealed that DS was the greatest contributor to the effects on hemodynamics in both cases, as shown in Figure 6.9. It was interesting to note that although the effects of IA on pre-treatment hemodynamics were negligible in most cases, the contributions of IA toward modifying aneurysmal V_{RMS} and CNF after treatment grew to 25.46% and 9.94%, respectively.

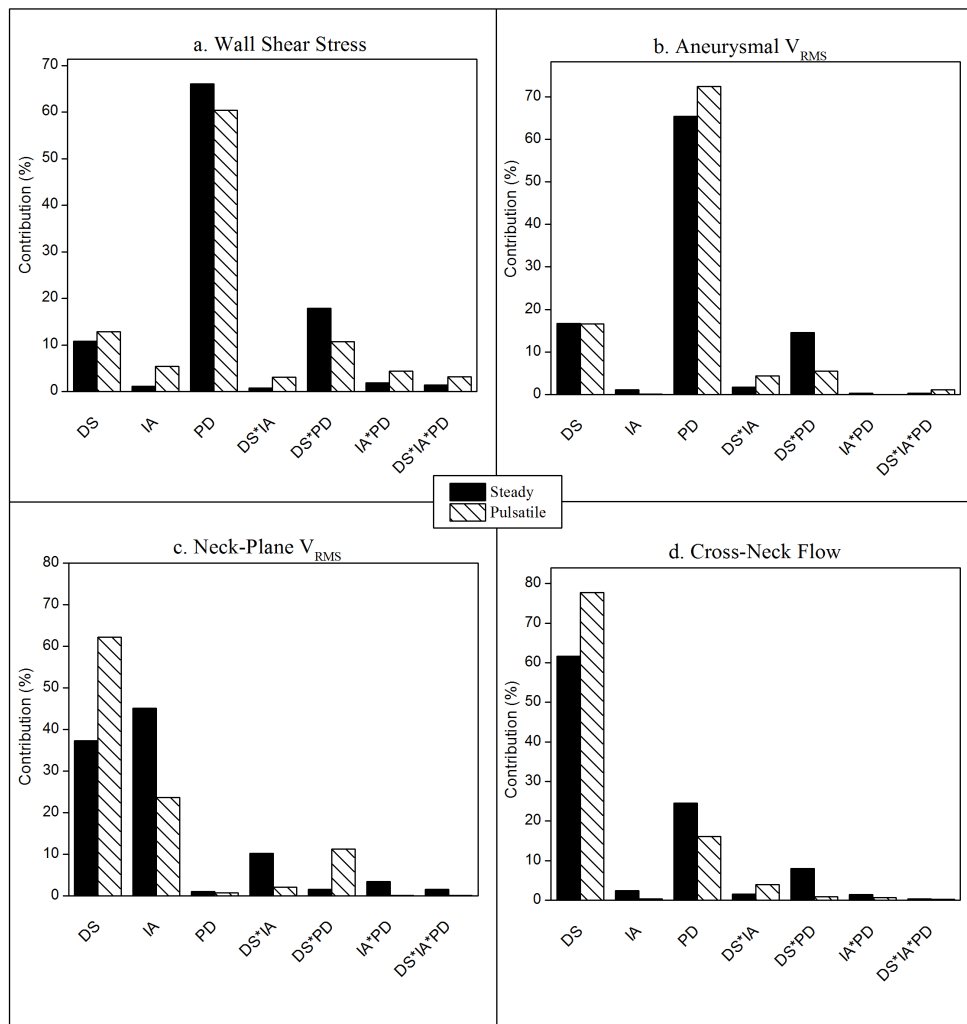


Figure 6.8: Percentage contributions of dome size (DS), inflow angle (IA), and packing density (PD) on (a) aneurysmal wall shear stress, (b) aneurysmal V_{RMS} , (c) neck-plane V_{RMS} , and (d) cross-neck flow.

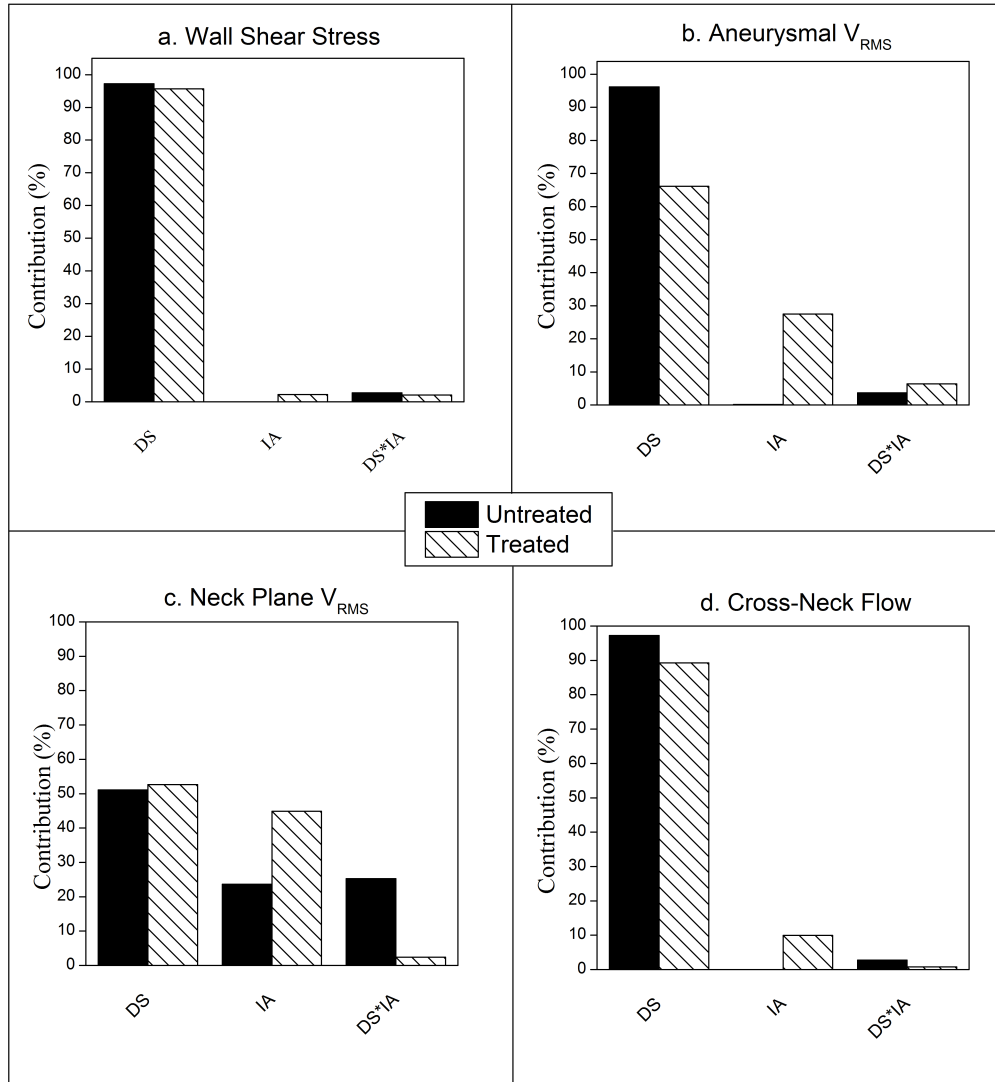


Figure 6.9: Percentage contributions of dome size and inflow angle on untreated (solid boxes) and treated (patterned boxes) hemodynamics under steady flow conditions.

CNF was calculated from the experimental data and compared against the corresponding CFD results for validation. Figure 6.10 represents the CNF values calculated using CFD and measured using PIV at a 3 ml/s steady inflow rate before and after treatment. Although some differences in absolute values of CNF were observed

between the CFD and PIV data, the overall trends were very similar between the two groups. Strong correlations (i.e., 0.98 and 0.95 before and after treatment, respectively, across all steady flow rates) were observed between experimental and computational results. The average discrepancy between the PIV and CFD results was 37.07%, across all steady flow rates (before and after treatment). A qualitative comparison between CFD and PIV velocity vector plots from IBTA-8 at a 3 ml/s inflow rate is also provided in Figure. 6.11.

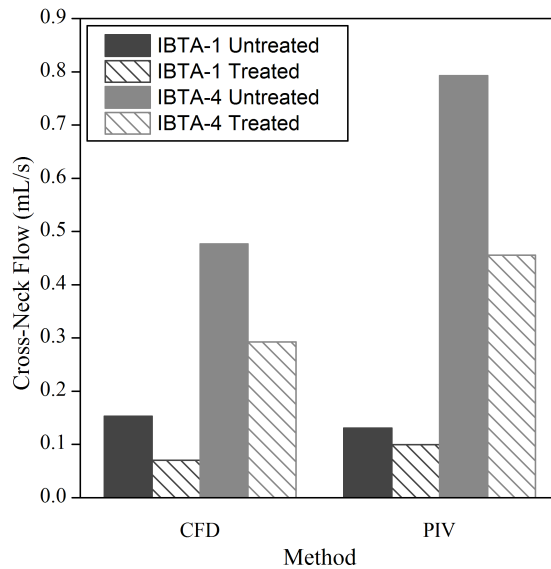


Figure 6.10: CFD to PIV comparison of cross-neck flow in untreated (solid boxes) and treated (patterned boxes) IBTA models at a 3 mL/s steady inflow rate.

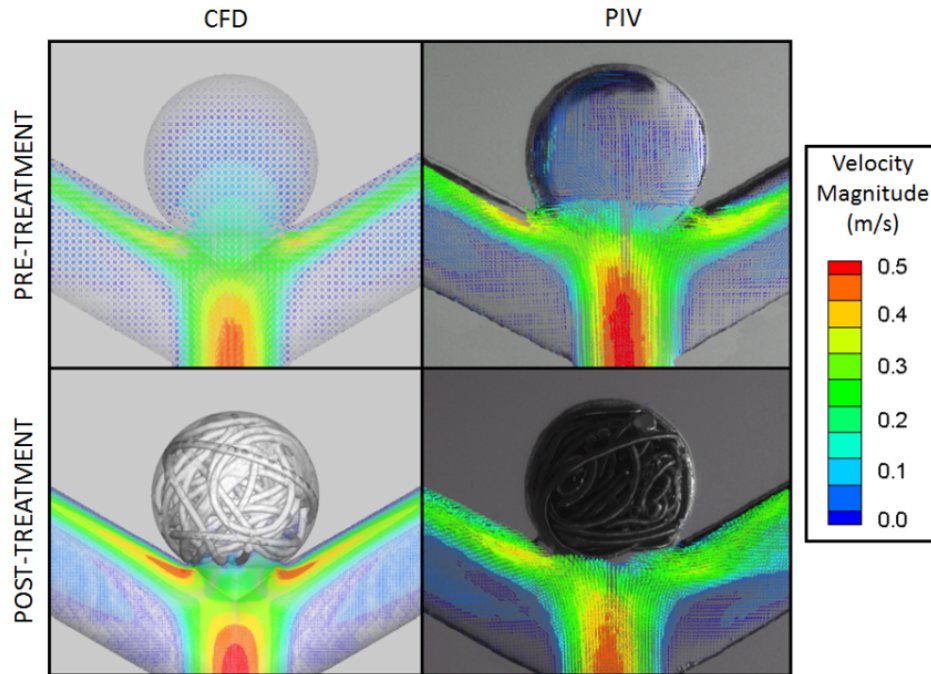


Figure 6.11: CFD (left) and PIV (right) velocity vector distribution, color-coded by velocity magnitude, in IBTA-8 at 3 mL/s steady inflow rate.

6.3.2 Idealized Sidewall Aneurysm Results

The hemodynamic responses (aneurysmal WSS, aneurysmal and neck-plane V_{RMS} , and CNF) calculated from CFD in all four investigated IBTA templates, pre- and post-treatment with embolic coils are presented in Table 6.3. Similar to the IBTA templates, measured hemodynamic responses post-treatment with embolic coils decreased all calculated hemodynamic responses. Figure 6.12 illustrates the effects of embolic coil treatment towards modifying intra-aneurysmal flow patterns all four ISA templates. Example of the effects of DS and IA on pre- and post treatment CNF and aneurysmal

V_{RMS} , respectively, is illustrated in Figure 6.13. In general, increasing DS and IA increased all calculated hemodynamic responses.

Table 6.3: Hemodynamic responses calculated from CFD for all four ISA templates and across all investigated steady flow rates before and after treatment with embolic coils.

Model	Flow Rate (mL/s)	Untreated 0% PD				Treated PD 26% (DS: 4mm) PD 27% (DS: 6 mm)			
		Aneurysm		Neck-plane		Aneurysm		Neck-plane	
		WSS	V_{RMS}	V_{RMS}	CNF	WSS	V_{RMS}	V_{RMS}	CNF
		(Pa)	(m/s)	(m/s)	(mL/s)	(Pa)	(m/s)	(m/s)	(mL/s)
ISA – 3 (4 mm, 90°)	2	0.009	0.004	0.024	0.009	0.000	0.003	0.020	0.005
	3	0.014	0.005	0.033	0.015	0.001	0.004	0.027	0.008
	4	0.019	0.007	0.041	0.021	0.001	0.005	0.033	0.012
ISA – 4 (4 mm, 135°)	2	0.013	0.005	0.026	0.029	0.001	0.004	0.021	0.020
	3	0.051	0.013	0.046	0.072	0.002	0.010	0.038	0.061
	4	0.161	0.024	0.071	0.128	0.005	0.019	0.064	0.115
ISA – 7 (6 mm, 90°)	2	0.010	0.005	0.029	0.028	0.001	0.002	0.018	0.014
	3	0.015	0.007	0.038	0.046	0.002	0.002	0.024	0.022
	4	0.021	0.008	0.046	0.060	0.003	0.003	0.030	0.030
ISA – 8 (6 mm, 135°)	2	0.029	0.011	0.056	0.097	0.003	0.004	0.039	0.061
	3	0.115	0.023	0.093	0.196	0.010	0.011	0.074	0.150
	4	0.316	0.039	0.133	0.313	0.022	0.020	0.11	0.267

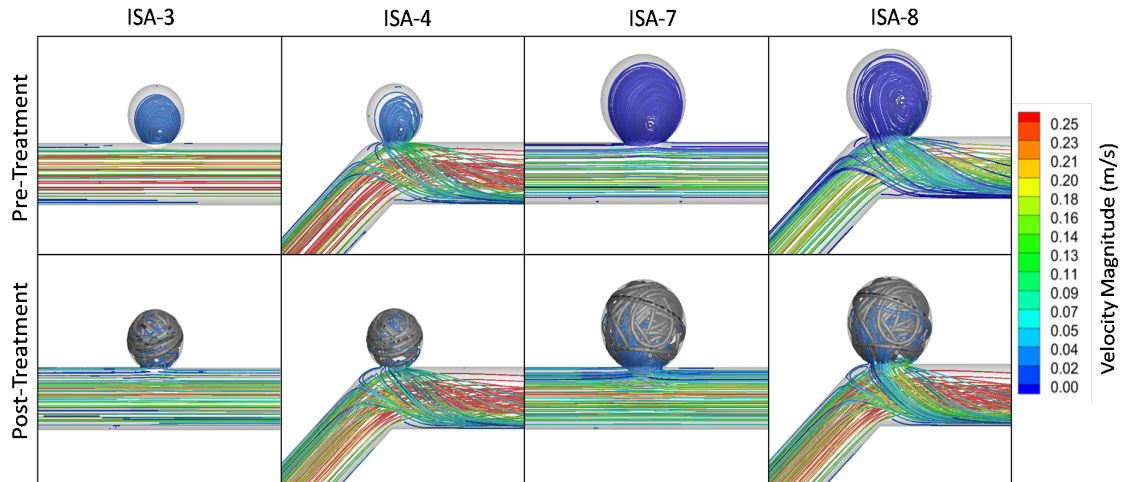


Figure 6.12: Velocity streamtraces, colored-coded by velocity magnitude, in (top) pre- and (bottom) post-treatment ISA templates.

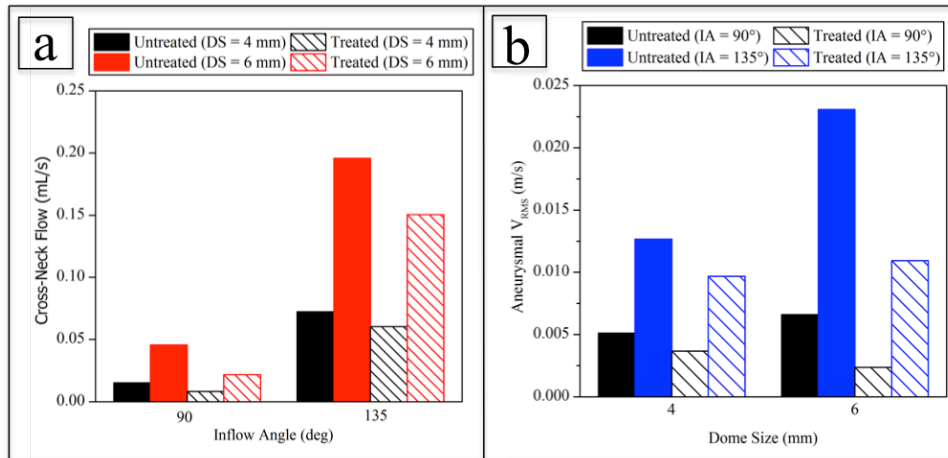


Figure 6.13: Effects of changing (a) dome size on cross-neck flow, and (b) inflow angle on aneurysmal V_{RMS} , keeping the other factor constant within the grouped bars at a steady inflow rate of 3 mL/s.

Statistical examination of the effects of DS, IA, and PD (as a 2x2x2 factorial design) on hemodynamics revealed that the IA had the largest effect on aneurysmal and neck-plane V_{RMS} , and CNF, while PD had the largest effects only on aneurysmal WSS, as

illustrated in Figure 6.14. These results were slightly different from the results obtained from the IBTA templates where PD had the largest contribution towards modifying both aneurysmal responses. The contributions of geometry on effects on pre- and post-treatment hemodynamics were also investigated, as two 2x2 factorial designs, and the results are graphically presented in Figure 6.15.

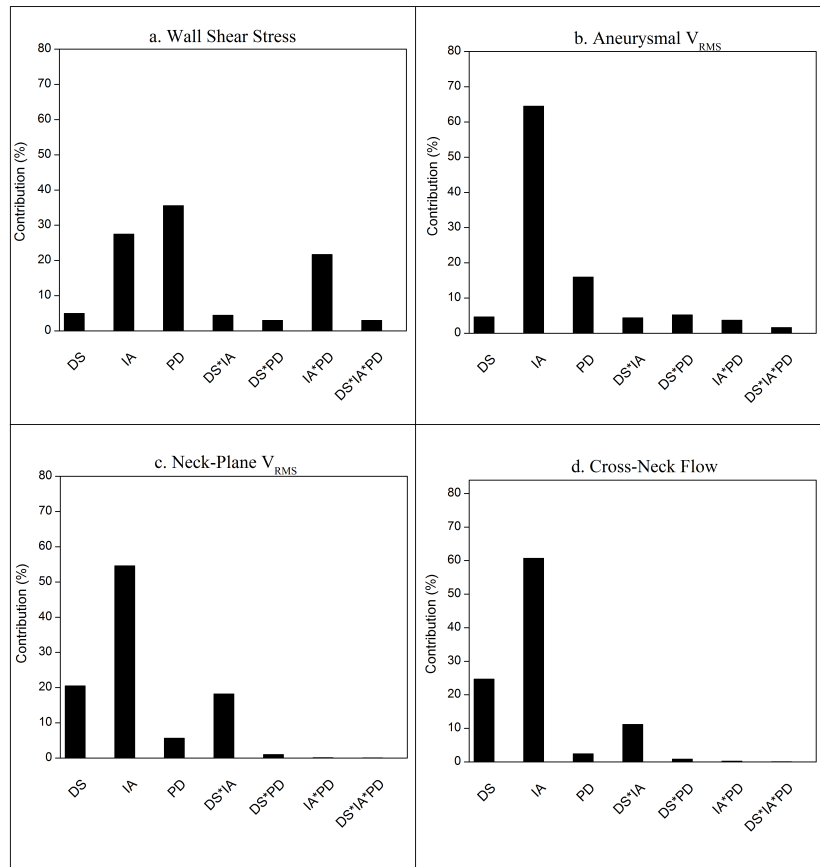


Figure 6.14: Percentage contribution of the effects of dome size, inflow angle, and packing density on (a) aneurysmal wall shear stress, (b) aneurysmal V_{RMS} , (c) neck-plane V_{RMS} , and (d) cross-neck flow in the idealized sidewall aneurysm templates.

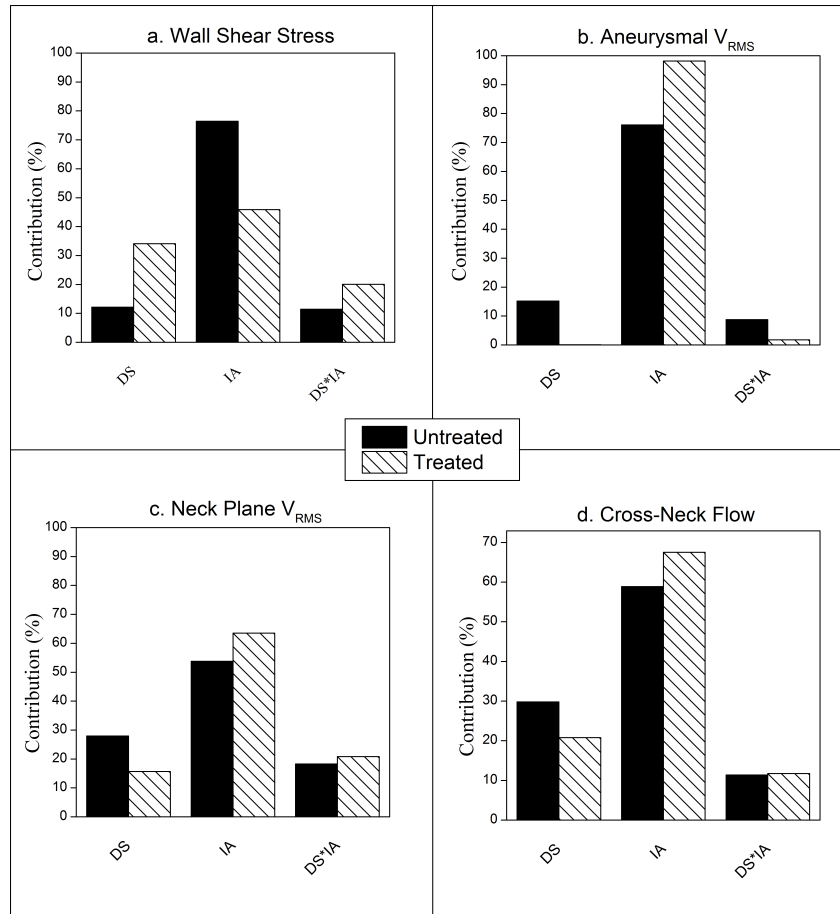


Figure 6.15: Percentage contributions of DS and IA on untreated (solid boxes) and treated (patterned boxes) hemodynamic responses.

6.4 Discussion

6.4.1 Effects of Geometry and Treatment on Idealized Bifurcation Aneurysm Hemodynamics

The results of this study demonstrated that among the geometric and treatment factors examined, PD made the greatest contributions to effects on V_{RMS} and WSS. This result is

not surprising, as PD is often the variable that clinicians focus on most in working toward a successful coiling outcome. However, in the context of CNF, DS was found to have the greatest impact, while the IA had the largest impact on neck-plane V_{RMS} . As a whole, the results thus indicate that the treatment factor (i.e., PD) affects hemodynamics most in the aneurysm (V_{RMS} and WSS are both quantified in or around the aneurysmal sac), while the geometric factors (i.e., DS and IA) affect hemodynamics most at the neck of the aneurysm (CNF and neck-plane V_{RMS} is evaluated at the aneurysmal neck-plane, upstream of the coil mass).

Another interesting finding from this study is that although IA had relatively little impact on aneurysmal hemodynamics in the untreated case, the factor became much more impactful after treatment. This result demonstrates that the geometric factors that influence aneurysmal hemodynamics can be different for untreated aneurysms and those same aneurysms after coiling. Treatment design and execution may thus benefit from considering both the geometric factors that dictate pre-treatment hemodynamics, as well as the factors that could play a greater role in dictating hemodynamics after treatment.

6.4.2 Effects of Geometry and Treatment on Idealized Sidewall Aneurysm Hemodynamics

Statistical examination of the geometric and treatment main effects on aneurysmal and neck-plane hemodynamics revealed that IA made the largest contribution (over 54%) to effects on aneurysmal and neck-plane V_{RMS} , and CNF. The effects of PD on WSS, on the other hand, were similar to the IBTA templates where PD made the largest contribution

towards effects on WSS. Aneurysmal DS made the second largest contributions to modifying both neck-plane responses. Combinations of factor interactions also made contributions to effects of neck-plane hemodynamics and WSS, the most prominent of which were the combinations of IA with DS or PD.

In contrast to the effects of geometry on IBTA hemodynamics, IA consistently played the greatest role on modifying pre- and post-treatment hemodynamics in the ISA templates. It was interesting to note that while DS made the second largest contribution to effects on V_{RMS} in the pre-treatment templates, the combination of DS and IA made the second largest contribution towards modifying V_{RMS} in the post-treatment templates.

6.4.3 Clinical Implications

The possible clinical implications of these findings can be further appreciated in the context of unsuccessful treatment outcomes, such as aneurysmal rupture and recurrence. Aneurysmal rupture typically occurs beyond the neck in the aneurysmal sac, so PD may be the most important factor to consider in designing and executing a treatment in a bifurcation aneurysm so as to prevent rupture. However, in the case of a sidewall aneurysm, the effects of IA must also be taken into consideration in addition to PD. Aneurysmal recurrence, on the other hand, manifests when the neck of the aneurysm fails to fully close, so we hypothesize that DS may be the most important factor to consider in targeting eventual aneurysmal occlusion in a bifurcation aneurysm, while the IA may be the most important factor to consider in targeting a sidewall aneurysm occlusion. This hypothesis is also supported by clinical findings in that aneurysms with large DS have

been firmly associated with elevated recurrence rates [112], [113]. Turjiman et al. noted that in addition to large aneurysm DS, more obtuse IA (increased IA) correlated with unsatisfactory occlusion post-coiling [114]. More diligent Post-treatment follow up may thus be called for in order to monitor for the higher likelihood of recurrence associated with large DS aneurysms.

While this study was successful in providing greater insight into the roles that different geometric factors may play in aneurysmal hemodynamics before and after treatment with embolic coils, it is not without a few limitations. First, the study focused on idealized models of aneurysms, but in the clinic, each patient-specific anatomical case will certainly behave differently. For example, the anatomical aneurysm presented in Figure 6.16 demonstrates higher magnitude WSS values but less considerable reductions in WSS after coiling (i.e., 60.0% reduction as opposed to 79.3% in the idealized case). The overall trend is fundamentally similar though. The example in Figure 6.16 also illustrates how hemodynamics at the neck plane can change following treatment, as the WSS levels near the neck clearly elevate after coiling.

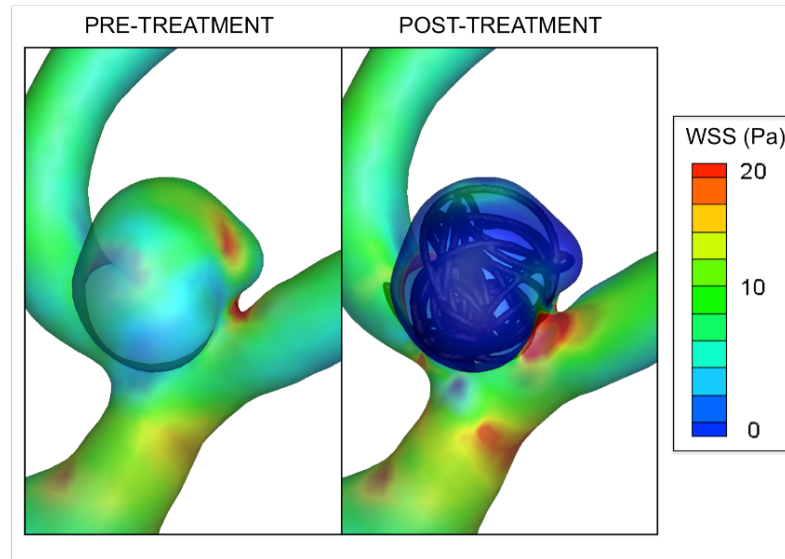


Figure 6.16: WSS changes in anatomical bifurcation aneurysm model, before and after treatment with embolic coils, at a 3 mL/s steady inflow rate.

Second, every coil deployment is different, and accordingly different hemodynamic outcomes can present even when the same coils are used to pack an aneurysm to the same PD in repeated trials. However, a study by Babiker et al. has shown that at high PDs like those examined here, different coil deployments effect minimal variation in hemodynamic responses [79]. Third, discrepancies in absolute values of CNF were observed between the computational and experimental IBTA cases. This discrepancy is mainly attributed to differences in the fluid domain examined by CFD and PIV. Unlike CFD, PIV excluded some lower velocity flow regions toward the outskirts of the aneurysmal neck that resulted in higher magnitudes of CNF as compared to the CFD cases. Future work will include the examination of a broader range of anatomical geometries under steady and pulsatile flow conditions, and will continue development of the proposed methods toward interventional planning and optimization in the clinic.

CHAPTER 7

HEMODYNAMIC CHARACTERIZATION OF CEREBRAL ANEURYSM TEMPLATES TREATED WITH PIPELINE EMBOLIZATION DEVICE

7.1 Introduction

Cerebral aneurysms are often treated using flow diverting (FD) stents when embolic coiling or surgical clipping are not viable options. In this technique, a microcatheter containing the low porosity endovascular stent is inserted into the femoral artery and is navigated to the aneurysm site under fluoroscopic guidance. The stent is then deployed across the aneurysm neck using a "push and pull" technique where the device is pushed out of the microcatheter while the microcatheter is pulled back simultaneously. The high density (low porosity) mesh design of the device reduces the inflow of blood into the aneurysm, promoting intra-aneurysmal thrombosis [21], [115]. Over time, vascular reconstruction of the parent-vessel and the aneurysmal neck completely isolates the aneurysm from circulation. The pipeline embolization device (PED) is one such flow diverter often used in clinical practice. PEDs are primarily used to treat large or giant aneurysms (i.e., aneurysms with dome size (DS) > 10 mm), and can be used as a stand-alone treatment for cerebral aneurysms with dome-to-neck ratios (DNR) less than 1.6, where embolic coiling without any adjunctive techniques is not a practical treatment option [19], [21], [22], [25]. Treatment with PEDs are extremely effective, with over 80% 6-month Post-treatment occlusion rates [21]–[23]. However, since majority of the aneurysms found in the general population are under 10 mm, the

effectiveness of PEDs in treating smaller aneurysms are being investigated as well [5], [26].

In this chapter, the effects of geometry and PED treatment on idealized bifurcation and sidewall aneurysm hemodynamics are investigated using computational fluid dynamics (CFD). The effects of cerebral aneurysm geometry on pre- and post-treatment hemodynamics are also investigated. Wide-neck (i.e., DNR = 3:2 or 1.5) cerebral aneurysm templates are chosen for investigation from the full factorial bifurcation and sidewall aneurysm designs described in Chapters 4 and 5.

7.2 Methods

7.2.1 Study Design

Wide-neck cerebral aneurysm templates with 3:2 DNRs were chosen for virtual treatment with PEDs from the idealized basilar tip aneurysm (IBTA) and sidewall aneurysm (ISA) templates described in Chapters 4 and 5. Figure 7.1 (a) shows the templates chosen for investigation (marked with orange bubbles). This facilitated the creation of a 2^2 factorial design, as shown in Figure 7.2 (b), where the red and blue edges of the square represent an increase in DS and inflow angle (IA), respectively, along the direction of the colored arrows. Additionally, two large aneurysm templates (i.e., 6 mm DS) with high DNR (i.e., 2:1), marked with pink bubbles in Figure 7.2 (a) were also investigated. Although a DNR of 2:1 indicated that the aneurysms were good candidates for embolic coiling, more coils are required to achieve packing densities between 20 and 25% for effective treatment

outcomes.

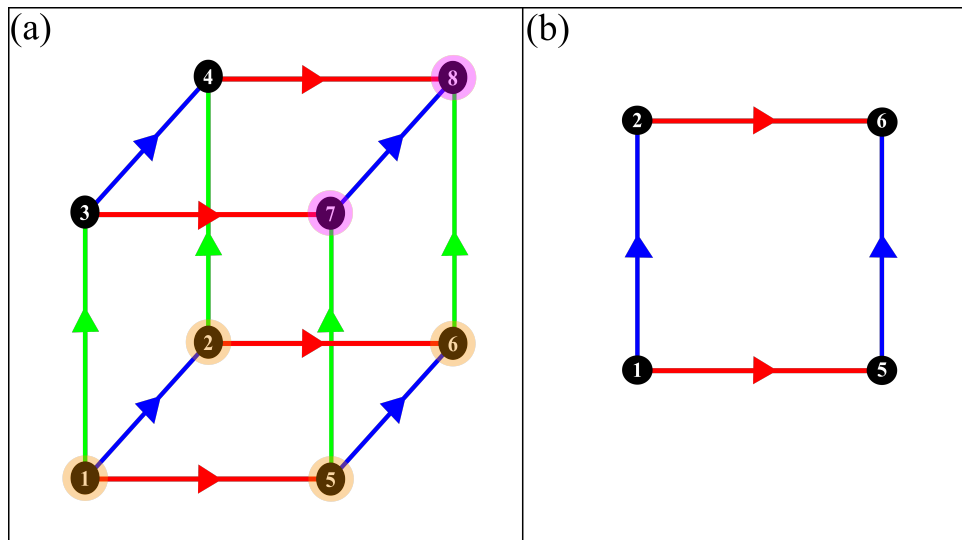


Figure 7.1: (a) Full Factorial design of DS, DNR and IA with orange bubbles representing the 3:2 DNR templates and pink bubbles representing the two templates with 2:1 DNR chosen for investigation with PEDs, and (b) a 2^2 factorial design the wide-neck templates.

7.2.2 Computational Modeling and Virtual Device Deployment

The computational cerebral aneurysm templates were constructed in SolidWorks, as described in Sections 4.2.2.1 and 5.2.2. The IBTA and ISA templates were virtually treated with FE PED models using the EndoVantage Interventional Suite (EVIS) (EndoVantage, Scottsdale, AZ, USA). PEDs of diameter 4.5 mm and length 12 mm were chosen from a library of FE device models. The FE device library was previously validated against geometric and force-based measurements of the physical devices. The devices were first crimped to a diameter of 0.68 mm that represents the inner diameter of

a microcatheter that houses the PED. Several boundary conditions were then prescribed to simulate the deployment procedure using an explicit FE solver. Displacement boundary conditions were then applied to the tip of the virtual microcatheter in order to guide the PED delivery system to the device landing zone, as shown in Figure 7.2 (a) and (b). Device unsheathing was then simulated using a “push and pull” algorithm to imitate clinical PED deployment process, as shown in Figure 7.2 (c) – (f). The optimal device shape was preserved during the virtual deployment process. The final deployed PED configurations in the IBTA and ISA templates are shown in Figures 7.3 and 7.4. The deployed PED models were then exported as VRML files for CFD simulations.

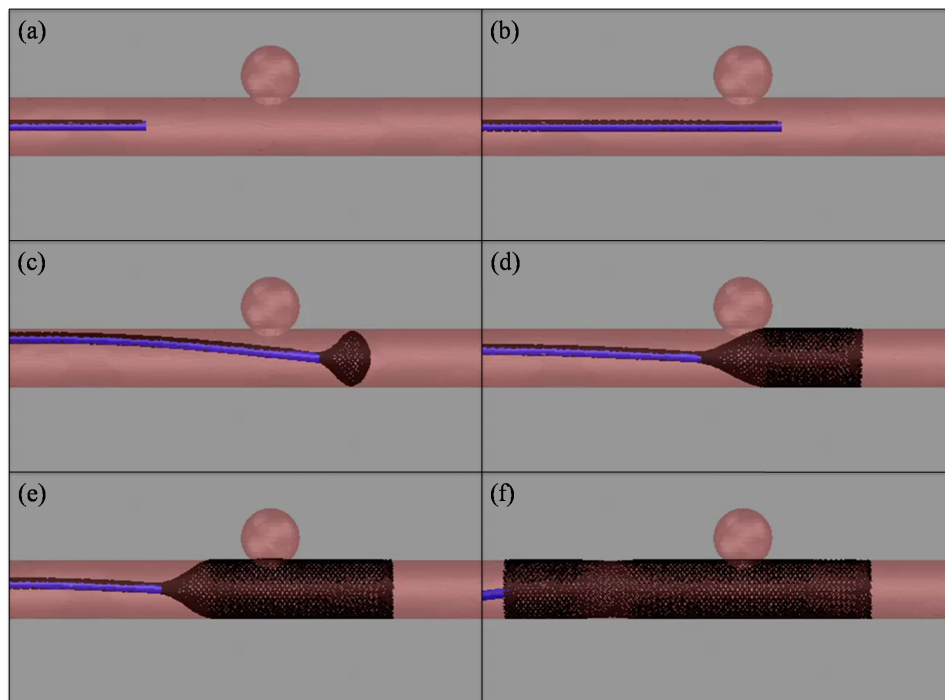


Figure 7.2: Virtual PED deployment process in a sidewall cerebral aneurysm template. (a) and (b) depict displacement of the microcatheter to the device landing zone, and (c) – (f) depict the device unsheathing process.

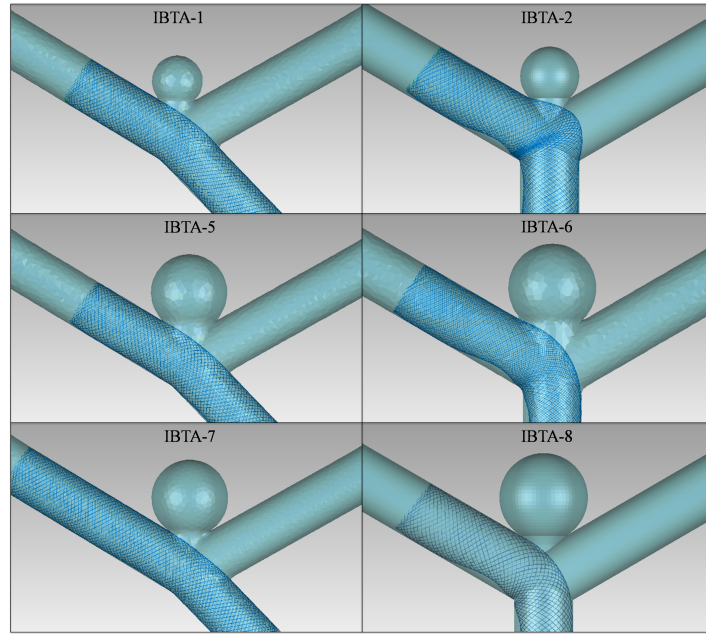


Figure 7.3: IBTA templates virtually treated with pipeline embolization device.

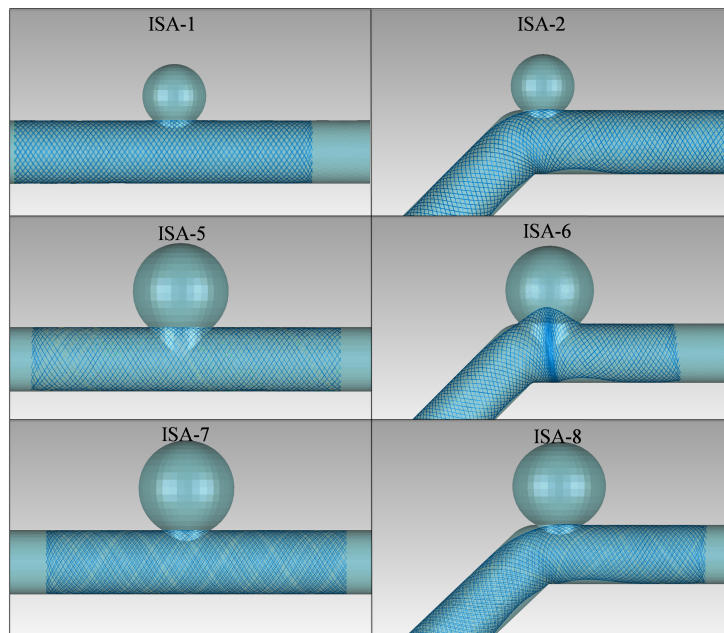


Figure 7.4: ISA templates virtually treated with pipeline embolization device.

7.2.3 Computational Fluid Dynamics (CFD)

The untreated and virtually treated cerebral aneurysm templates were prepared for CFD simulations using ANSYS ICEM 14.1. The blood and PED domains were discretized into unstructured tetrahedral elements using the Octree process. The devices were meshed with a maximum element size of 0.016 mm. The maximum mesh element size chosen for the treated IBTA and ISA templates were based on the results of a mesh refinement study on the untreated templates, as described in Sections 4.2.2 and 5.2.3. The IBTA templates were meshed with a maximum element size of 0.25 mm, and the resulting meshes ranged between 45.57 and 55.16 million mesh elements. The ISA templates were meshed with a maximum element size of 0.17 mm, and the meshes ranged between 43.44 and 53.08 million elements.

The meshed geometries were next imported into ANSYS Fluent for CFD simulations, where blood was modeled as an incompressible and Newtonian fluid. The PED surface and vessel walls were assumed to be rigid, with a no-slip condition imposed at the walls. A second-order scheme was used for momentum discretization, and the SIMPLE algorithm was used for pressure-velocity coupling. Steady inflow rates of 2, 3 and 4 mL/s, corresponding to velocities of 0.159, 0.239 and 0.318 m/s, were prescribed at the inlet for all simulations.

IBTA Simulations

Blood was modeled with a density and viscosity of 1500 kg/m^3 and 3.86 cP, respectively,

to match the untreated IBTA cases described in Chapter 5. Resistance outflow boundary conditions were prescribed at the outlets according to equation 5.1. The outlet pressure values calculated from equation 5.1 were 11080, 16620 and 22160 Pa for inflow rates of 2, 3 and 4 mL/s respectively. It is to be noted that the untreated IBTA templates were simulated using a zero pressure (and zero traction) outlet boundary condition, while the treated IBTA templates were simulated using a resistance outflow boundary condition. However, in a study comparing the effects of zero pressure and resistance outlet boundary conditions, it was observed that the aneurysmal hemodynamic responses varied by less than 5% between the two cases.

ISA Simulations

Blood was modeled with a density and viscosity of 1060 kg/m^3 and 3.71 cP, respectively. Steady inflow rates of 2, 3 and 4 mL/s were investigated, and a resistance outflow boundary condition was prescribed at the ISA outlet. The outlet pressures were calculated according to equation 5.1, and were 11940, 17910 and 23880 Pa for inflow rates of 2, 3 and 4 mL/s, respectively.

7.2.4 Data Analysis

Distal aneurysmal wall shear stress (WSS), aneurysmal and neck-plane root-mean-square velocity magnitude (V_{RMS}) and cross-neck flow (CNF) were calculated from the CFD simulation results using Tecplot 360. Changes in hemodynamic responses

before and after treatment with PED, and changes with respect to increase in a single geometric factor (with the other factor held constant) were calculated. The hemodynamic responses obtained from the large dome, narrow neck IBTA and ISA templates (i.e., DS = 6 mm, and DNR = 2:1) treated with PED were also directly compared to the same templates treated with embolic coiling (described in Chapter 6) to investigate the impact of the two endovascular devices on post-treatment hemodynamics.

The hemodynamic responses were then examined using a statistical analysis software to determine the contributions of the two geometric factors (i.e., DS and IA) and one treatment factor (i.e., treatment with PED) towards modifying cerebral aneurysm hemodynamics. The data was first analyzed as 2^3 factorial design with DS, IA, and treatment as the three factors. The two levels of treatment corresponded to untreated and treated conditions. The percentage contribution of each factor, and interactions, towards modifying hemodynamics was calculated by dividing the sum of squares (SS) values for each individual factor by the total SS value, as shown in equation 6.2. Following the two 2^3 factorial designs, the pre- and post-treatment data were analyzed as two 2×2 factorial designs to understand the effects of geometry on pre- and post-treatment hemodynamics.

7.3 Results

7.3.1 Idealized Bifurcation Aneurysm Results

Increasing aneurysmal DS from 4 to 6 mm (keeping IA constant) resulted in an increase in aneurysmal and neck-plane V_{RMS} , CNF, and WSS in the pre- and post-treatment IBTA

templates (except for WSS in one untreated model pair). Please note that the untreated and treated results will be presented in the following form: (*untreated result, treated result*). In general, increasing DS increased aneurysmal V_{RMS} by (45.56%, 41.24%), neck-plane V_{RMS} by (66.67%, 12.05%), CNF by (195.69%, 134.03%), and WSS by (26.68% and 74.45%), across all models and flow rates. An example of the effect of increasing DS on neck-plane V_{RMS} is shown in Figure 7.5 (change from black to red boxes). Changing IA, however, did not have consistent effects on pre- and post-treatment hemodynamics.

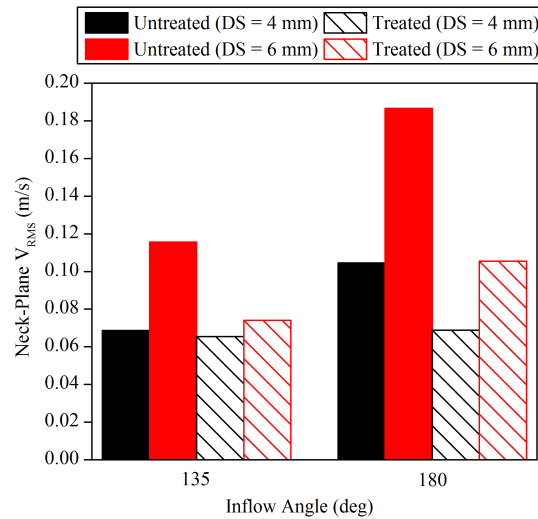


Figure 7.5: Effects of increasing aneurysmal dome size on neck-plane V_{RMS} in the idealized bifurcation aneurysm templates, at a steady inflow rate of 3 mL/s.

Examination of pre- and post-treatment hemodynamics in IBTA-7 and 8 templates allowed for the examination of the effects DNR change between the large dome templates. As in the case of the untreated IBTA results presented in Chapter 4, increase in DNR from 3:2 to 2:1 decreased all calculated neck-plane and aneurysmal hemodynamic

responses, as illustrated in Figure 7.6. Increase in DNR decreased neck-plane V_{RMS} by (51.10%,33.23%), aneurysmal V_{RMS} by (48.70%,54.03%), WSS by (42.46%,71.71%), and CNF by (58.76%,58.19%).

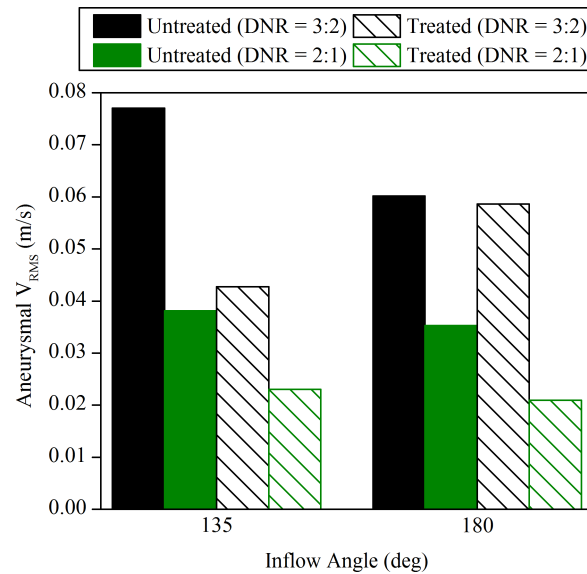


Figure 7.6: Effects of increasing DNR (from black to green boxes) in untreated (solid boxes) and treated (patterned boxes) IBTA templates.

The hemodynamic responses calculated from the steady CFD results in the wide-neck (3:2 DNR) templates were then analyzed as a 2x2x2 factorial design with DS, IA and Treatment as the three main factors to determine the percentage contribution of each factor (and interactions) towards modifying a hemodynamic response. The results are illustrated in Figure 7.7. Aneurysmal DS made the largest contribution towards modifying the neck-plane hemodynamic responses with 78.70% and 36.01% contribution towards modifying neck-plane V_{RMS} and CNF, respectively. DS also made the second largest

contribution towards effects on aneurysmal V_{RMS} (43.08%). The effects of treatment had the largest effect on modifying aneurysmal V_{RMS} by 44%, and second largest effect on neck-plane V_{RMS} by 29.09%. Several factor interactions also played important roles (as high as 27.68% contribution) in modifying IBTA hemodynamics, most prominent of which were the interactions between IA and Treatment on WSS, and interactions between DS, IA and Treatment on WSS, and aneurysmal V_{RMS} .

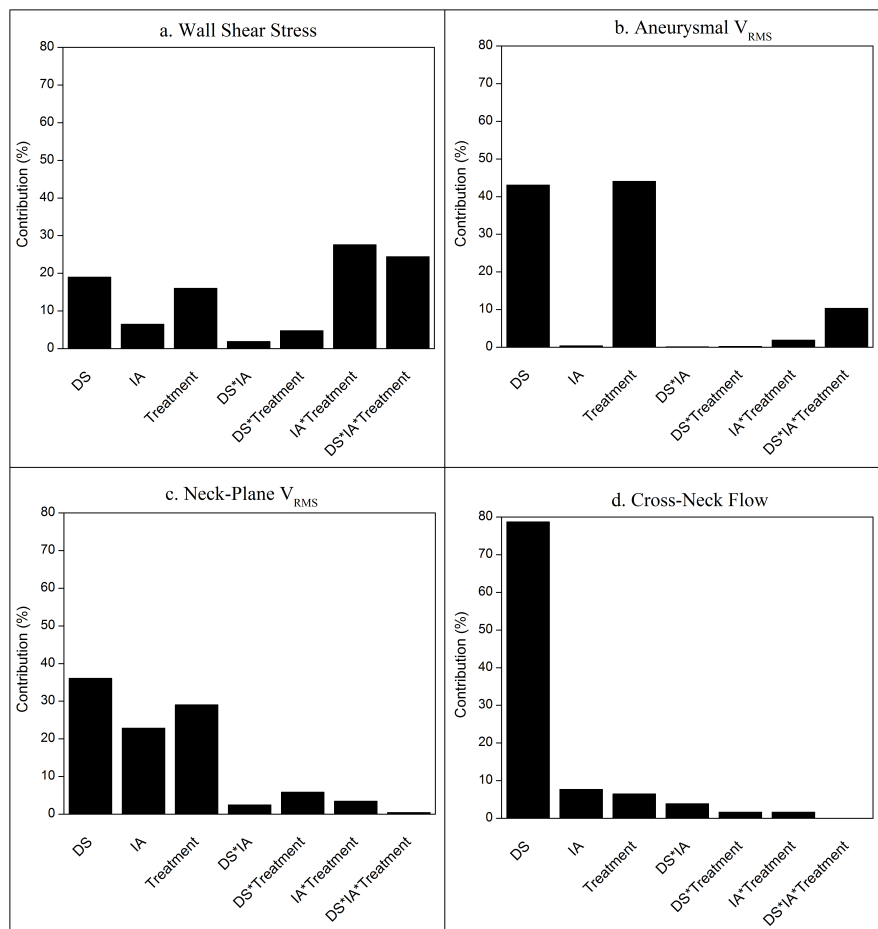


Figure 7.7: Percentage contribution of DS, IA and treatment with PED on modifying aneurysmal and neck-plane hemodynamic responses.

The hemodynamic responses obtained from the 3:2 DNR IBTA templates were also investigated as a 2x2 factorial design to understand the effects of aneurysm geometry on hemodynamics, before and after virtual treatment with a PED, illustrated in Figure 7.8. DS made the greatest contribution (over 47%) towards modifying all hemodynamic responses (except WSS in the pre-treatment templates). IA, on the other hand, had the most effect on WSS (57.63%), and the second largest effect on modifying neck-plane V_{RMS} and CNF in the untreated IBTA templates, and the second largest effect on modifying treated neck-plane V_{RMS} . The combination of DS and IA played important roles in modifying pre- and post-treatment hemodynamics (over 13% and as high as 37.88%). It was interesting to note that while the contribution of DS on WSS was less than 5% in the untreated case, the contribution of DS on treated WSS increased to 68%.

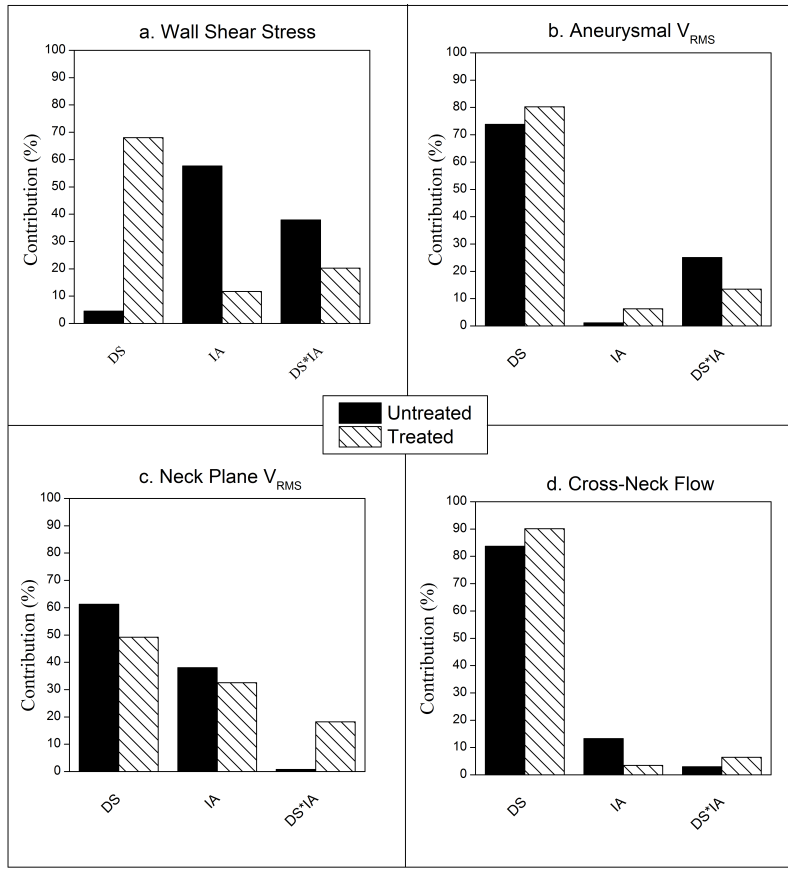


Figure 7.8: Effects of the geometric factors (i.e., DS and IA) on pre- and post-treatment IBTA hemodynamics.

7.3.2 Idealized Sidewall Aneurysm Results

Virtual treatment with PED in the ISA templates decreased WSS, aneurysmal V_{RMS} , neck-plane V_{RMS} and CNF by 87.12%, 76.65%, 70.52% and 50.71%, respectively, across all templates and flow rates. Increasing DS in the wide-neck ISA templates increased all calculated aneurysmal and neck-plane hemodynamic responses. The effects were more prominent in the 135° ISA templates, and in the treated ISA templates. On average across all templates and flow rates, increasing DS increased WSS by (93.89%,219.18%),

aneurysmal V_{RMS} by (66.89%,161.88%), neck-plane V_{RMS} by (56.57%,174.25%) and CNF by (272.29%,297.53%), where (*change1,change2*) denote untreated and treated percentage change, respectively. As observed in the untreated and coiled ISA templates, IA also affected treatment with PED. On average, increase in IA from 90° to 135° increased WSS by (1134.06%,1542.13%), aneurysmal V_{RMS} by (362.72%,705.11%), neck-plane V_{RMS} by (201.14%,771.56%) and CNF by (362.94%,598.16%). Example of the effects of increase in DS (from black to red boxes) on neck-plane V_{RMS} and increase in IA (from black to blue boxes) on aneurysmal V_{RMS} is illustrated in Figure 7.9.

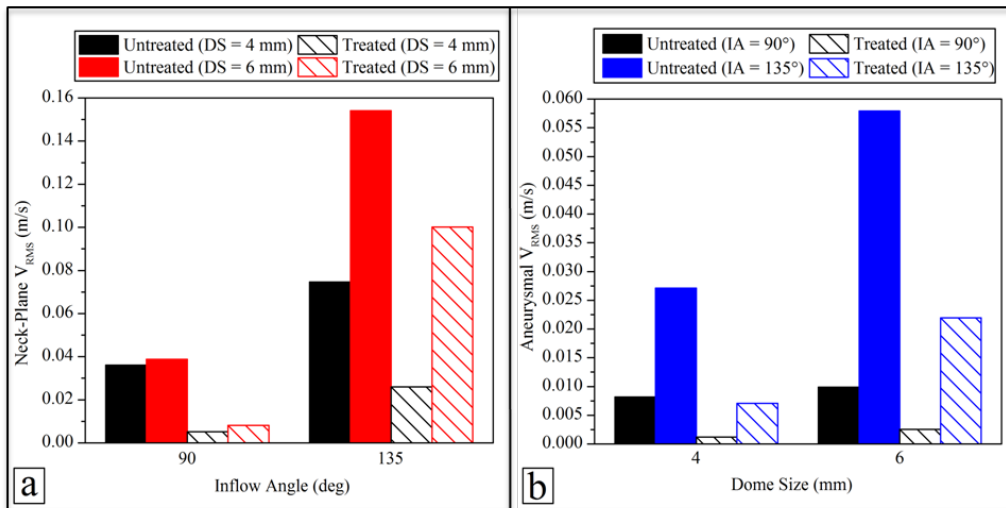


Figure 7.9: Effects of increasing (a) DS on neck-plane V_{RMS} , and (b) IA on aneurysmal V_{RMS} for a 3 mL/s steady inflow rate.

Statistical examination of the two geometric factors (i.e., DS and IA) and one treatment factor (i.e., treatment with PED) as 2x2x2 factorial design demonstrated that the IA made the largest contribution to effects on all calculated aneurysmal and neck-plane hemodynamic responses, by over 22%. Treatment with PED made the second

highest contribution to effects on ISA hemodynamics, while DS made the third highest contribution to effects on all calculated hemodynamic responses (except WSS). As in the case of the IBTA templates, several factor interactions made noteworthy contributions to effects on hemodynamics. The most prominent factor interaction(s) was the interactions of IA with Treatment or DS (greater than 14%). Result from the 2x2x2 factorial analysis is shown in Figure 7.10.

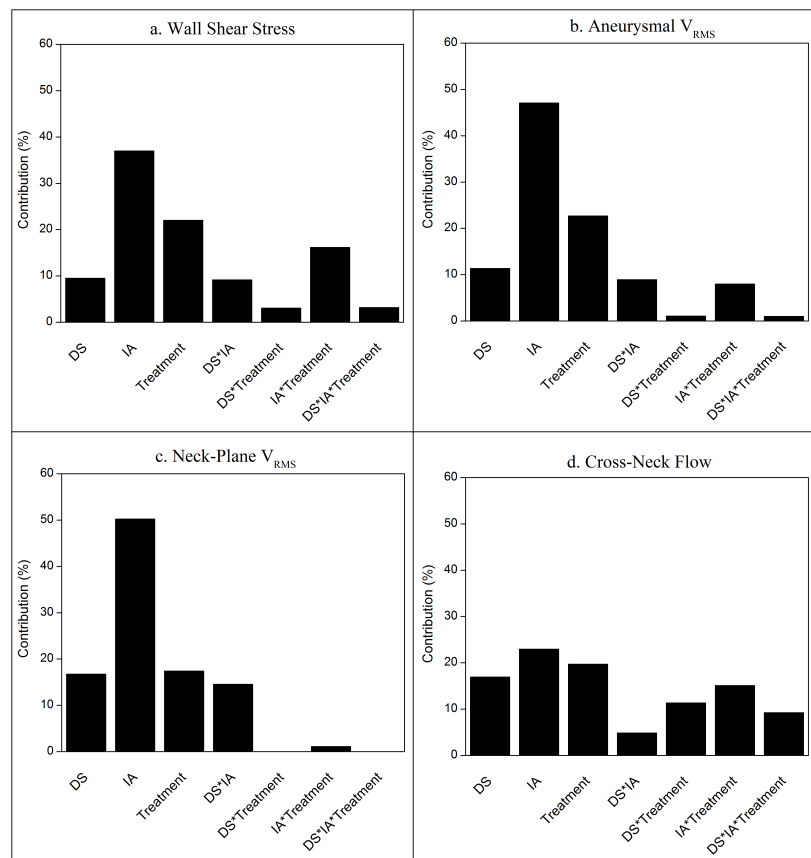


Figure 7.10: Percentage contribution of dome size, inflow angle and PED treatment on ISA hemodynamics.

In order to understand the impact of aneurysm geometry on pre- and post-treatment hemodynamics, the results obtained from the 3:2 DNR templates were analyzed as a 2x2 factorial design. As shown in Figure 7.11, IA made the largest contribution towards modifying WSS, aneurysmal and neck-plane V_{RMS} , and CNF, as high as 72.79%. DS had the second highest contribution towards modifying all hemodynamic responses, except post-treatment CNF. Interactions between DS and IA also played important roles in modifying pre- and post-treatment ISA hemodynamics, sometimes as high as 33.67%.

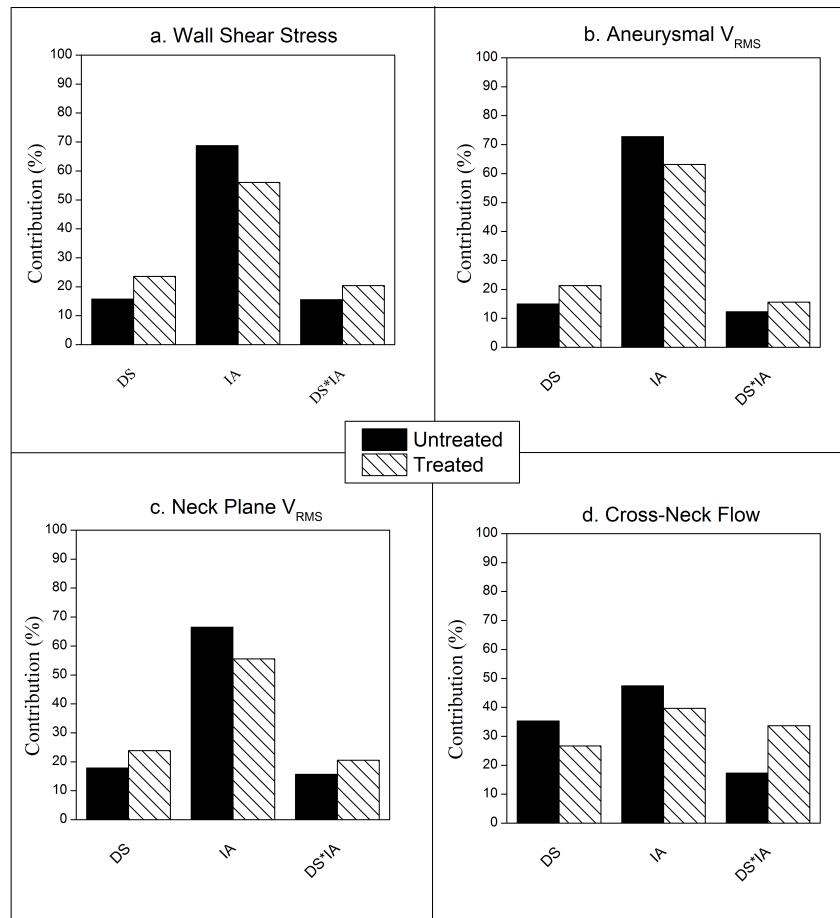


Figure 7.11: Effects of dome size and inflow angle on ISA hemodynamics, before and after treatment with pipeline embolization device.

7.3.3 PED versus Embolic Coiling

In addition to the wide-neck IBTA and ISA templates, two narrow-neck (2:1) templates were investigated to understand the effects different treatment outcomes on cerebral aneurysm hemodynamics. Figure 7.12 represents velocity streamtraces, color-coded by velocity magnitude, in IBTA and ISA templates virtually treated with PED and embolic coils. The IBTA and ISA in the figure have a DS of 6 mm, DNR of 2:1 and inflow angle of 135°.

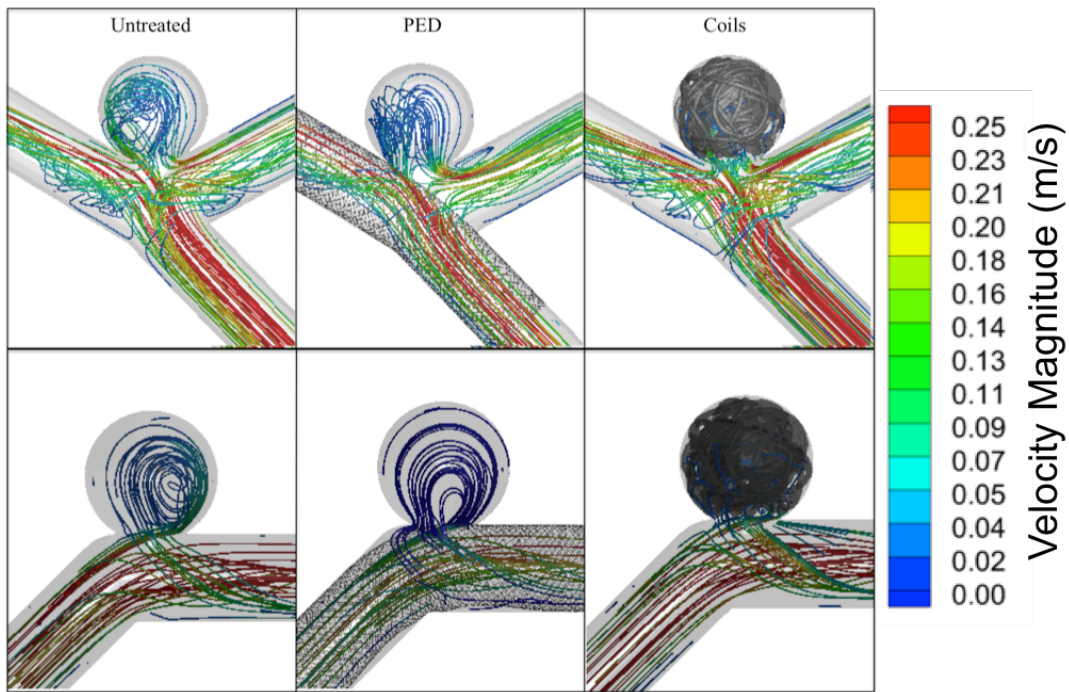


Figure 7.12: Streamtraces color-coded by velocity magnitude in idealized bifurcation and sidewall aneurysm templates (left) pre-treatment, (middle) after virtual treatment with PED, and (right) after virtual treatment with embolic coils.

From the figure, the hemodynamic modification that the endovascular devices effect can be visualized by the reduction in intra-aneurysmal flow velocities. Virtual treatment with PED and embolic coils reduced WSS, aneurysmal and neck-plane V_{RMS} , and CNF in the two investigated IBTA and ISA templates (i.e., template 7 and 8), as illustrated in Figures 7.13 and 7.14.

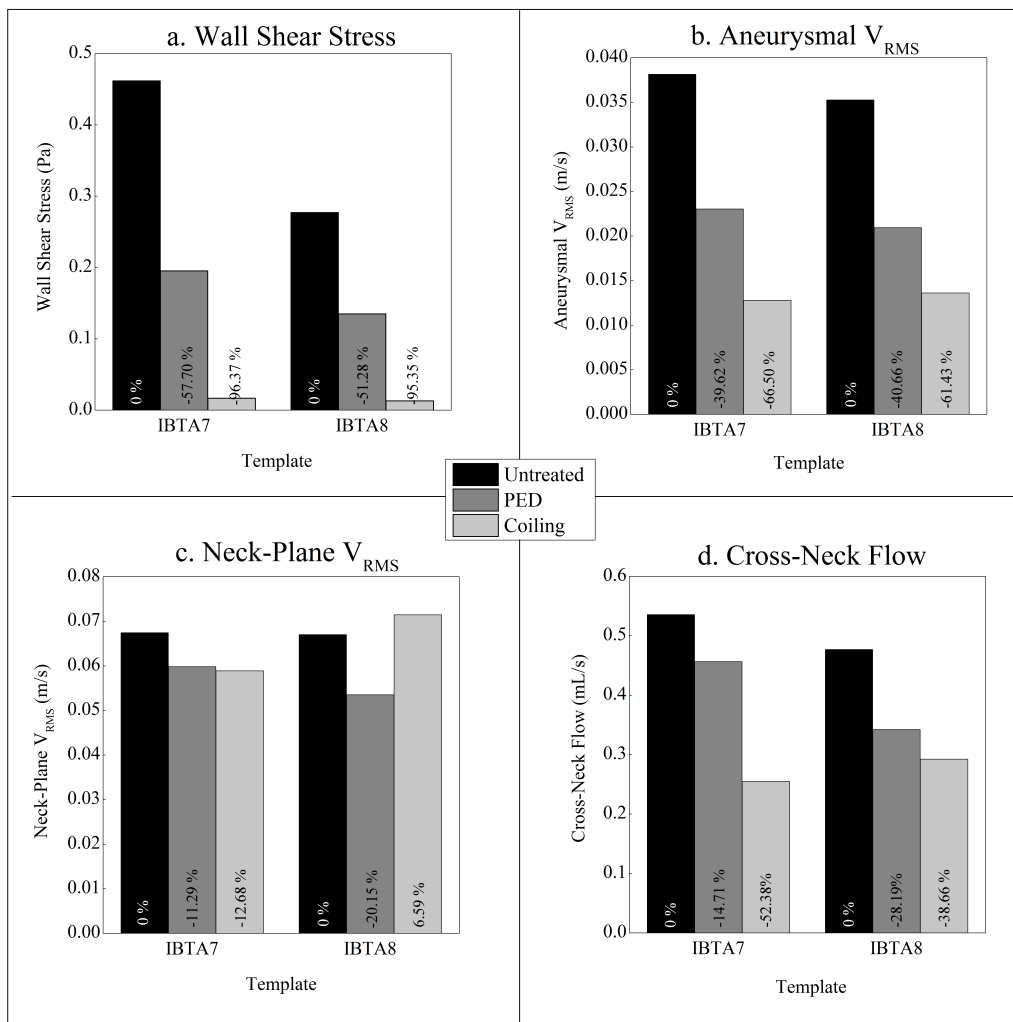


Figure 7.13: Effects of treatment with PED and embolic coils on idealized bifurcation aneurysm templates.

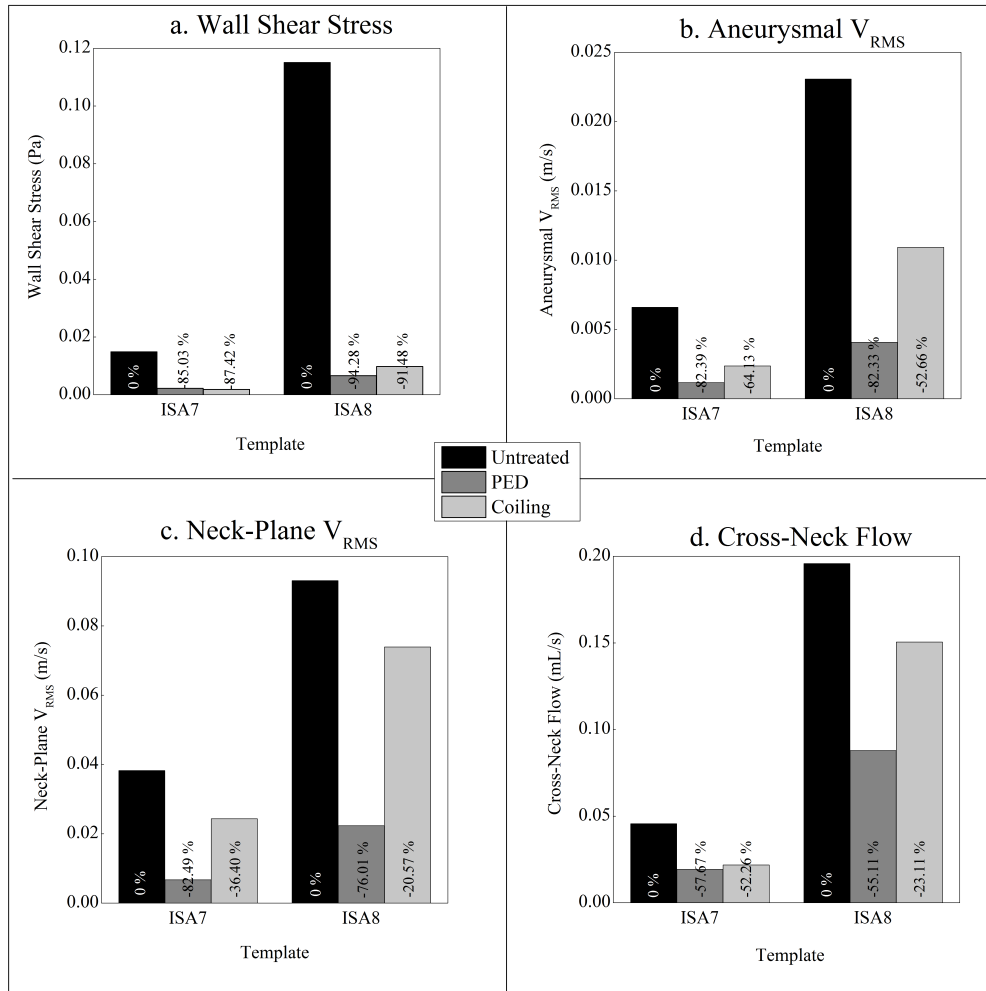


Figure 7.14: Effects of treatment with PED and embolic coils on idealized sidewall aneurysm templates.

The figures clearly depict the impact of aneurysm geometry on endovascular treatment outcomes. While treatment with embolic coils seem to produce better outcomes in the IBTA templates, PEDs may be more suitable for treating the ISA templates. The differences in treatment outcome between the two basic aneurysm variants call for the need of geometric/hemodynamic basis for cerebral aneurysm evaluation and treatment planning.

7.4 Discussion

Endovascular devices such as embolic coils and PEDs isolate the aneurysm from circulation by reducing intra-aneurysmal hemodynamics to promote thrombus formation within the aneurysm dome. Understanding cerebral aneurysm hemodynamics prior to treatment, and after treatment with endovascular devices is critical to cerebral aneurysm evaluation and treatment planning.

7.4.1 Effects of Geometry and Treatment on IBTA and ISA Templates

Treatment of the idealized bifurcation and sidewall aneurysm templates with PEDs reduced intra-aneurysmal hemodynamics indicating a positive treatment outcome. Changes in aneurysm geometry (i.e., DS, IA, and DNR) affected aneurysmal and neck-plane hemodynamics. Increasing the DS from 4 to 6 mm increased WSS, aneurysmal and neck-plane V_{RMS} , and CNF in the IBTA and ISA templates, before and after treatment with PED. IA, on the other hand, had the most effect on ISA hemodynamics where increase from 90° to 135° increased all calculated hemodynamic responses. Statistical examination of the two geometric factors (i.e., DS and IA) and one treatment factor (i.e., PED treatment) demonstrated that while DS made the greatest contribution towards modifying neck-plane responses in the IBTA templates, IA had the largest effects on all computed hemodynamic responses. Treatment with PED had the largest contribution only to effects of aneurysmal V_{RMS} in the IBTA templates. However, in the case of the ISA templates, treatment with PED had the second largest contribution towards effects on

WSS, aneurysmal and neck-plane V_{RMS} , and CNF. The findings indicate that the impact of geometric and treatment factors on hemodynamics in the two main cerebral aneurysm variants are quite different, and need to be characterized in order to better inform clinical decisions.

7.4.2 Effects of Aneurysm Geometry on Treatment Outcomes

This study also investigated the effects of two different endovascular devices, i.e., PED and embolic coils, on IBTA and ISA hemodynamics. Figure 7.12 – 7.14 clearly indicate the different hemodynamic environments the two devices effect on the bifurcation and sidewall aneurysm geometries. The findings indicated that while embolic coiling produced greater hemodynamic reductions in the IBTA templates, PED contributed to better treatment outcomes in the ISA templates. Advances in FE modeling of different endovascular devices, along with CFD, has the potential to develop pre-interventional treatment planning tools that can help clinicians choose the best treatment option on a patient-specific basis for cerebral aneurysm repair.

7.4.3 Clinical Implications

Higher hemodynamic responses were observed for the larger aneurysm templates (i.e., templates with 6 mm DS). This finding agree with previous studies where aneurysms with larger DS, and were found to be more prone to rupture [3], [5]. Furthermore, increase in aneurysmal DS, or enlargement, was also observed to be an important

predictor of rupture risks where aneurysms at the time of rupture were found to be larger than at initial assessment [4]. Although treating the larger aneurysm with endovascular devices successfully decreased intra-aneurysmal hemodynamics, the absolute values of the calculated hemodynamic responses were still higher in the 6 mm aneurysm templates, indicating the possible benefit of treating a cerebral aneurysm at an earlier stage rather than waiting for it to grow. However, the treatment of smaller aneurysms is still a gray area since the risks of treating the aneurysm may outweigh the rupture risks [31].

Aneurysm size has been established as an independent predictor of aneurysmal rupture, and is currently used in clinical practice for cerebral aneurysm evaluation and treatment planning [3]–[5], [102]. But, in the case of a sidewall aneurysm, it was observed that IA had the largest contribution towards modifying pre- and post-treatment intra-aneurysmal hemodynamics. Furthermore, treatment with PED and coils produced different hemodynamic environments based on the aneurysm variant. It is therefore critical to understand and develop a combined geometric-hemodynamic basis for cerebral aneurysm evaluation and treatment planning.

While this study demonstrated the impact of aneurysm geometry and treatment on cerebral aneurysm hemodynamics, it is not without some noteworthy limitations. First, only idealized cerebral aneurysm templates were investigated in this study. While the need for a patient-specific evaluation of cerebral aneurysm hemodynamics is necessary, the goal was to attribute specific hemodynamic features to geometric underliers. Second, the vessel wall was assumed to be rigid. Although compliant simulations would be more beneficial, previous studies have demonstrated that geometry is the main driving factor for cerebral aneurysm hemodynamics, and the effects of compliance is secondary [44],

[90]. Furthermore, cerebral blood vessels are stiffer in comparison to extra-cranial vasculature, with a distensibility of about 6% [106]–[108]. Third, the study was investigated under steady inflow boundary conditions. Previous studies, including the data presented in Chapters 4 and 6, have shown that steady flow data provide a strong indication of the pulsatile flow simulations results [20], [109], [110], [116].

CHAPTER 8

CONCLUSIONS AND FUTURE WORK

The main objectives of this dissertation were to (1) characterize the effects of geometry on cerebral aneurysm hemodynamics (presented in Chapters 4 and 5), and (2) characterize the effects of geometry on endovascular treatment outcomes (presented in Chapters 6 and 7). The effects of geometric factors on hemodynamics in cerebral aneurysms were quantified using CFD simulations. The CFD simulations were also validated against data from experimental flow measurements using PIV. While some of the findings were intuitive, confirming them against a full factorial experimental design provides an objective basis that complements clinical experience. A fundamental understanding of the effects of cerebral aneurysm geometry on hemodynamics was established by utilizing controlled factors and conditions, such as low and high levels of geometric and treatment factors, idealized cerebral aneurysm templates, steady state simulations (with few pulsatile flow simulations for comparison), and Newtonian fluid models with rigid wall assumptions. The findings connecting the basic geometric features of a cerebral aneurysm to hemodynamics (in untreated and treated templates) provides a more combined geometric/hemodynamic basis, and has the potential to improve cerebral aneurysm evaluation and treatment criteria.

Future work will include examination of a broader range of anatomical geometries under steady and pulsatile flow conditions. Accordingly, more realistic boundary condition that include modeling the fluid-structure interactions is proposed. It is noteworthy that this study applies only to specific geometric cerebral aneurysm

templates. One of the anatomical cerebral aneurysms from the database included an aneurysm that was oriented normal to the plane formed by the parent and outlet vessels at the bifurcation (rather than within that plane, on top of the bifurcation). As a result, the hemodynamics in that cerebral aneurysm (which were investigated in a different study) did not match closely with any of the idealized templates. Furthermore, due to the computational costs associated with meshing and simulation of the virtually treated cerebral aneurysm templates, development of alternate meshing and device-modeling strategies are proposed. Alternative approaches to elucidating the hemodynamic effects of geometric factors (and effects on different endovascular treatment outcomes), such as integrating the templates to a multiscale model to understand the holistic impact of geometry on the global, cellular and genetic scale, may be pursued.

REFERENCES

- [1] “Brain Aneurysm Statistics and Facts | The Brain Aneurysm Foundation,” 19-Aug-2010.[Online]. Available: http://www.bafound.org/Statistics_and_Facts. [Accessed: 01-Mar-2016].
- [2] J. C. Lasheras, “The Biomechanics of Arterial Aneurysms,” *Annu.Rev. Fluid Mech.*, vol. 39, no. 1, pp. 293–319, 2007.
- [3] T. I. S. of U. I. A. Investigators, “Unruptured Intracranial Aneurysms — Risk of Rupture and Risks of Surgical Intervention,” *N. Engl. J. Med.*, vol. 339, no. 24, pp. 1725–1733, Dec. 1998.
- [4] J. E. Loewenstein, S. C. Gayle, E. J. Duffis, C. J. Prestigiacomo, and C. D. Gandhi, “The Natural History and Treatment Options for Unruptured Intracranial Aneurysms,” *Int. J. Vasc. Med.*, vol. 2012, p. e898052, Feb. 2012.
- [5] D. O. Wiebers, “Unruptured intracranial aneurysms: natural history, clinical outcome, and risks of surgical and endovascular treatment,” *The Lancet*, vol. 362, no. 9378, pp. 103–110, Jul. 2003.
- [6] T. Hassan, E. V. Timofeev, T. Saito, H. Shimizu, M. Ezura, Y. Matsumoto, K. Takayama, T. Tominaga, and A. Takahashi, “A proposed parent vessel geometry—based categorization of saccular intracranial aneurysms: computational flow dynamics analysis of the risk factors for lesion rupture,” *J. Neurosurg.*, vol. 103, no. 4, pp. 662–680, Oct. 2005.
- [7] B. Seibert, R. Tummala, R. Chow, A. Faridar, S. A. Mousavi, and A. A. Divani, “Intracranial aneurysms: review of current treatment options and outcomes,” *Endovasc. Interv. Neurol.*, vol. 2, p. 45, 2011.
- [8] E. S. Connolly, A. A. Rabinstein, J. R. Carhuapoma, C. P. Derdeyn, J. Dion, R. T. Higashida, B. L. Hoh, C. J. Kirkness, A. M. Naidech, C. S. Ogilvy, A. B. Patel, B. G. Thompson, and P. Vespa, “Guidelines for the Management of Aneurysmal Subarachnoid Hemorrhage A Guideline for Healthcare Professionals From the American Heart Association/American Stroke Association,” *Stroke*, vol. 43, no. 6, pp. 1711–1737, Jun. 2012.
- [9] A. Molyneux, “International Subarachnoid Aneurysm Trial (ISAT) of neurosurgical clipping versus endovascular coiling in 2143 patients with ruptured intracranial aneurysms: a randomised trial,” *The Lancet*, vol. 360, no. 9342, pp. 1267–1274, Oct. 2002.
- [10] R. F. Spetzler, H. Schuster, and R. A. Roski, “Elective extracranial-intracranial arterial bypass in the treatment of inoperable giant aneurysms of the internal carotid artery,” *J. Neurosurg.*, vol. 53, no. 1, pp. 22–27, Jul. 1980.

- [11] B. R. Gelber and T. M. Sundt, "Treatment of intracavernous and giant carotid aneurysms by combined internal carotid ligation and extra- to intracranial bypass," *J. Neurosurg.*, vol. 52, no. 1, pp. 1–10, Jan. 1980.
- [12] T. M. Sundt, D. G. Piepgras, W. R. Marsh, and N. C. Fode, "Saphenous vein bypass grafts for giant aneurysms and intracranial occlusive disease," *J. Neurosurg.*, vol. 65, no. 4, pp. 439–450, Oct. 1986.
- [13] J. L. Brisman, J. K. Song, and D. W. Newell, "Cerebral Aneurysms," *N. Engl. J. Med.*, vol. 355, no. 9, pp. 928–939, Aug. 2006.
- [14] R. T. Higashida, B. J. Lahue, M. T. Torbey, L. N. Hopkins, E. Leip, and D. F. Hanley, "Treatment of Unruptured Intracranial Aneurysms: A Nationwide Assessment of Effectiveness," *Am. J. Neuroradiol.*, vol. 28, no. 1, pp. 146–151, Jan. 2007.
- [15] M. H. Babiker, L. F. Gonzalez, F. Albuquerque, D. Collins, A. Elvikis, and D. H. Frakes, "Quantitative effects of coil packing density on cerebral aneurysm fluid dynamics: an in vitro steady flow study," *Ann. Biomed. Eng.*, vol. 38, no. 7, pp. 2293–2301, 2010.
- [16] H. G. Morales, M. Kim, E. E. Vivas, M.-C. Villa-Uriol, I. Larrabide, T. Sola, L. Guimaraens, and A. F. Frangi, "How Do Coil Configuration and Packing Density Influence Intra-Aneurysmal Hemodynamics?," *Am. J. Neuroradiol.*, vol. 32, no. 10, pp. 1935–1941, Nov. 2011.
- [17] M. Sluzewski, W. J. van Rooij, M. J. Slob, J. O. Bescós, C. H. Slump, and D. Wijnalda, "Relation between Aneurysm Volume, Packing, and Compaction in 145 Cerebral Aneurysms Treated with Coils," *Radiology*, vol. 231, no. 3, pp. 653–658, Jun. 2004.
- [18] G. M. Debrun, V. A. Aletich, P. Kehrl, M. Misra, J. I. Ausman, F. Charbel, and H. Shownkeen, "Aneurysm Geometry: An Important Criterion in Selecting Patients for Guglielmi Detachable Coiling," *Neurol. Med. Chir. (Tokyo)*, vol. 38, no. suppl, pp. 1–20, 1998.
- [19] W. Brinjikji, H. J. Cloft, and D. F. Kallmes, "Difficult aneurysms for endovascular treatment: overdue or undertall?," *AJNR Am. J. Neuroradiol.*, vol. 30, no. 8, pp. 1513–1517, Sep. 2009.
- [20] B. N. Roszelle, P. Nair, L. F. Gonzalez, M. H. Babiker, J. Ryan, and D. Frakes, "Comparison Among Different High Porosity Stent Configurations: Hemodynamic Effects of Treatment in a Large Cerebral Aneurysm," *J. Biomech. Eng.*, vol. 136, no. 2, p. 021013, 2014.

- [21] P. Lylyk, C. Miranda, R. Ceratto, A. Ferrario, E. Scrivano, H. R. Luna, A. L. Berez, Q. Tran, P. K. Nelson, and D. Fiorella, “Curative Endovascular Reconstruction of Cerebral Aneurysms with the Pipeline Embolization Device: The Buenos Aires Experience,” *Neurosurgery*, vol. 64, no. 4, pp. 632–643, Apr. 2009.
- [22] P. K. Nelson, P. Lylyk, I. Szikora, S. G. Wetzel, I. Wanke, and D. Fiorella, “The Pipeline Embolization Device for the Intracranial Treatment of Aneurysms Trial,” *Am. J. Neuroradiol.*, vol. 32, no. 1, pp. 34–40, Jan. 2011.
- [23] S. Tateshima, J. G. Jones, F. M. Basto, F. Vinuela, and G. R. Duckwiler, “Aneurysm pressure measurement before and after placement of a Pipeline stent: feasibility study using a 0.014 inch pressure wire for coronary intervention,” *J. NeuroInterventional Surg.*, pp. neurintsurg–2014–011214, May 2014.
- [24] C. for D. and R. Health, “Recently-Approved Devices - Pipeline™ Embolization Device - P100018,” Apr-2011. [Online]. Available: <http://www.fda.gov/MedicalDevices/ProductsandMedicalProcedures/DeviceApprovalsandClearances/Recently-ApprovedDevices/ucm252130.htm>. [Accessed: 21-Mar-2016].
- [25] S. C.-H. Yu, C.-K. Kwok, P.-W. Cheng, K.-Y. Chan, S. S. Lau, W.-M. Lui, K.-M. Leung, R. Lee, H. K.-M. Cheng, Y.-L. Cheung, C.-M. Chan, G. K.-C. Wong, J. W.-Y. Hui, Y.-C. Wong, C.-B. Tan, W.-L. Poon, K.-Y. Pang, A. K.-S. Wong, and K.-H. Fung, “Intracranial Aneurysms: Midterm Outcome of Pipeline Embolization Device—A Prospective Study in 143 Patients with 178 Aneurysms,” *Radiology*, vol. 265, no. 3, pp. 893–901, Dec. 2012.
- [26] L.-M. Lin, G. P. Colby, J. E. Kim, J. Huang, R. J. Tamargo, and A. L. Coon, “Immediate and follow-up results for 44 consecutive cases of small (<10 mm) internal carotid artery aneurysms treated with the pipeline embolization device,” *Surg. Neurol. Int.*, vol. 4, p. 114, 2013.
- [27] W. Brinjikji, M. H. Murad, G. Lanzino, H. J. Cloft, and D. F. Kallmes, “Endovascular Treatment of Intracranial Aneurysms with Flow Diverters A Meta-Analysis,” *Stroke*, vol. 44, no. 2, pp. 442–447, Feb. 2013.
- [28] J. R. Cebal, F. Mut, M. Raschi, E. Scrivano, R. Ceratto, P. Lylyk, and C. M. Putman, “Aneurysm Rupture Following Treatment with Flow-Diverting Stents: Computational Hemodynamics Analysis of Treatment,” *Am. J. Neuroradiol.*, vol. 32, no. 1, pp. 27–33, Jan. 2011.
- [29] T. Ishibashi, Y. Murayama, M. Urashima, T. Saguchi, M. Ebara, H. Arakawa, K. Irie, H. Takao, and T. Abe, “Unruptured Intracranial Aneurysms Incidence of Rupture and Risk Factors,” *Stroke*, vol. 40, no. 1, pp. 313–316, Jan. 2009.

- [30] M. J. H. Wermer, I. C. van der Schaaf, A. Algra, and G. J. E. Rinkel, "Risk of Rupture of Unruptured Intracranial Aneurysms in Relation to Patient and Aneurysm Characteristics An Updated Meta-Analysis," *Stroke*, vol. 38, no. 4, pp. 1404–1410, Apr. 2007.
- [31] M. Sonobe, T. Yamazaki, M. Yonekura, and H. Kikuchi, "Small Unruptured Intracranial Aneurysm Verification Study SUAVe Study, Japan," *Stroke*, vol. 41, no. 9, pp. 1969–1977, Sep. 2010.
- [32] The UCAS Japan Investigators, "The Natural Course of Unruptured Cerebral Aneurysms in a Japanese Cohort," *N. Engl. J. Med.*, vol. 366, no. 26, pp. 2474–2482, Jun. 2012.
- [33] T. R. Forget, R. Benitez, E. Veznedaroglu, A. Sharan, W. Mitchell, M. Silva, and R. H. Rosenwasser, "A review of size and location of ruptured intracranial aneurysms," *Neurosurgery*, vol. 49, no. 6, pp. 1322–1325; discussion 1325–1326, Dec. 2001.
- [34] N. F. M. D. Kassell and J. C. M. S. Torner, "Size of Intracranial Aneurysms," *Neurosurgery*, vol. 12, no. 3, pp. 291–297, Mar. 1983.
- [35] Y. Hoi, H. Meng, S. H. Woodward, B. R. Bendok, R. A. Hanel, L. R. Guterman, and L. N. Hopkins, "Effects of arterial geometry on aneurysm growth: three-dimensional computational fluid dynamics study," *J. Neurosurg.*, vol. 101, no. 4, pp. 676–681, Oct. 2004.
- [36] J. Raymond, F. Guilbert, A. Weill, S. A. Georganos, L. Juravsky, A. Lambert, J. Lamoureux, M. Chagnon, and D. Roy, "Long-Term Angiographic Recurrences After Selective Endovascular Treatment of Aneurysms With Detachable Coils," *Stroke*, vol. 34, no. 6, pp. 1398–1403, Jun. 2003.
- [37] I. Szikora, Z. Berentei, Z. Kulcsar, M. Marosfoi, Z. S. Vajda, W. Lee, A. Berez, and P. K. Nelson, "Treatment of Intracranial Aneurysms by Functional Reconstruction of the Parent Artery: The Budapest Experience with the Pipeline Embolization Device," *Am. J. Neuroradiol.*, vol. 31, no. 6, pp. 1139–1147, Jun. 2010.
- [38] B. Weir, C. Amidei, G. Kongable, J. M. Findlay, N. F. Kassell, J. Kelly, L. Dai, and T. G. Karrison, "The aspect ratio (dome/neck) of ruptured and unruptured aneurysms," *J. Neurosurg.*, vol. 99, no. 3, pp. 447–451, Sep. 2003.
- [39] G. J. Hademenos, T. F. Massoud, F. Turjman, and J. W. Sayre, "Anatomical and morphological factors correlating with rupture of intracranial aneurysms in patients referred for endovascular treatment," *Neuroradiology*, vol. 40, no. 11, pp. 755–760, Nov. 1998.

- [40] J. Beck, S. Rohde, M. el Beltagy, M. Zimmermann, J. Berkefeld, V. Seifert, and A. Raabe, “Difference in configuration of ruptured and unruptured intracranial aneurysms determined by biplanar digital subtraction angiography,” *Acta Neurochir. (Wien)*, vol. 145, no. 10, pp. 861–865, Oct. 2003.
- [41] B. V. Nahed, M. L. DiLuna, T. Morgan, E. Ocal, A. A. Hawkins, K. Ozduman, K. T. Kahle, A. Chamberlain, A. P. Amar, and M. Gunel, “Hypertension, age, and location predict rupture of small intracranial aneurysms,” *Neurosurgery*, vol. 57, no. 4, pp. 676–683; discussion 676–683, Oct. 2005.
- [42] M. Shojima, M. Oshima, K. Takagi, R. Torii, M. Hayakawa, K. Katada, A. Morita, and T. Kirino, “Magnitude and Role of Wall Shear Stress on Cerebral Aneurysm Computational Fluid Dynamic Study of 20 Middle Cerebral Artery Aneurysms,” *Stroke*, vol. 35, no. 11, pp. 2500–2505, Nov. 2004.
- [43] J. R. Cebral, F. Mut, J. Weir, and C. M. Putman, “Association of Hemodynamic Characteristics and Cerebral Aneurysm Rupture,” *Am. J. Neuroradiol.*, vol. 32, no. 2, pp. 264–270, Feb. 2011.
- [44] J. R. Cebral, F. Mut, J. Weir, and C. M. Putman, “Association of Hemodynamic Characteristics and Cerebral Aneurysm Rupture,” *Am. J. Neuroradiol.*, vol. 32, no. 2, pp. 264–270, Feb. 2011.
- [45] J. Xiang, S. K. Natarajan, M. Tremmel, D. Ma, J. Mocco, L. N. Hopkins, A. H. Siddiqui, E. I. Levy, and H. Meng, “Hemodynamic–morphologic discriminants for intracranial aneurysm rupture,” *Stroke*, vol. 42, no. 1, pp. 144–152, 2011.
- [46] M. I. Baharoglu, C. M. Schirmer, D. A. Hoit, B.-L. Gao, and A. M. Malek, “Aneurysm Inflow-Angle as a Discriminant for Rupture in Sidewall Cerebral Aneurysms Morphometric and Computational Fluid Dynamic Analysis,” *Stroke*, vol. 41, no. 7, pp. 1423–1430, Jul. 2010.
- [47] D. M. Sforza, C. M. Putman, and J. R. Cebral, “Hemodynamics of Cerebral Aneurysms,” *Annu. Rev. Fluid Mech.*, vol. 41, pp. 91–107, Jan. 2009.
- [48] R. Aaslid, T. M. Markwalder, and H. Nornes, “Noninvasive transcranial Doppler ultrasound recording of flow velocity in basal cerebral arteries,” *J. Neurosurg.*, vol. 57, no. 6, pp. 769–774, Dec. 1982.
- [49] A. Keedy, “An overview of intracranial aneurysms,” *McGill J. Med. MJM*, vol. 9, no. 2, p. 141, Jul. 2006.
- [50] S. Purkayastha and F. Sorond, “Transcranial Doppler Ultrasound: Technique and Application,” *Semin. Neurol.*, vol. 32, no. 4, pp. 411–420, Sep. 2012.

- [51] H. A. Nicoletto and M. H. Burkman, "Transcranial Doppler series part II: performing a transcranial Doppler," *Am. J. Electroneurodiagnostic Technol.*, vol. 49, no. 1, pp. 14–27, Mar. 2009.
- [52] G. Tsivgoulis, A. V. Alexandrov, and M. A. Sloan, "Advances in transcranialdoppler ultrasonography," *Curr. Neurol. Neurosci. Rep.*, vol. 9, no. 1, pp. 46–54, Dec. 2008.
- [53] D. Harrington, L. Boxt, and P. Murray, "Digital subtraction angiography: overview of technical principles," *Am. J. Roentgenol.*, vol. 139, no. 4, pp. 781–786, Oct. 1982.
- [54] R. Anxionnat, S. Bracard, X. Ducrocq, Y. Troussel, L. Launay, E. Kerrien, M. Braun, R. Vaillant, F. Scomazzoni, A. Lebedinsky, and L. Picard, "Intracranial Aneurysms: Clinical Value of 3D Digital Subtraction Angiography in the Therapeutic Decision and Endovascular Treatment," *Radiology*, vol. 218, no. 3, pp. 799–808, Mar. 2001.
- [55] O. I. Tähtinen, R. L. Vanninen, H. I. Manninen, R. Rautio, A. Haapanen, T. Niskakangas, J. Rinne, and L. Keski-Nisula, "Wide-necked Intracranial Aneurysms: Treatment with Stent-assisted Coil Embolization during Acute (<72 Hours) Subarachnoid Hemorrhage—Experience in 61 Consecutive Patients," *Radiology*, vol. 253, no. 1, pp. 199–208, Oct. 2009.
- [56] N. G. Warnock, M. R. Gandhi, U. Bergvall, and T. Powell, "Complications of intraarterial digital subtraction angiography in patients investigated for cerebral vascular disease," *Br. J. Radiol.*, vol. 66, no. 790, pp. 855–858, Oct. 1993.
- [57] A.-M. Leffers and A. Wagner, "Neurologic Complications of Cerebral Angiography," *ActaRadiol.*, vol. 41, no. 3, pp. 204–210, May 2000.
- [58] J. R. Waugh and N. Sacharias, "Arteriographic complications in the DSA era.," *Radiology*, vol. 182, no. 1, pp. 243–246, Jan. 1992.
- [59] K. W. Stock, S. Wetzel, E. Kirsch, G. Bongartz, W. Steinbrich, and E. W. Radue, "Anatomic evaluation of the circle of Willis: MR angiography versus intraarterial digital subtraction angiography.," *Am. J. Neuroradiol.*, vol. 17, no. 8, pp. 1495–1499, Sep. 1996.
- [60] B. Patruş, J. P. Laissy, S. Jouini, W. Kawiecki, P. Coty, and J. Thiébot, "Magnetic resonance angiography (MRA) of the circle of Willis: a prospective comparison with conventional angiography in 54 subjects," *Neuroradiology*, vol. 36, no. 3, pp. 193–197, Apr. 1994.

- [61] E. T. Chappell, F. C. Moure, and M. C. Good, "Comparison of computed tomographic angiography with digital subtraction angiography in the diagnosis of cerebral aneurysms: a meta-analysis," *Neurosurgery*, vol. 52, no. 3, pp. 624–631, 2003.
- [62] G. B. Anderson, D. E. Steinke, K. C. Petruk, R. Ashforth, and J. M. Findlay, "Computed tomographic angiography versus digital subtraction angiography for the diagnosis and early treatment of ruptured intracranial aneurysms," *Neurosurgery*, vol. 45, no. 6, p. 1315, 1999.
- [63] R. Gasparotti and R. Liserre, "Intracranial aneurysms," *Eur. Radiol.*, vol. 15, no. 3, pp. 441–447, Jan. 2005.
- [64] J. R. Cebal, M. A. Castro, S. Appanaboyina, C. M. Putman, D. Millan, and A. F. Frangi, "Efficient pipeline for image-based patient-specific analysis of cerebral aneurysm hemodynamics: technique and sensitivity," *Med. Imaging IEEE Trans. On*, vol. 24, no. 4, pp. 457–467, 2005.
- [65] C. Karmonik, R. Klucznik, and G. Benndorf, "Blood Flow in Cerebral Aneurysms: Comparison of Phase Contrast Magnetic Resonance and Computational Fluid Dynamics - Preliminary Experience," *RöFo - Fortschritte Auf Dem Geb. RöntgenstrahlenBildgeb. Verfahr.*, vol. 180, no. 3, pp. 209–215, Mar. 2008.
- [66] L. Boussel, V. Rayz, A. Martin, G. Acevedo-Bolton, M. T. Lawton, R. Higashida, W. S. Smith, W. L. Young, and D. Saloner, "Phase-contrast magnetic resonance imaging measurements in intracranial aneurysms in vivo of flow patterns, velocity fields, and wall shear stress: Comparison with computational fluid dynamics," *Magn. Reson. Med.*, vol. 61, no. 2, pp. 409–417, Feb. 2009.
- [67] J. R. Cebal, M. A. Castro, O. Soto, R. Löhner, and N. Alperin, "Blood-flow models of the circle of Willis from magnetic resonance data," *J. Eng. Math.*, vol. 47, no. 3–4, pp. 369–386, Dec. 2003.
- [68] S. Tateshima, Y. Murayama, J. P. Villablanca, T. Morino, K. Nomura, K. Tanishita, and F. Viñuela, "In Vitro Measurement of Fluid-Induced Wall Shear Stress in Unruptured Cerebral Aneurysms Harboring Blebs," *Stroke*, vol. 34, no. 1, pp. 187–192, Jan. 2003.
- [69] B. B. Lieber, V. Livescu, L. N. Hopkins, and A. K. Wakhloo, "Particle Image Velocimetry Assessment of Stent Design Influence on Intra-Aneurysmal Flow," *Ann. Biomed. Eng.*, vol. 30, no. 6, pp. 768–777, Jun. 2002.
- [70] F. Dorn, F. Niedermeyer, A. Balasso, D. Liepsch, and T. Liebig, "The effect of stents on intra-aneurysmal hemodynamics: in vitro evaluation of a pulsatile sidewall aneurysm using laser Doppler anemometry," *Neuroradiology*, vol. 53, no. 4, pp. 267–272, Apr. 2011.

- [71] J. Seong, A. K. Wakhloo, and B. B. Lieber, “In Vitro Evaluation of Flow Divertors in an Elastase-Induced Saccular Aneurysm Model in Rabbit,” *J. Biomech. Eng.*, vol. 129, no. 6, pp. 863–872, Mar. 2007.
- [72] P. Bouillot, O. Brina, R. Ouared, K.-O. Lovblad, M. Farhat, and V. M. Pereira, “Particle Imaging Velocimetry Evaluation of Intracranial Stents in Sidewall Aneurysm: Hemodynamic Transition Related to the Stent Design,” *PLOS ONE*, vol. 9, no. 12, p. e113762, Dec. 2014.
- [73] G. Cantón, D. I. Levy, J. C. Lasheras, and P. K. Nelson, “Flow changes caused by the sequential placement of stents across the neck of sidewall cerebral aneurysms,” *J. Neurosurg.*, vol. 103, no. 5, pp. 891–902, Nov. 2005.
- [74] M. Haithem Babiker, Colin Kealy, Younjae Chung, Gregory P. Carman, Daniel S. Levi, and David H Frakes, “In-vitro fluid dynamic evaluation of a novel hyper elastic-thin film nitinol stent and the pipeline embolization device for cerebral aneurysm treatment,” presented at the International Stroke Conference, 2012.
- [75] M. D. Ford, H. N. Nikolov, J. S. Milner, S. P. Lownie, E. M. DeMont, W. Kalata, F. Loth, D. W. Holdsworth, and D. A. Steinman, “PIV-measured versus CFD-predicted flow dynamics in anatomically realistic cerebral aneurysm models,” *J. Biomech. Eng.*, vol. 130, no. 2, p. 021015, 2008.
- [76] Y. Hoi, S. H. Woodward, M. Kim, D. B. Taulbee, and H. Meng, “Validation of CFD Simulations of Cerebral Aneurysms With Implication of Geometric Variations,” *J. Biomech. Eng.*, vol. 128, no. 6, pp. 844–851, Dec. 2006.
- [77] M. Raschi, F. Mut, G. Byrne, C. M. Putman, S. Tateshima, F. Viñuela, T. Tanoue, K. Tanishita, and J. R. Cebral, “CFD and PIV analysis of hemodynamics in a growing intracranial aneurysm,” *Int. J. Numer. Methods Biomed. Eng.*, vol. 28, no. 2, pp. 214–228, 2012.
- [78] P. van Ooij, A. Guédon, C. Poelma, J. Schneiders, M. C. M. Rutten, H. A. Marquering, C. B. Majoie, E. VanBavel, and A. J. Nederveen, “Complex flow patterns in a real-size intracranial aneurysm phantom: phase contrast MRI compared with particle image velocimetry and computational fluid dynamics,” *NMR Biomed.*, vol. 25, no. 1, pp. 14–26, 2012.
- [79] M. H. Babiker, B. Chong, L. F. Gonzalez, S. Cheema, and D. H. Frakes, “Finite element modeling of embolic coil deployment: Multifactor characterization of treatment effects on cerebral aneurysm hemodynamics,” *J. Biomech.*, vol. 46, no. 16, pp. 2809–2816, Nov. 2013.
- [80] R. J. Damiano, D. Ma, J. Xiang, A. H. Siddiqui, K. V. Snyder, and H. Meng, “Finite element modeling of endovascular coiling and flow diversion enables hemodynamic prediction of complex treatment strategies for intracranial aneurysm,” *J. Biomech.*, vol. 48, no. 12, pp. 3332–3340, Sep. 2015.

- [81] M. Kim, D. B. Taulbee, M. Tremmel, and H. Meng, "Comparison of Two Stents in Modifying Cerebral Aneurysm Hemodynamics," *Ann. Biomed. Eng.*, vol. 36, pp. 726–741, Feb. 2008.
- [82] A. Valencia, A. Zarate, M. Galvez, and L. Badilla, "Non-Newtonian blood flow dynamics in a right internal carotid artery with a saccular aneurysm," *Int. J. Numer. Methods Fluids*, vol. 50, no. 6, pp. 751–764, Feb. 2006.
- [83] I. E. Vignon and C. A. Taylor, "Outflow boundary conditions for one-dimensional finite element modeling of blood flow and pressure waves in arteries," *Wave Motion*, vol. 39, no. 4, pp. 361–374, Apr. 2004.
- [84] I. E. Vignon-Clementel, C. Alberto Figueroa, K. E. Jansen, and C. A. Taylor, "Outflow boundary conditions for three-dimensional finite element modeling of blood flow and pressure in arteries," *Comput. Methods Appl. Mech. Eng.*, vol. 195, no. 29–32, pp. 3776–3796, Jun. 2006.
- [85] M. S. Olufsen, "Structured tree outflow condition for blood flow in larger systemic arteries," *Am. J. Physiol. - Heart Circ. Physiol.*, vol. 276, no. 1, pp. H257–H268, Jan. 1999.
- [86] Alison L. Marsden and Ethan Kung, "Chapter 7: Multiscale Modeling of Cardiovascular Flows," in *Computational Bioengineering*, CRC Press Taylor & Francis Group, 2015.
- [87] A. L. Marsden and M. Esmaily-Moghadam, "Multiscale modeling of cardiovascular flows for clinical decision support," *Appl. Mech. Rev.*, vol. 67, no. 3, p. 030804, 2015.
- [88] L.-D. Jou, A. Mohamed, D. H. Lee, and M. E. Mawad, "3D Rotational Digital Subtraction Angiography May Underestimate Intracranial Aneurysms: Findings from Two Basilar Aneurysms," *Am. J. Neuroradiol.*, vol. 28, no. 9, pp. 1690–1692, Oct. 2007.
- [89] M. D. Ford, N. Alperin, S. H. Lee, D. W. Holdsworth, and D. A. Steinman, "Characterization of volumetric flow rate waveforms in the normal internal carotid and vertebral arteries," *Physiol. Meas.*, vol. 26, no. 4, p. 477, 2005.
- [90] S. Z. Zhao, X. Y. Xu, A. D. Hughes, S. A. Thom, A. V. Stanton, B. Ariff, and Q. Long, "Blood flow and vessel mechanics in a physiologically realistic model of a human carotid arterial bifurcation," *J. Biomech.*, vol. 33, no. 8, pp. 975–984, Aug. 2000.
- [91] L. Dempere-Marco, E. Oubel, M. Castro, C. Putman, A. Frangi, and J. Cebral, "CFD analysis incorporating the influence of wall motion: application to intracranial aneurysms," *Med. Image Comput. Comput.-Assist. Interv. MICCAI Int. Conf. Med. Image Comput. Comput.-Assist. Interv.*, vol. 9, no. Pt 2, pp. 438–445, 2006.

- [92] R. J. Adrian and J. Westerweel, *Particle Image Velocimetry*. Cambridge University Press, 2011.
- [93] W. I. Schievink, “Intracranial Aneurysms,” *N. Engl. J. Med.*, vol. 336, no. 1, pp. 28–40, Jan. 1997.
- [94] H. Meng, Z. Wang, Y. Hoi, L. Gao, E. Metaxa, D. D. Swartz, and J. Kolega, “Complex Hemodynamics at the Apex of an Arterial Bifurcation Induces Vascular Remodeling Resembling Cerebral Aneurysm Initiation,” *Stroke*, vol. 38, no. 6, pp. 1924–1931, Jun. 2007.
- [95] J. R. Cebral, M. A. Castro, J. E. Burgess, R. S. Pergolizzi, M. J. Sheridan, and C. M. Putman, “Characterization of Cerebral Aneurysms for Assessing Risk of Rupture By Using Patient-Specific Computational Hemodynamics Models,” *Am. J. Neuroradiol.*, vol. 26, no. 10, pp. 2550–2559, Nov. 2005.
- [96] J. M. Wardlaw and P. M. White, “The detection and management of unruptured intracranial aneurysms,” *Brain*, vol. 123, no. 2, pp. 205–221, Feb. 2000.
- [97] R. D. Rhew and P. A. Parker, “A parametric geometry computational fluid dynamics (CFD) study utilizing design of experiments (DOE),” *Am. Institute Aeronaut. Astronaut. AIAA*, vol. 1615, p. 2007, 2007.
- [98] R. Taylor, “Interpretation of the correlation coefficient: a basic review,” *J. Diagn. Med. Sonogr.*, vol. 6, no. 1, pp. 35–39, 1990.
- [99] M. Castro, C. Putman, A. Radaelli, A. Frangi, and J. Cebral, “Hemodynamics and Rupture of Terminal Cerebral Aneurysms,” *Acad. Radiol.*, vol. 16, no. 10, pp. 1201–1207, Oct. 2009.
- [100] K. Pekkan, L. P. Dasi, D. de Zélicourt, K. S. Sundareswaran, M. A. Fogel, K. R. Kanter, and A. P. Yoganathan, “Hemodynamic Performance of Stage-2 Univentricular Reconstruction: Glenn vs. Hemi-Fontan Templates,” *Ann. Biomed. Eng.*, vol. 37, no. 1, pp. 50–63, Nov. 2008.
- [101] V. L. Rayz, A. Abla, L. Bousset, J. R. Leach, G. Acevedo-Bolton, D. Saloner, and M. T. Lawton, “Computational Modeling of Flow-Altering Surgeries in Basilar Aneurysms,” *Ann. Biomed. Eng.*, vol. 43, no. 5, pp. 1210–1222, Oct. 2014.
- [102] S. Juvela, M. Porras, and K. Poussa, “Natural history of unruptured intracranial aneurysms: probability of and risk factors for aneurysm rupture,” *J. Neurosurg.*, vol. 93, no. 3, pp. 379–387, Sep. 2000.
- [103] J. Alastruey, K. H. Parker, J. Peiró, S. M. Byrd, and S. J. Sherwin, “Modelling the circle of Willis to assess the effects of anatomical variations and occlusions on cerebral flows,” *J. Biomech.*, vol. 40, no. 8, pp. 1794–1805, 2007.

- [104] T. F. Sherman, “On connecting large vessels to small. The meaning of Murray’s law,” *J. Gen. Physiol.*, vol. 78, no. 4, pp. 431–453, Oct. 1981.
- [105] L.-D. Jou, D. H. Lee, H. Morsi, and M. E. Mawad, “Wall shear stress on ruptured and unruptured intracranial aneurysms at the internal carotid artery,” *AJNR Am. J. Neuroradiol.*, vol. 29, no. 9, pp. 1761–1767, Oct. 2008.
- [106] K. Hayashi, H. Handa, S. Nagasawa, A. Okumura, and K. Moritake, “Stiffness and elastic behavior of human intracranial and extracranial arteries,” *J. Biomech.*, vol. 13, no. 2, pp. 175–184, 1980.
- [107] E. A. Warnert, K. Murphy, J. E. Hall, and R. G. Wise, “Noninvasive Assessment of Arterial Compliance of Human Cerebral Arteries with Short Inversion Time Arterial Spin Labeling,” *J. Cereb. Blood Flow Metab.*, vol. 35, no. 3, pp. 461–468, Mar. 2015.
- [108] M. Löw, K. Perktold, and R. Raunig, “Hemodynamics in rigid and distensible saccular aneurysms: a numerical study of pulsatile flow characteristics,” *Biorheology*, vol. 30, no. 3–4, pp. 287–298, Aug. 1993.
- [109] P. Nair, B. W. Chong, A. Indahlastari, J. Lindsay, D. Dejeu, V. Parthasarathy, J. Ryan, H. Babiker, C. Workman, and L. F. Gonzalez, others, “Hemodynamic Characterization of Geometric Cerebral Aneurysm Templates,” *J. Biomech.*, 2015.
- [110] M. H. Babiker, L. F. Gonzalez, J. Ryan, F. Albuquerque, D. Collins, A. Elvikis, and D. H. Frakes, “Influence of stent configuration on cerebral aneurysm fluid dynamics,” *J. Biomech.*, vol. 45, no. 3, pp. 440–447, 2012.
- [111] S. C. Johnston, C. B. Wilson, V. V. Halbach, R. T. Higashida, C. F. Dowd, M. W. McDermott, C. B. Applebury, T. L. Farley, and D. R. Gress, “Endovascular and surgical treatment of unruptured cerebral aneurysms: comparison of risks,” *Ann. Neurol.*, vol. 48, no. 1, pp. 11–19, Jul. 2000.
- [112] A. Lecler, J. Raymond, C. Rodriguez-Régent, F. Al Shareef, D. Trystram, S. Godon-Hardy, W. Ben Hassen, J.-F. Meder, C. Oppenheim, and O. N. Naggara, “Intracranial Aneurysms: Recurrences More than 10 Years after Endovascular Treatment—A Prospective Cohort Study, Systematic Review, and Meta-Analysis,” *Radiology*, vol. 277, no. 1, pp. 173–180, Jun. 2015.
- [113] H. D. Boogaarts, J. H. van Lieshout, M. J. van Amerongen, J. de Vries, A. L. M. Verbeek, J. A. Grotenhuis, G. P. Westert, and R. H. M. A. Bartels, “Aneurysm diameter as a risk factor for pretreatment rebleeding: a meta-analysis,” *J. Neurosurg.*, vol. 122, no. 4, pp. 921–928, Apr. 2015.

- [114] F. Turjman, T. F. Massoud, J. Sayre, and F. Viñuela, “Predictors of aneurysmal occlusion in the period immediately after endovascular treatment with detachable coils: a multivariate analysis,” *Am. J. Neuroradiol.*, vol. 19, no. 9, pp. 1645–1651, Oct. 1998.

APPENDIX A
PERMISSIONS

A.1 Copyright Permission for Chapter 4

4/14/2016

Rights & Access

[Authors' Rights](#)
[Help](#) | [Print](#)

RIGHTS & ACCESS

Elsevier Ltd

Article: Hemodynamic Characterization of Geometric Cerebral Aneurysm Templates
Corresponding author: Ms. Priya Nair
E-mail address: priyanair@asu.edu
Journal: Journal of Biomechanics
Our reference: BM7442
PII: S0021-9290(15)00676-4
DOI: 10.1016/j.jbiomech.2015.11.034

YOUR STATUS

» I am one author signing on behalf of all co-authors of the manuscript

ASSIGNMENT OF COPYRIGHT

I hereby assign to Elsevier Ltd the copyright in the manuscript identified above (where Crown Copyright is claimed, authors agree to grant an exclusive publishing and distribution license) and any tables, illustrations or other material submitted for publication as part of the manuscript (the "Article") in all forms and media (whether now known or later developed), throughout the world, in all languages, for the full term of copyright, effective when the Article is accepted for publication.

SUPPLEMENTAL MATERIALS

With respect to Supplemental Materials that I wish to make accessible either through a link in the Article or on a site or through a service of Elsevier Ltd, Elsevier Ltd shall be entitled to publish, post, reformat, index, archive, make available and link to such Supplemental Materials on a non-exclusive basis in all forms and media (whether now known or later developed) and to permit others to do so. "Supplemental Materials" shall mean additional materials that are not an intrinsic part of the Article, including but not limited to experimental data, e-components, encodings and software, and enhanced graphical, illustrative, video and audio material.

REVERSION OF RIGHTS

Articles may sometimes be accepted for publication but later rejected in the publication process, even in some cases after public posting in "Articles in Press" form, in which case all rights will revert to the author (see <http://www.elsevier.com/locate/withdrawalpolicy>).

REVISIONS AND ADDENDA

I understand that no revisions, additional terms or addenda to this Journal Publishing Agreement can be accepted without Elsevier Ltd's express written consent. I understand that this Journal Publishing Agreement supersedes any previous agreements I have entered into with Elsevier Ltd in relation to the Article from the date hereof.

RETENTION OF RIGHTS FOR SCHOLARLY PURPOSES.

I understand that I retain or am hereby granted (without the need to obtain further permission) the Retained Rights (see description below), and that no rights in patents, trademarks or other intellectual property rights are transferred to Elsevier Ltd.

The Retained Rights include the right to use the [Preprint](#), [Accepted Manuscript](#) and the [Published Journal Article](#) for [Personal Use](#), [Internal Institutional Use](#) and for [Scholarly Sharing](#).

In the case of the Accepted Manuscript and the Published Journal Article the Retained Rights exclude Commercial Use (unless expressly agreed in writing by Elsevier Ltd), other than use by the author in a subsequent compilation of the author's works or to extend the Article to book length form or re-use by the author of portions or excerpts in other works (with full acknowledgment of the original publication of the Article).

AUTHOR REPRESENTATIONS / ETHICS AND DISCLOSURE

I affirm the Author Representations noted below, and confirm that I have reviewed and complied with the relevant Instructions to Authors, Ethics in Publishing policy, and Conflicts of Interest disclosure. Please note that some journals may require that all co-authors sign and submit Conflicts of Interest disclosure forms. I am also aware of the publisher's policies with respect to retractions and withdrawal (<http://www.elsevier.com/locate/withdrawalpolicy>).

For further information see the publishing ethics page at <http://www.elsevier.com/publishingethics> and the journal home page.

Author representations

- » The Article I have submitted to the journal for review is original, has been written by the stated authors and has not been published
- » The Article was not submitted for review to another journal while under review by this journal and will not be submitted to any other journal
- » The Article and the Supplemental Materials contain no libellous or other unlawful statements and do not contain any materials that infringe the intellectual property or proprietary rights of any other person or entity.
- » I have obtained written permission from copyright owners for any excerpts from copyrighted works that are included and have credited the source.

file:///Users/priya/Dropbox/IPA%20LAB/Dissertation/Nair/Copyright/BM7442.html

1/2

4/14/2016

Rights & Access

the Article or the Supplemental Materials.

- » Except as expressly set out in this Journal Publishing Agreement, the Article is not subject to any prior rights or licenses and, if my authors' institution has a policy that might restrict my ability to grant exclusive rights under this Journal Publishing Agreement, a policy has been obtained.
- » If I am using any personal details or images of patients, research subjects or other individuals, I have obtained all consents required and complied with the publisher's policies relating to the use of such images or personal information. See <http://www.elsevier.com> for further information.
- » Any software contained in the Supplemental Materials is free from viruses, contaminants or worms.
- » If the Article or any of the Supplemental Materials were prepared jointly with other authors, I have informed the co-author(s) of this Publishing Agreement and that I am signing on their behalf as their agent, and I am authorized to do so.

For information on the publisher's copyright and access policies, please see <http://www.elsevier.com/copyright>.
[For more information about the definitions relating to this agreement click here.](#)

I have read and agree to the terms of the Journal Publishing Agreement.
27th November 2015

T-copyright-v20/2015

A.2 Copyright for Chapter 6

COPYRIGHT AGREEMENT (as of February 2010)

ASME Publishing • Two Park Avenue • New York, NY 10016

For questions about Conference paper copyright, please e-mail copyright@asme.org

For questions about Journal paper copyright, please email journalcopyright@asme.org

Before publication of your paper in a conference proceedings or journal, ASME must receive a signed Copyright Agreement. For conference papers, this form should be received by the deadline indicated by the Conference. Other forms may NOT be substituted for this form, nor may any wording on the form be changed.

PAPER NUMBER (for conference/journal papers): BIO-15-1390

TITLE: Hemodynamic Characterization of Geometric Cerebral Aneurysm Templates Treated with Embolic Coils

AUTHOR(s): David Frakes, Justin Ryan, M. Haithem Babiker, Priya Nair, Brian W. Chong, Aprinda Indahlastari, Christopher Workman, Hooman Yadollahi Farsani, Carlos E. Baccin

CONFERENCE NAME: _____

JOURNAL NAME: Journal of Biomechanical Engineering

ASME requests that authors/copyright owners assign copyright to ASME in order for a conference or journal paper to be published by ASME. Authors exempt from this request are direct employees of the U.S. Government, whereby papers are not subject to copyright protection in the U.S., or non-U.S. government employees, whose governments hold the copyright to the paper. Otherwise, the author/ copyright owner(s) of the Paper should sign this form as instructed below. Please refer to the section below "Who Should Sign" and also to ASME's [FAQ page](#) for more information regarding copyright ownership and the copyright process.

WHO SHOULD SIGN

Only the copyright owner(s) of the Paper, or an authorized representative, can sign this form. If one of the following applies, you may not own the copyright to the paper, or you may not be authorized to sign this agreement, and you may need to have the appropriate copyright owner(s) or organization representative sign this Agreement:

- (1) You created the Paper within the scope of your employment, and your employer is the copyright owner
- (2) You created the Paper under an independent contractor agreement**
- (3) You received a grant that funded your Paper.

Please review your company policies regarding copyright, and if you are not authorized to sign this agreement, please forward to the appropriate organization representative. Please review applicable company, institutional, and grant policies and your employment/independent contractor agreement to determine who holds the rights to your Paper. For more information, please refer to the [FAQs](#).

****Note to U.S. Government Contractors:** If you created the Paper under contract with the U.S. Government, e.g., U.S. Government labs, the paper may be subject to copyright, and you or your employer may own the copyright. Please review your company/institutional policies and your contractor agreement. Your Paper may also require a footer acknowledging contract information and also the following statement:

"The United States Government retains, and by accepting the article for publication, the publisher acknowledges that the United States Government retains, a non-exclusive, paid-up, irrevocable, worldwide license to publish or reproduce the published form of this work, or allow others to do so, for United States Government purposes."

It is your responsibility to ensure that the final PDF version of the Paper you submit includes all necessary footers and statements required under your contract.

COPYRIGHT ASSIGNMENT

The following terms of copyright assignment refer to Sections 1, 2, and 3. Sections 4 and 5 may not be subject to copyright.

The undersigned hereby assigns irrevocably to ASME all worldwide rights under copyright in the Paper.

Authors retain all proprietary rights in any idea, process, procedure, or articles of manufacture described in the Paper, including the right to seek patent protection for them. Authors may perform, lecture, teach, conduct related research, display all

or part of the Paper, and create derivative works in print or electronic format. Authors may reproduce and distribute the Paper for non-commercial purposes only. Non-commercial applies only to the sale of the paper per se. For all copies of the Paper made by Authors, Authors must acknowledge ASME as original publisher and include the names of all author(s), the publication title, and an appropriate copyright notice that identifies ASME as the copyright holder.

PLEASE READ THE [TERMS AND CONDITIONS](#) WHICH ARE FULLY INCORPORATED IN THIS AGREEMENT.

PAPERS OWNED BY ONE AUTHOR OR JOINT AUTHORS; DESIGNATED AUTHORS (For jointly authored works, all authors should submit a signed Agreement, or one Designated Author may sign on behalf of the other authors, but ONLY IF the designated author has secured written authorization to do so from all other authors. The designated author must be able to produce such written authorization if requested.)

Author, Co-Author, or Designated Author

Name: Priya Nair Signature: Priya Nair Date: 04 Aug 2015
Affiliation: Arizona State University Title: Graduate Student
(Company or Institution)
Street Address: School of Biological and Health Systems Engineering, 501 E Tyler Mall BLDG ECG RM #334
Tempe AZ 85287 United States
(City) (State) (Zip Code) (Country)
Phone: 480-205-6530 Fax: _____ Email: priyanair@asu.edu

Author: (Applied only if you are signing for other)

Name: _____ Signature: _____ Date: _____
Affiliation: _____ Title: _____
(Company or Institution)
Street Address: _____

(City) (State) (Zip Code) (Country)
Phone: _____ Fax: _____ Email: _____

ASME COPYRIGHT FORM TERMS AND CONDITIONS

The following terms and conditions are fully incorporated into the Copyright Form. Please read them carefully.

REPRESENTATIONS, OBLIGATIONS, ACKNOWLEDGEMENTS, AND INDEMNIFICATION

You represent and acknowledge that:

(A) This Paper represents: either the first publication of material or the first publication of an original compilation of information from a number of sources as specifically noted by footnotes and/or bibliography.

(B) You have the right to enter into this Copyright Form and to make the assignment of rights to ASME. If the Paper contains excerpts from other copyrighted material (including without limitation any diagrams, photographs, figures or text), you have acquired in writing all necessary rights from third parties to include those materials in the Paper, and have provided appropriate credit for that third-party material in footnotes or in a bibliography.

(C) If you are signing this Form on behalf of any co-authors or other copyright holders, you have obtained express authorizations from all those authors and/or copyright holders to make this assignment of rights to ASME.

(D) To the best of the author's knowledge, all statements contained in the Paper purporting to be facts are true or supported by reasonable scientific research, the Paper does not contain any defamatory or libelous material and does not infringe any third party's copyright, patent, trade secret, or other proprietary rights and does not violate the right of privacy or publicity of any third party or otherwise violate any other applicable law; furthermore that to the best of your ability, you are responsible for ensuring the accuracy of your research and the Paper's content.

(E) If the Paper was produced in the course of an author's employment by, or contractual relationship with, the U.S. Federal or State Government and/or contains classified material, it has been appropriately cleared for public release and such is indicated in the paper.

(F) The Paper is not subject to any prior claim, encumbrance or form and is not under consideration for publication elsewhere.

(G) You have appropriately cited and acknowledged all third parties who have contributed significantly in the Paper's technical aspects.

(H) ASME is not responsible for any misrepresentation, errors or omissions by those signing this copyright form.

(I) All print and electronic copies of the Paper submitted to ASME become ASME's physical property regardless of whether or not ASME publishes the Paper, and that ASME is not obligated to publish your paper (see the Termination Section below if your paper is not published).

(J) ASME is not responsible for any of your expenses incurred in connection with preparing the Paper or attending meetings to present it, nor will ASME pay you any financial compensation if it publishes your Paper.

(K) Subject to and to the maximum extent permitted by law, you agree to indemnify and hold harmless ASME from any damage or expense related to a breach of any of the representations and warranties above.

TERMINATION

If ASME decides not to publish your Paper, this Form, including all of ASME's rights in your Paper, terminates and you are thereafter free to offer the Paper for publication elsewhere.

GENERAL PROVISIONS

This Copyright Form, the Terms & Conditions, and [ASME Copyright Guidelines](#), constitutes the entire agreement between you and ASME, and supersedes all prior or current negotiations, understandings and representations, whether oral or written, between you and ASME concerning the Paper.

This Agreement is governed by, and should be construed in accordance with, the laws of the State of New York, United States of America, applicable to agreements made and performed there, except to the extent that your institution is prohibited by law from entering contracts governed by New York law, in which limited case this Agreement is governed by, and should be construed in accordance with, the laws of the jurisdiction in which your institution is located. Any claim, dispute, action or proceeding relating to this Agreement may be brought only in the applicable state and federal courts in the State and County of New York, and you expressly consent to personal jurisdiction and venue in any of those courts.

A.3 Permissions letter for usage of Figure 3.1



820 Jorie Blvd
Oak Brook, IL, 60523
TEL 1-630-571-2670
FAX 1-630-571-7837
RSNA.org

March 14, 2016

Priya Nair
School of Biological and Health Systems Engineering
Arizona State University

Dear Priya Nair:

The Radiological Society of North America (RSNA®) is pleased to grant you permission to reproduce the following figures in print, electronic, and web formats for educational, non-profit use in your PhD dissertation, provided you give full credit to the authors of the original publication.

Figures 1a, 1b, 1c
Tähtinen O I, Vanninen R L, Manninen H I, et al. Wide-necked intracranial aneurysms: Treatment with stent-assisted coil embolization during acute (<72 hours) subarachnoid hemorrhage—Experience in 61 consecutive patients. *Radiology* 2009;253:199-208.

This permission is a one-time, non-exclusive grant for English-language use and is exclusively limited to the usage stated and underlined above. The requestor guarantees to reproduce the material as originally published. Permission is granted under the condition that a full credit line is prominently placed (i.e. author name(s), journal name, copyright year, volume #, inclusive pages and copyright holder).

This permission becomes effective upon receipt of this signed contract. Please sign a copy of this agreement, return a signed copy to me and retain a copy for your files. Thank you for your interest in our publication.

[Print Name]: PRIYA NAIR
SIGNATURE: Priya Nair Date: 03-14-2016

Sincerely,

Ashley E. Daly
Senior Manager, Journal Rights & Communications
Publications

Phone: 630-590-7771

A.4 Permissions for usage of Figure 3.2 (CTA Image)

3/7/2016

PubMed Central, Figure 3: McGill J Med. 2006 Jul; 9(2): 141–146.



PMC full text: [Mcgill J Med. 2006 Jul; 9\(2\): 141–146.](#)

[Copyright/License](#) ▼

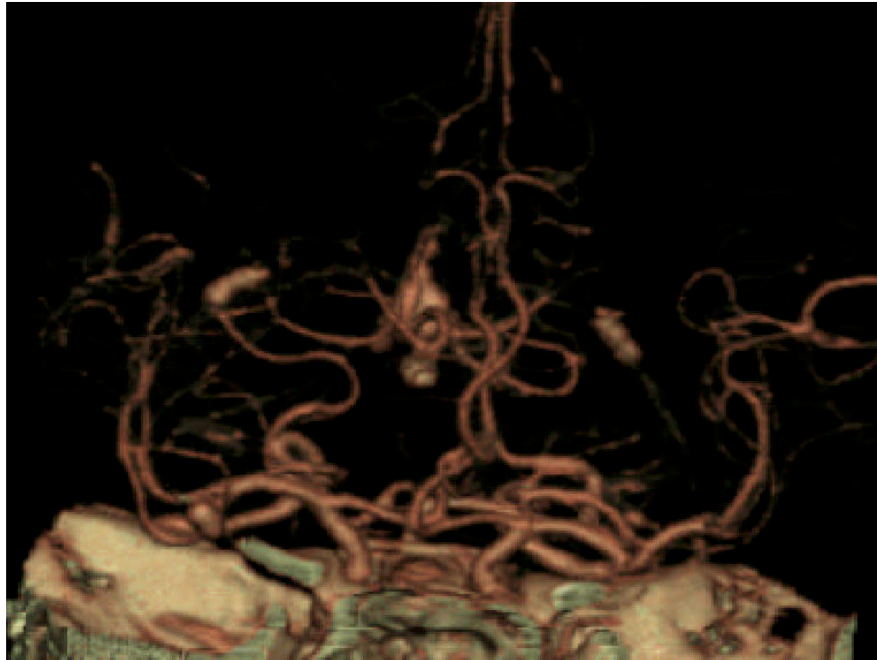
[Request permission to reuse](#)

<< Prev Figure 3 Next >>

Copyright © 2006 by MJM

This is an Open Access article distributed under the terms of the Creative Commons Attribution Non-Commercial No Derivatives License, which permits for noncommercial use, distribution, and reproduction in any digital medium, provided the original work is properly cited and is not altered in any way. For details, please refer to <http://creativecommons.org/licenses/by-nc-nd/3.0/>

Figure 3



Computed tomography (CT) angiography of the same aneurysm depicted in [Figure 2](#).

Images in this article

P.5 Permissions for usage of Figure 3.2 (MRA Image)

3/7/2016

PubMed Central, Figure 4: McGill J Med. 2006 Jul; 9(2): 141-146.



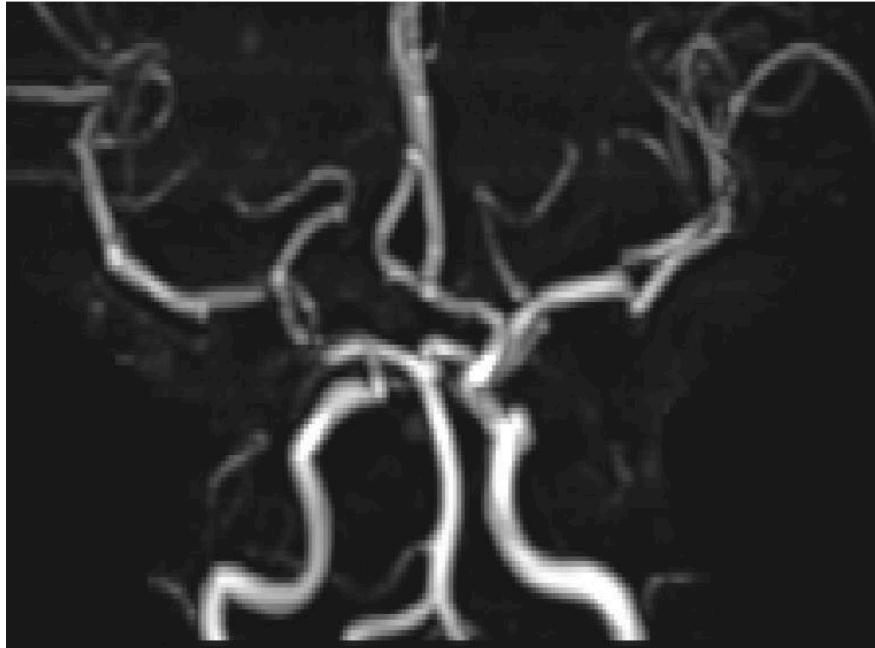
PMC full text: [Mcgill J Med. 2006 Jul; 9\(2\): 141-146.](#)
[Copyright/License](#) ▼ [Request permission to reuse](#)

<< Prev Figure 4 Next >>

[Copyright](#) © 2006 by MJM

This is an Open Access article distributed under the terms of the Creative Commons Attribution Non-Commercial No Derivatives License, which permits for noncommercial use, distribution, and reproduction in any digital medium, provided the original work is properly cited and is not altered in any way. For details, please refer to <http://creativecommons.org/licenses/by-nc-nd/3.0/>

Figure 4



Magnetic resonance (MR) angiogram depicting normal cerebral vasculature

Images in this article
